SINGLE ELECTRON CAPTURE FROM ATOMIC AND MOLECULAR COLLISIONS USING ADVANCED THEORETICAL METHODS

by

DAVID LYONS

(Under the Direction of Phillip C. Stancil)

Abstract

Cross sections for single electron capture (SEC), or charge exchange (CX), in collisions of $Ne^{(8-10)+} \ and \ Mg^{(8-12)+} \ with \ H \ and \ He, \ and \ Fe^{(8-9)+} \ with \ H, \ H_2, \ He, \ H_2O, \ CO, \ CO_2, \ and \ N_2, \ He, \ H_2O, \ CO, \ CO_2, \ Add \ N_2, \ He, \ H_2O, \ CO, \ CO_2, \ Add \ N_2, \ He, \ H_2O, \ CO, \ CO_2, \ Add \ N_2, \ He, \ H_2O, \ CO, \ CO_2, \ Add \ N_2, \ He, \ H_2O, \ CO, \ CO_2, \ Add \ N_2, \ He, \ H_2O, \ CO, \ CO_2, \ Add \ N_2, \ He, \ H_2O, \ CO, \ CO_2, \ Add \ N_2, \ He, \ H_2O, \ CO, \ CO_2, \ Add \ N_2, \ He, \ H_2O, \ CO, \ CO_2, \ Add \ N_2, \ He, \ H_2O, \ CO, \ CO_2, \ Add \ N_2, \ He, \ H_2O, \ CO, \ CO_2, \ Add \ N_2, \ He, \ H_2O, \ CO, \ CO_2, \ Add \ N_2, \ He, \ H_2O, \ CO, \ CO_2, \ Add \ N_2, \ He, \ H_2O, \ CO, \ CO_2, \ Add \ N_2, \ He, \ H_2O, \ CO, \ CO_2, \ Add \ N_2, \ He, \ H_2O, \ CO, \ CO_2, \ Add \ N_2, \ He, \ H_2O, \ CO, \ CO_2, \ Add \ N_2, \ He, \ H_2O, \ CO, \ CO_2, \ Add \ N_2, \ H_2O, \ CO, \ CO_2, \ Add \ N_2, \ H_2O, \ CO, \ CO_2, \ Add \ N_2, \ H_2O, \ CO, \ CO_2, \ Add \ N_2, \ H_2O, \ CO, \ CO_2, \ Add \ N_2, \ H_2O, \ CO, \ CO_2, \ Add \ N_2, \ H_2O, \ CO, \ CO_2, \ Add \ N_2, \ H_2O, \ CO, \ CO_2, \ Add \ N_2, \ H_2O, \ Add \ N_2, \ H_2O, \ Add \ N_2, \ H_2O, \ Add \ N_2O, \ Add$ are computed using an approximate multichannel Landau-Zener (MCLZ) formalism. The Molecular Orbital Close-Coupling (MOCC) method is also used for the cross section calculation of the $\mathrm{Ne}^{9+}\mathrm{+H}$ collision system. Final-state-resolved cross sections for the principal (n), orbital angular momentum (ℓ) , and where appropriate, total spin angular momentum (S) quantum numbers are explicitly computed except for the incident bare ions Ne^{10+} and Mg^{12+} . In the latter two cases, $n\ell$ -resolution is obtained from analytical ℓ -distribution functions applied to n-resolved MCLZ cross sections. In all cases, the cross sections are computed over the collision energy range 1 meV/u to 100 keV/u with LZ parameters estimated from atomic energies obtained from experiment, theory, or, in the case of high-lying Rydberg levels, estimated with a quantum defect approach. Errors in the energy differences in the adiabatic potentials at the avoided-crossing distances give the largest contribution to the uncertainties in the cross sections, which is expect to increase with decreasing cross section magnitude. The energy differences are deduced here with the Olson-Salop-Tauljberg radial coupling model. Proper selection of an ℓ -distribution function for bare ion collisions introduces another level of uncertainty in the results. Comparison is made to existing experimental or theoretical results when available, but such data are absent for most considered collision systems. The $n\ell S$ -resolved SEC cross sections are used in a optically thin cascade simulation to predict X-ray spectra and line ratios which will aid in modeling the X-ray emission in environments where charge exchange is an important mechanism. Details on a MCLZ computational package, $St\ddot{u}ckelberg$, are also provided.

INDEX WORDS: Atomic Data, Atomic Processes, Charge Exchange, Single Electron

Capture, Molecular Collisions, Atomic Collisions, Ionic Collisions, Cross Sections, Landau-Zener, Molecular Orbital Close Coupling,

Numerical Simulation

SINGLE ELECTRON CAPTURE FROM ATOMIC AND MOLECULAR COLLISIONS USING ADVANCED THEORETICAL METHODS

by

DAVID LYONS

BS, Electrical Engineering, Southern Illinois University
MS, Electrical Engineering, Southern Illinois University
MBA, University of Georgia
MS, Physics, University of Georgia

A Dissertation Submitted to the Graduate Faculty of The University of Georgia in Partial Fulfillment of the

Requirements for the Degree

DOCTOR OF PHILOSOPHY

ATHENS, GEORGIA

© 2019

David Lyons

All Rights Reserved

SINGLE ELECTRON CAPTURE FROM ATOMIC AND MOLECULAR COLLISIONS USING ADVANCED THEORETICAL METHODS

by

DAVID LYONS

Approved:

Major Professor: Phillip C. Stancil

Committee: Henning Meyer

Loris Magnani

Electronic Version Approved:

Suzanne Barbour Dean of the Graduate School The University of Georgia May 2019

DEDICATION

To the memory of Jeff Burns and his family.

To the memory of Dr. Howard Lee.

To my wife, Marina.

ACKNOWLEDGMENTS

As I slowly progressed during this program, I thank Dr. Phillip Sancil for his patience, understanding, and guidance.

When I became a graduate student, a graduate teaching assistant, and then a graduate reseach assistant in the Department of Physics and Astronomy at the University of Georgia, I was a full-time working professional. I had a schedule which allowed me to pursue a PhD in physics. I also had a wife and children, a house, cars, and the usual financial and time demands associated with such a life. It would not have been possible to participate in this program with a typical 9 hours per day, 5 days per week schedule. I am grateful to those managers who were supportive of me by allowing me remain on the schedule which made it possible for me to pursue this academic goal.

This work was partially supported by NASA grants NNX09AC46G and NNX13AF31G.

TABLE OF CONTENTS

		P	age
ACKN	OWLEDO	GMENTS	v
List (of Figu	RES	viii
List o	of Tabi	ES	xii
Снар	ΓER		
1	Intro	DUCTION	1
2	Тнеог	RY	4
	2.1	Landau-Zener	4
	2.2	Molecular Orbital Close Coupling	7
3	$NE^{(8-1)}$	$^{0)+}$ and $\mathrm{MG^{(8-12)+}}$ with H and He using MCLZ	10
	3.1	Introduction	10
	3.2	SINGLE ELECTRON CAPTURE CROSS SECTIONS	12
	3.3	NE^{10+}	13
	3.4	NE^{9+}	21
	3.5	NE^{8+}	24
	3.6	$\mathrm{MG^{12+}}$	26
	3.7	$\mathrm{MG^{11+}}$	30
	3.8	$\mathrm{MG^{10+}}$	34
	3.9	MG^{9+}	37
	3.10	MG^{8+}	41
	3 11	SUMMARY	43

4	$FE^{(8-9)}$	WITH H, H_2 , HE, H_2O , CO , CO_2 , AND N_2 USING MCLZ	46
	4.1	Introduction	46
	4.2	FE^{9+}	58
	4.3	$\mathrm{FE}^{8+}\ldots\ldots\ldots\ldots\ldots\ldots\ldots$	68
	4.4	Summary	77
5	$NE^{9+} +$	-H using MOCC	79
	5.1	Introduction	79
	5.2	Results	83
	5.3	Summary	83
6	Conci	LUSIONS	85
	6.1	MCLZ: $NE^{(8-10)+}$ and $MG^{(8-12)+}$	85
	6.2	MCLZ: $FE^{(8-9)+}$	85
	6.3	MOCC: $NE^{9+}+H$	86
Appei	NDIX		
A	Stück	KELBERG	87
Вівыс	OGRAPH	IY	88

LIST OF FIGURES

2.1	Polarization (V_p) and Coulomb (V_c) potentials	5
3.1	Ne^{q+} and Mg^{q+} total cross sections	12
3.2	$Ne^{10+}+X\rightarrow Ne^{9+}+X^+$ total cross sections	13
3.3	Ne ¹⁰⁺ +H \rightarrow Ne ⁹⁺ +H ⁺ $n\ell$ -resolved (low-energy) cross section comparisons	14
3.4	Ne ¹⁰⁺ +H \rightarrow Ne ⁹⁺ +H ⁺ $n\ell$ -resolved (statistical) cross section comparisons	15
3.5	$Ne^{10+}+H\rightarrow Ne^{9+}+H^+$ total cross section comparison	16
3.6	$Ne^{10+}+H\rightarrow Ne^{9+}+H^+$ n-resolved cross section comparison	17
3.7	$Ne^{10+}+He \rightarrow Ne^{9+}+He^+$ $n\ell$ -resolved cross sections	18
3.8	Ne ¹⁰⁺ +He \rightarrow Ne ⁹⁺ +He ⁺ $n\ell$ -resolved cross sections	19
3.9	$Ne^{10+}+He \rightarrow Ne^{9+}+He^+$ n-resolved cross sections	19
3.10	$Ne^{9+}+X\rightarrow Ne^{8+}+X^+$ total cross sections	21
3.11	$Ne^{9+}+X\rightarrow Ne^{8+}+X^+$ n-resolved cross sections	22
3.12	Ne ⁹⁺ +H \rightarrow Ne ⁸⁺ +H ⁺ n - and $n\ell$ -resolved cross section comparisons	23
3.13	$Ne^{8+}+X\rightarrow Ne^{7+}+X^+$ total cross sections	24
3.14	$\text{Ne}^{8+} + X \rightarrow \text{Ne}^{7+} + X^+$ n- and $n\ell$ -resolved cross section comparisons	25
3.15	Ne ⁸⁺ +H \rightarrow Ne ⁷⁺ +H ⁺ n - and $n\ell$ -resolved cross section comparisons	26
3.16	$Mg^{12+}+X\rightarrow Mg^{11+}+X^+$ total cross sections	27
3.17	$Mg^{12+}+H\rightarrow Mg^{11+}+H^+$ n-resolved cross sections	28
3.18	$Mg^{12+}+H\rightarrow Mg^{11+}+H^+$ $n\ell$ -resolved cross sections	28
3.19	$Mg^{12+}+H\rightarrow Mg^{11+}+H^+$ $n\ell$ -resolved cross sections	29
3.20	$Mg^{12+}+He \rightarrow Mg^{11+}+He^+$ n-resolved cross sections	29
3.21	$Mg^{12+}+He \rightarrow Mg^{11+}+He^+$ $n\ell$ -resolved cross sections	30
3.22	$Mg^{12+} + He \rightarrow Mg^{11+} + He^+$ $n\ell$ -resolved cross sections.	30

3.23	$Mg^{11+}+X \rightarrow Mg^{10+}+X^+$ total cross sections	31
3.24	$Mg^{11+}+H\rightarrow Mg^{10+}+H^+$ $n\ell$ -resolved cross sections	32
3.25	$Mg^{11+}+H\rightarrow Mg^{10+}+H^+$ $n\ell$ -resolved cross sections	32
3.26	$Mg^{11+}+H\rightarrow Mg^{10+}+H^+$ n-resolved cross sections	33
3.27	$Mg^{11+}+He \rightarrow Mg^{10+}+He^+$ $n\ell$ -resolved cross sections	34
3.28	$Mg^{11+}+He \rightarrow Mg^{10+}+He^+$ n-resolved cross sections	34
3.29	$Mg^{10+}+X\rightarrow Mg^{9+}+X^+$ total cross sections	35
3.30	$Mg^{10+}+H\rightarrow Mg^{9+}+H^+$ $n\ell$ -resolved cross sections	35
3.31	$Mg^{10+}+H\rightarrow Mg^{9+}+H^+$ n-resolved cross sections	36
3.32	$Mg^{10+}+He \rightarrow Mg^{9+}+He^+$ $n\ell$ -resolved cross sections	36
3.33	$Mg^{10+}+He \rightarrow Mg^{9+}+He^+$ n-resolved cross sections	37
3.34	$Mg^{9+}+X\rightarrow Mg^{8+}+X^+$ total cross sections	37
3.35	$Mg^{9+}+H\rightarrow Mg^{8+}+H^+$ $n\ell$ -resolved cross sections	38
3.36	$Mg^{9+}+H\rightarrow Mg^{8+}+H^+$ $n\ell$ -resolved cross sections	39
3.37	$Mg^{9+}+H\rightarrow Mg^{8+}+H^+$ n-resolved cross sections	39
3.38	$Mg^{9+}+He \rightarrow Mg^{8+}+He^+$ $n\ell$ -resolved cross sections	40
3.39	$Mg^{9+}+He \rightarrow Mg^{8+}+He^+$ n-resolved cross sections	40
3.40	$Mg^{8+}+X\rightarrow Mg^{7+}+X^+$ total cross sections	41
3.41	$Mg^{8+}+H\rightarrow Mg^{7+}+H^+$ $n\ell$ -resolved cross sections	42
3.42	$Mg^{8+}+H\rightarrow Mg^{7+}+H^+$ n-resolved cross sections	42
3.43	$Mg^{8+}+He \rightarrow Mg^{7+}+He^+$ $n\ell$ -resolved cross sections	43
3.44	$Mg^{8+}+He \rightarrow Mg^{7+}+He^{+}$ n-resolved cross sections	43
4.1	μ vs. n — Fe^7+ NIST excitation energies	49
4.2	μ vs. n — Fe^7+ estimated and NIST excitation energies	50
4.3	$Fe^{9+}+X \rightarrow Fe^{8+}+X^+$ total cross sections	59
4.4	$Fe^{9+}+H\rightarrow Fe^{8+}+H^+$ n-resolved cross sections	60
4.5	$Fe^{9+}+H\rightarrow Fe^{8+}+H^+$ n-resolved cross sections.	60

4.6	$Fe^{9+}+H_2 \rightarrow Fe^{8+}+H_2^+$ $n\ell$ -resolved cross sections	61
4.7	$Fe^{9+}+H_2 \rightarrow Fe^{8+}+H_2^+$ n-resolved cross sections	61
4.8	$Fe^{9+}+He \rightarrow Fe^{8+}+He^{+}$ n-resolved cross sections	62
4.9	$Fe^{9+}+He \rightarrow Fe^{8+}+He^+$ n-resolved cross sections	62
4.10	$Fe^{9+}+H_2O\rightarrow Fe^{8+}+H_2O^+$ $n\ell$ -resolved cross sections	63
4.11	$Fe^{9+}+H_2O\rightarrow Fe^{8+}+H_2O^+$ n-resolved cross sections	64
4.12	$Fe^{9+}+CO \rightarrow Fe^{8+}+CO^+$ $n\ell$ -resolved cross sections	65
4.13	$Fe^{9+}+CO \rightarrow Fe^{8+}+CO^{+}$ n-resolved cross sections	65
4.14	$Fe^{9+}+CO_2 \rightarrow Fe^{8+}+CO_2^+$ $n\ell$ -resolved cross sections	66
4.15	$Fe^{9+}+CO_2 \rightarrow Fe^{8+}+CO_2^+$ n-resolved cross sections	66
4.16	$Fe^{9+}+N_2 \rightarrow Fe^{8+}+N_2^+$ $n\ell$ -resolved cross sections	67
4.17	$Fe^{9+}+N_2\rightarrow Fe^{8+}+N_2^+$ n-resolved cross sections	67
4.18	$Fe^{8+}+X\rightarrow Fe^{7+}+X^+$ total cross sections	68
4.19	$Fe^{8+}+H\rightarrow Fe^{7+}+H^+$ $n\ell$ -resolved cross sections	69
4.20	$Fe^{8+}+H\rightarrow Fe^{7+}+H^+$ n-resolved cross sections	69
4.21	$Fe^{8+}+H_2 \rightarrow Fe^{7+}+H_2^+$ $n\ell$ -resolved cross sections	70
4.22	$Fe^{8+}+H_2 \rightarrow Fe^{7+}+H_2^+$ n-resolved cross sections	70
4.23	$Fe^{8+}+He \rightarrow Fe^{7+}+He^{+}$ $n\ell$ -resolved cross sections	71
4.24	$Fe^{8+}+He \rightarrow Fe^{7+}+He^{+}$ n-resolved cross sections	71
4.25	$Fe^{8+}+H_2O\rightarrow Fe^{7+}+H_2O^+$ $n\ell$ -resolved cross sections	72
4.26	$Fe^{8+}+H_2O\rightarrow Fe^{7+}+H_2O^+$ n-resolved cross sections	72
4.27	$Fe^{8+}+CO \rightarrow Fe^{7+}+CO^{+}$ $n\ell$ -resolved cross sections	73
4.28	$Fe^{8+}+CO \rightarrow Fe^{7+}+CO^{+}$ n-resolved cross sections	74
4.29	$Fe^{8+}+CO_2 \rightarrow Fe^{7+}+CO_2^+$ $n\ell$ -resolved cross sections	75
4.30	$Fe^{8+}+CO_2 \rightarrow Fe^{7+}+CO_2^+$ n-resolved cross sections	75
4.31	$Fe^{8+}+N_2 \rightarrow Fe^{7+}+N_2^+$ $n\ell$ -resolved cross sections	76
4.32	$Fe^{8+}+N_2 \rightarrow Fe^{7+}+N_2^+$ n-resolved cross sections	76

5.1	Adiabatic potentials	80
5.2	Avoided crossings for channels 14–38	82
5.3	$Ne^{9+}+H\to Ne^{8+}+H^{+}$	83

LIST OF TABLES

3.1	Low-energy distribution function factors	20
3.2	$\mathrm{Ne^{10+} + He \rightarrow Ne^{9+} + He^{+}}$ MCLZ and CTMC $n\text{-}\mathrm{resolved}$ cross section differences	
	at 4550 eV/u	20
3.3	$Ne^{(8-10)+}$ Dominant Channels	44
3.4	$Mg^{(8-12)+}$ Dominant Channels	45
4.1	Fe VIII (Fe ⁷⁺) NIST Atomic Energies	47
4.1	Fe VIII (Fe ⁷⁺) NIST Atomic Energies	48
4.2	Fe VIII (Fe $^{7+}$) NIST Term Energies: Singly-Excited Doublets	49
4.3	Fe VIII (Fe ⁷⁺) Term Energies: Estimated and NIST	51
4.3	Fe VIII (Fe ⁷⁺) Term Energies: Estimated and NIST	52
4.4	Fe IX (Fe ⁸⁺) NIST Atomic Energies	53
4.4	Fe IX (Fe ⁸⁺) NIST Atomic Energies	54
4.5	Fe IX (Fe ⁸⁺) Singlet Term Energies: Estimated and NIST	55
4.5	Fe IX (Fe ⁸⁺) Singlet Term Energies: Estimated and NIST	56
4.6	Fe IX (Fe ⁸⁺) Triplet Term Energies: Estimated and NIST	57
4.6	Fe IX (Fe ⁸⁺) Triplet Term Energies: Estimated and NIST	58
4.7	Degeneracy Factors	59
4.8	Fe ⁽⁸⁻⁹⁾⁺ Dominant Channels	77
4.8	$Fe^{(8-9)+}$ Dominant Channels	78
5.1	MRDCI Potentials (singlets)	81
5.1	MRDCI Potentials (singlets)	82
5.2	MOCC Single Electron Capture Cross Sections	84

Chapter 1

Introduction

With continual improvements in X-ray detector technology from charge-coupled devices (CCDs) to the reflection grating spectrometer (RGS) available on the current fleet of X-ray satellites (*Chandra, XMM-Newton, Suzaku*), the resolution of X-ray spectra have dramatically improved allowing for detailed studies of line formation mechanisms. While X-ray lines from highly ionized plasmas are primarily produced by electron impact excitation (EIE) in collisionally ionized equilibrium (CIE) or via electron radiative recombination (RR) in photoionized environments, a third mechanism, charge-exchange (CX) induced X-ray emission, has been found to be important in situations where hot plasmas meet cold gas.

The importance of CX as a mechanism for producing X-ray emission was recognized from studies of the Jovian aurora as early as the 1980s (e.g., Cravens et al. 1995, and references therein), but it was the detection of cometary X-ray emission (Lisse et al. 1996), and later its possible contribution to the soft X-ray background (Cox 1998; Cravens 2000) which brought CX induced emission to the attention of the high-energy astrophysics community. More recently, CX has been invoked for a host of environments, from supernova remnants (Katsuda et al. 2011; Cumbee et al. 2014, 2016) to extragalactic cooling flows (Fabian et al. 2011), in attempts to explain "anomalous" X-ray emission features which are unlikely to be attributable to EIE or RR. Unfortunately, the current CX cross sectional data are of insufficient reliability or availability to allow for quantitative spectroscopic models. To partially address this situation, cross sections, as a function of kinetic energy, for a series of single electron capture (SEC) collision systems are calculated here using the multi-channel Landau-Zener (MCLZ) (Janev et al. 1983; Butler and Dalgarno 1980) and Molecular Orbital

Close-Coupling (MOCC) methods. Theoretical summaries of these methods are presented in Chapter 2.

Chapter 3 discusses the study of $Ne^{(8-10)+}$ and $Mg^{(8-12)+}$ colliding with neutral H and He resulting in single electron capture. The resulting cross sections are calculated over a range of energies from 10^{-1} – 10^{5} eV/u. The MCLZ method is used since it is reasonably accurate for kinetic energies $\lesssim 10 \text{ keV/u}$, and computation effort is minimal which allows several collision systems to be studied, benchmarking their results to other data when available. In many of these cases, explicit experimental or theoretical CX data are lacking. Collisional ionization, not included in the MCLZ model, begins to become important, and eventually dominates, at higher energies.

Chapter 4 discusses $Fe^{(8-9)+}$ in collisions with H, H₂, He, H₂O, CO, CO₂, and N₂. For the same reasons with Ne and Mg, the MCLZ method is used to calculate the cross sections of collisions over a range of energies from 10^{-1} – 10^{5} eV/u. For Fe⁹⁺, multiple calculations are performed on each collision system as dictated by Wigner-Witmer rules (Wigner and Witmer 1928) describing the symmetries of the scattering channels. Cross section calculations are performed for singly-excited $n\ell$ -resolved quantum states. Cross sections are also calculated for core-excited states when those energies are available. Excitation energies are estimated only for singly-excited states when they are not initially available.

SEC cross sections for these collision systems— $Fe^{8+}+H_2O$, $Fe^{9+}+H_2O$, $Fe^{8+}+CO$, $Fe^{9+}+CO$, $Fe^{9+}+CO$, $Fe^{9+}+CO$, $Fe^{9+}+CO$, and $Fe^{9+}+CO$, $Fe^{9+}+CO$, and $Fe^{9+}+CO$, $Fe^{9+}+CO$

In Chapter 5, Ne⁹⁺+H is studied using MOCC. Cross sections comparision are made with existing data and discussed.

Conclusions are given in Chapter 6. An Appendix discusses the implementation of the MCLZ method in a new computational package, *Stückelberg*. Atomic units are used unless otherwise indicated.

Chapter 2

THEORY

2.1 Landau-Zener ¹

The interaction of two particles where single electron capture charge exchange occurs can be described by

$$X^{q+} + Y(1s) \to X(n, \ell)^{(q-1)+} + Y^{+} + E,$$
 (2.1)

where X is a positively charged ion, Y is a neutral atom or molecule, q is the ionic charge, n is the principal quantum number, and ℓ is the angular momentum quantum number.

In the Landau-Zener model, the difference between ionization potential of the two particles can be written as

$$\Delta E = I(X^{(q-1)+}) - I(Y). \tag{2.2}$$

The polarization potential of the dominant long-range interaction between X and Y is

$$V_p = -\frac{\alpha q^2}{2R^4},\tag{2.3}$$

where R is the separation, or internuclear distance, in atomic units, and α is the polarizability of the neutral target Y. According to Schwerdtfeger and Nagle (2018), if Y=H (hydrogen), then $\alpha=4.5$; if Y=He (helium), then $\alpha=1.383191$.

$$V_c = \frac{q-1}{R}. (2.4)$$

Plots of equations 2.2, 2.3, and 2.4 are shown in Figure 2.1.

 $^{^{1}\}mathrm{Child}$ (2010); Butler and Dalgarno (1980); Janev et al. (1983)

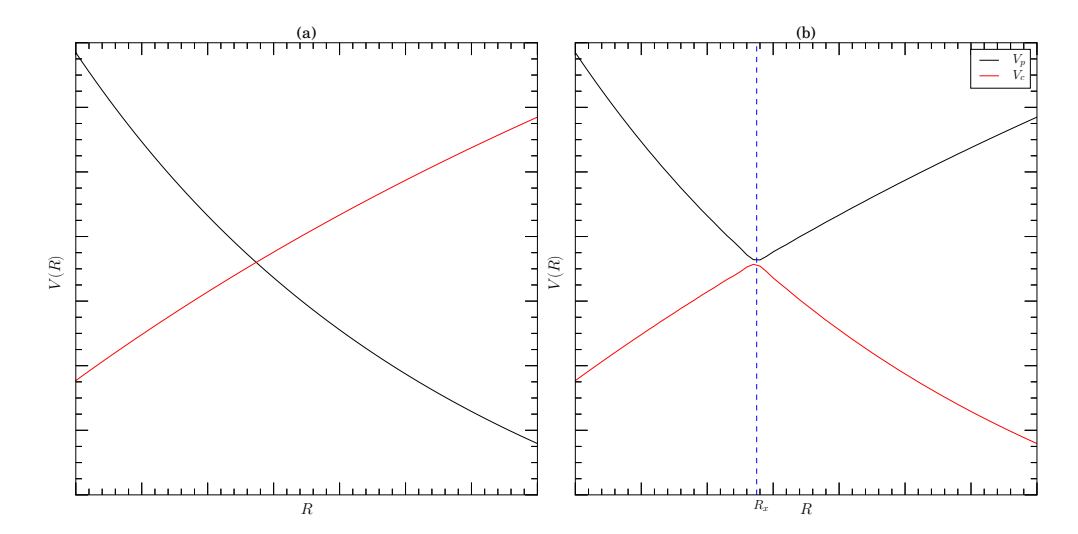


Figure 2.1: Polarization (V_p) and Coulomb (V_c) potentials.

(a) diabatic crossing; (b) adiabatic avoided crossing at R_x .

According to Butler and Dalgarno (1980), an avoided crossing occurs at R_x , which occurs where the potential curves are at, or near, the minimum distance between them. The probability of a transition occurring during a pass through R_x , according to the Landau-Zener approximation, is $\mathcal{P} = e^{-\omega}$, where

$$\omega = \frac{4\pi^2 [H_{12}(R_x)]^2}{hv(R_x) \left| \frac{d}{dR} (H_{11} - H_{22}) \right|_{R_x}}.$$
 (2.5)

H are elements of the potential matrix, and v is the radial component of the relative velocity of the collision. The separation of the adiabatic curves at R_x is

$$\Delta U(R_x) = 2H_{12}(R_x). \tag{2.6}$$

The cross section at an energy E_i of relative motion is given by

$$Q(E_i) = 4\pi R_x^2 p(1+\lambda) \int_1^\infty e^{-\eta x} \times \left[1 - e^{-\eta x}\right] x^{-3} dx, \qquad (2.7)$$

where

$$\eta = \frac{2\pi^3 M \left[\Delta U(R_x)\right]^2}{k_i h^2 \sqrt{1+\lambda} \left| \frac{d}{dR} \left(H_{11} - H_{22} \right) \right|}.$$
 (2.8)

Critical parameters in the LZ formula are R_x , and $\Delta U(R_x)$, $\frac{d}{dR}(H_{11} - H_{22})$ evaluated at R_x . The probability that the collision initially proceeds along the energy surface H_{11} is p. $k_i = \frac{Mv}{\hbar}$. And $\lambda = \frac{H_{11}(\infty) - H_{11}(R_x)}{E_i}$.

The internuclear distance where the interaction takes place in a final n-state channel is given by

$$R_n = \frac{n^2 (Z - 1)}{Z^2 - n^2} \left(1 + \sqrt{1 - \frac{3n (n - 1) (Z^2 - n^2)}{n^2 Z (Z - 1)^2}} \right).$$
 (2.9)

For n < Z, Equation 2.9 can be written as

$$R_n \simeq \frac{2n^2(Z-1)}{Z^2 - n^2},$$
 (2.10)

which is only valid for one-electron systems.

In the two-channel Landau-Zener method, the probability of an interaction occurring is denoted by p_n . In consideration of the multi-channel case, where the initial state interacts strongly with N final product states, where it assumed there are no interferences between transitions (p_k, p_{k+1}) and (p_k, q_k) , the probability a particular ionic level n will be populated after the collision is given by

$$P_{n} = p_{1}p_{2}...p_{n} (1 - p_{n}) \left[1 + (p_{n+1}p_{n+2}...p_{N})^{2} + (p_{n+1}p_{n+2}...p_{N-1})^{2} (1 - p_{N})^{2} (1 - q_{N}) + (p_{n+1}p_{n+2}...p_{N-2})^{2} (1 - p_{N-1})^{2} (1 - q_{N-1}) + ... + p_{n+1}^{2} (1 - p_{n+2}^{2})^{2} (1 - q_{n+2}) + (1 - p_{n+1})^{2} (1 - q_{n+1}) + p_{1}p_{2}...p_{n-1} (1 - p_{n})^{2} q_{n}.$$

$$(2.11)$$

The multichannel Landau-Zener theory is obtained by setting $q_k=0$ for k=1,...,N, in Equation 2.11. Partial cross sections are given by

$$\sigma_n = 2\pi \int_0^{R_n} P_n b db, \tag{2.12}$$

where b is the impact parameter. The total cross section is

$$\sigma = \sum_{n=1}^{N} \sigma_n. \tag{2.13}$$

2.2 Molecular Orbital Close Coupling ²

The Schrödinger equation of a system described by Equation 2.1 can be written as

$$\left[-\sum_{k=1}^{2} \frac{1}{2} \nabla_{s_{k}}^{2} + V(s_{1}, s_{2}, R) - \epsilon_{i}(R) \right] \psi_{i}(s_{1}, s_{2}, R) = 0,$$
(2.14)

where R is the internuclear distance, s_k are the electronic coordinates with respect to the center if mass of the system, and the molecular orbitals, ψ_i , are orthonormal solutions. The total wave function is the sum of the molecular orbitals, such that

$$\Psi = \sum_{i} \psi_{i}(s_{1}, s_{2}, R) F_{i}(R). \qquad (2.15)$$

From Equation 2.14, a set of coupled differential equations is obtained:

$$\[\frac{\partial^2}{\partial R^2} - \frac{\hat{J}_i^2 - \Lambda_i^2}{R^2} \] RF_i(R) = \sum_j \left[V_{ij}^2(R) + V_{ij}^C(R) \right] RF_j(R) , \qquad (2.16)$$

where \hat{J}_i^2 is the total angular momentum operator, Λ_i is the projection of electronic angular momentum onto R for the ith molecular orbital, and the total energy is E.

²Bransden and McDowell (1992)

The nonadiabatic radial coupling,

$$V_{ij}^{R}(R) = -2\left\langle i \left| \frac{\partial}{\partial R} \right| j \right\rangle \frac{\partial}{\partial R} \delta_{\Lambda_{i}\Lambda_{j}}, \tag{2.17}$$

gives rise to transitions between states with the same symmetry $^{2S+1}\Lambda$. And the nonadiabatic rotational coupling,

$$V_{ij}^{C}(R) = \frac{2i}{R^{2}} \langle i | L_{y} | j \rangle \frac{\partial}{\partial \Theta}, \qquad (2.18)$$

couples states of different symmetry. L_y is the y-component of the electronic angular momentum where the z-axis lies along the R-vector. Θ is the angle of rotation of R about the y-axis. The wave function states $\psi_i(s_1, s_2, R)$ are denoted by $|i\rangle$.

A diabatic transformation of the amplitudes $F_i(R)$ leads to

$$F_i(R) = \sum_j C_{ij}(R) G_j(R).$$
 (2.19)

When $C_{ij}(R)$ are obtained from

$$\frac{d}{dR}C_{ij}(R) + \sum_{k} \left\langle i \left| \frac{\partial}{\partial R} \right| k \right\rangle C_{kj}(R) = 0, \qquad (2.20)$$

the radial coupling matrix elements vanish. This leads to a complete basis when the second order derivative matrix elements in Equation 2.20 (Bransden and McDowell 1992; Heil and Dalgarno 1979) are neglected since they are typically small. A partial wave expansion of diabatic amplitudes $G_j(R)$ gives

$$\left[\frac{\partial^{2}}{\partial R^{2}} + \frac{\Lambda_{i}^{2} - J(J+1)}{R^{2}} + 2\mu E\right] g_{i}^{J}(R) = \sum_{jk} \left[{}^{d}V_{ij}^{C}(R) + 2\mu C_{ik}^{\dagger}(R) \epsilon_{k}(R) C_{kj}(R)\right] g_{j}^{J}(R).$$
(2.21)

The K^J matrix is then obtained by solving these equations using the multichannel logderivative method (Johnson 1973) and fitting the ion-neutral and Coulomb channel coefficients to spherical Bessel functions and Coulomb functions, respectively, in the asymptotic limit. The S^J matrix is related to the K^J matrix by

$$S^{J} = [I + iK^{J}] [I - iK^{J}]^{-1}, \qquad (2.22)$$

from which the cross sections are given:

$$\sigma_{ji} = \frac{\pi p_0}{2\mu \left(\epsilon_i(R) - E\right)} \sum_{J} (2J + 1) \left| S_{ij}^J \right|^2,$$
 (2.23)

where p_0 is the approach probability factor. For singlet molecular states, $p_0=1/4$; and for triplets, $p_0=3/4$.

Chapter 3

 $\mathrm{NE}^{(8-10)+}$ and $\mathrm{MG}^{(8-12)+}$ with H and He using MCLZ^1

3.1 Introduction

Many physical phenomena can be modeled by a two-level system (TLS) consisting of two interacting states (Nakamura 2002). The strength of the interaction can be varied typically by some external parameter such that the internal state energies of the quantum TLS exhibit an avoided-level crossing. Some physical property of the two states is typically exchanged when passing from one side of the avoided crossing to the other. In such a case, the system undergoes a nonadiabatic transition between the two energy states. Nonadiabatic interactions were first discussed by Landau (1932), Zener (1932), and Stückelberg (1932). In the current study, the control parameter is the distance R between an incident ion and a target neutral which interact during a charge exchange collision process (Equation 2.1), where an electron is transferred from the neutral target to a highly-ionized ion. Application of a TLS analysis to charge transfer systems is commonly referred to as the Landau-Zener (LZ) method. Here we apply a series of TLS crossings via the LZ approach of Butler and Dalgarno (1980) with the multichannel formalism of Janev et al. (1983).

For all collision systems, the first step in the MCLZ approach is to estimate the avoided crossing distances $R_{\rm x}$ between the incoming and outgoing channels. Beginning with atomic energies available from the NIST Atomic Spectral Database (Kramida et al. 2018), the crossings are estimated and then used to predict the adiabatic potential splitting at the crossing, $\Delta U(R_{\rm x})$, using the Olson and Salop (1977) radial coupling model for product

¹Lyons, David A., Cumbee, Renata S., and Stancil, Phillip C., 2017. Charge Exchange of Highly Charged Ne and Mg Ions with H and He, *The Astrophysical Journal*, Vol. 232, No. 2, 23 October 2017.

hydrogen-like ions. In the case of multielectron ions, the Olson-Salop-Tauljberg (Taulbjerg 1986) radial coupling approximation is adopted. The rotational coupling model of Janev et al. (1983) is included for hydrogen-like product ion systems, but only the radial coupling is considered for multielectron ions. In addition to $R_{\rm x}$ and $\Delta U(R_{\rm x})$, a third LZ parameter, the difference in slopes of the diabatic potentials at $R_{\rm x}$ is obtained analytically from empirical molecular potentials for the collision complexes following Butler and Dalgarno (1980).

In most cases, each individual $n\ell$ or $n\ell S$ -resolved SEC cross section is calculated directly with the MCLZ method. However, if the ion is initially bare, then the SEC cross sections for the angular momentum states in each n-shell are estimated using analytical ℓ -distribution functions (see, for example, Krasnopolsky et al. 2004; Smith et al. 2014). ℓ -distribution functions are necessary in such cases due to the ℓ -level degeneracy in a given n-manifold. Unfortunately, this introduces considerable uncertainty in the $n\ell$ -resolved cross sections as will be illustrated below.

Here, the statistical distribution function is considered,

$$W_{nl}^{\text{st}} = \frac{2l+1}{n^2};$$
 (3.1)

and the low-energy distribution (Abramov et al. 1978; Krasnopolsky et al. 2004),

$$W_{nl}^{\text{le}} = (2l+1) \frac{[(n-1)!]^2}{(n+l)!(n-1-l)!}.$$
(3.2)

The statistical distribution function is believed to be valid for energies above $\sim 5-10 \text{ keV/u}$, while for lower energies, the low-energy distribution function is preferred (Krasnopolsky et al. 2004; Cumbee et al. 2016; Mullen et al. 2016).

For some ions, experimental or theoretical energy level data for high-lying Rydberg states are lacking. In such instances, the ion energies are estimated with a variant of the quantum defect method (Connerade 1998; Mullen et al. 2016) and polynomial extrapolations from available energy data (Kramida et al. 2018). While advanced atomic structure calculations

can be performed, the goal is to utilize available recommended data with quick extrapolations.

3.2 SINGLE ELECTRON CAPTURE CROSS SECTIONS

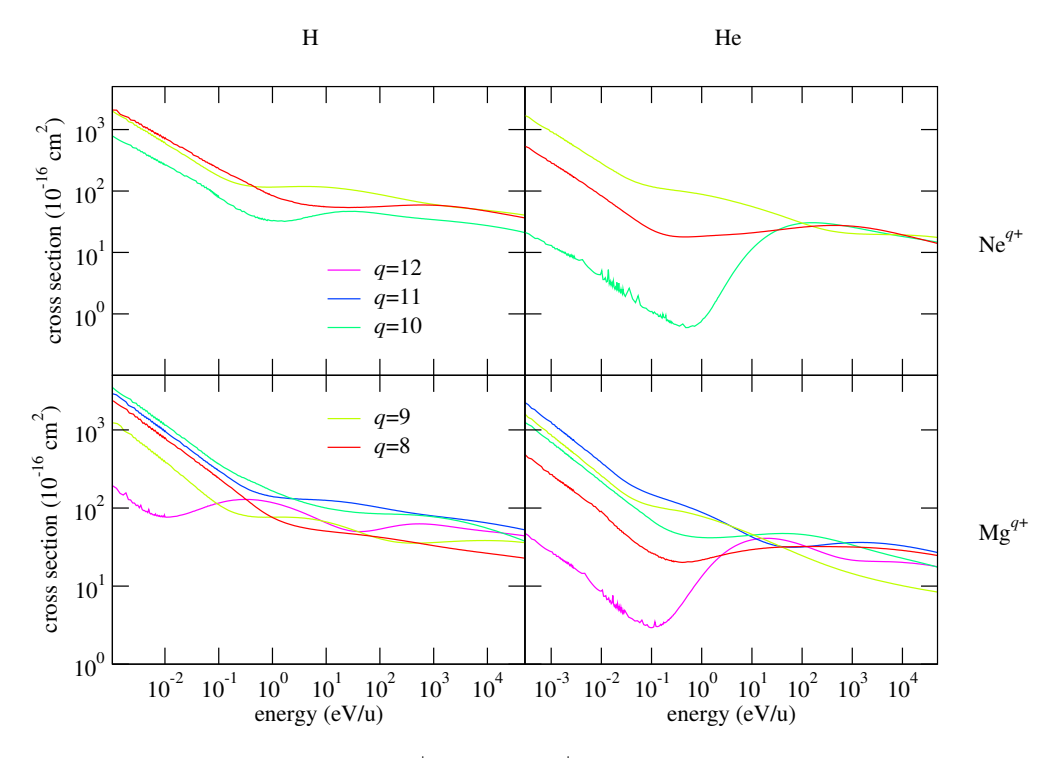


Figure 3.1: Ne^{q+} and Mg^{q+} total cross sections.

For collisions with hydrogen (H) and helium (He) for q=8-12 using the MCLZ method.

Total MCLZ charge exchange cross sections for all systems studied in this chapter are presented in Figure 3.1. The total cross sections for both H and He targets generally converge at high collision energies to within a factor of ~ 5 , but diverge for $E \lesssim 1-10$ eV/u. At low kinetic energies, all cross sections go to the Langevin limit, increasing as $1/E^{1/2}$ with decreasing kinetic energy. Collisions with bare ions give the smallest cross sections since the interaction results in a smaller number of final channels, degenerate for a given n. Details on each collision system are given below with comparison to available theoretical or experimental results.

3.3 NE^{10+}

Of all the ions considered here, Ne¹⁰⁺ has received the most attention, being the subject of numerous theoretical and experimental studies for the past 40 years. Unfortunately, this is not the case for most of the other ion-atom collision systems. Total MCLZ SEC cross sections for Ne¹⁰⁺+H and Ne¹⁰⁺+He are presented in Figure 3.2.

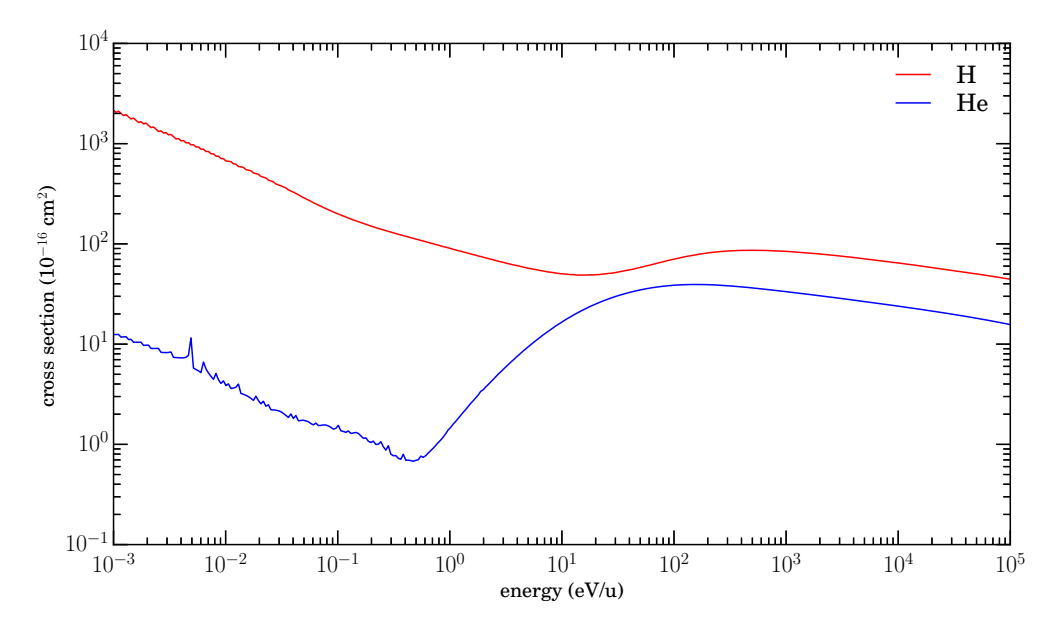


Figure 3.2: $Ne^{10+}+X\rightarrow Ne^{9+}+X^+$ total cross sections.

Additional details for Ne¹⁰⁺+X, where X=H, are given in Section 3.3.1; and for X=He, Section 3.3.2.

$3.3.1 \text{ NE}^{10+} + \text{H}$

For Ne¹⁰⁺+H, the $n\ell$ -resolved cross sections are calculated using the low-energy (Figure 3.3) and statistical (Figure 3.4) distribution functions. These figures also show comparison to classical trajectory Monte Calro (CTMC) data from Schultz and Kristić (1996) for n=5, n=6, and n=7.

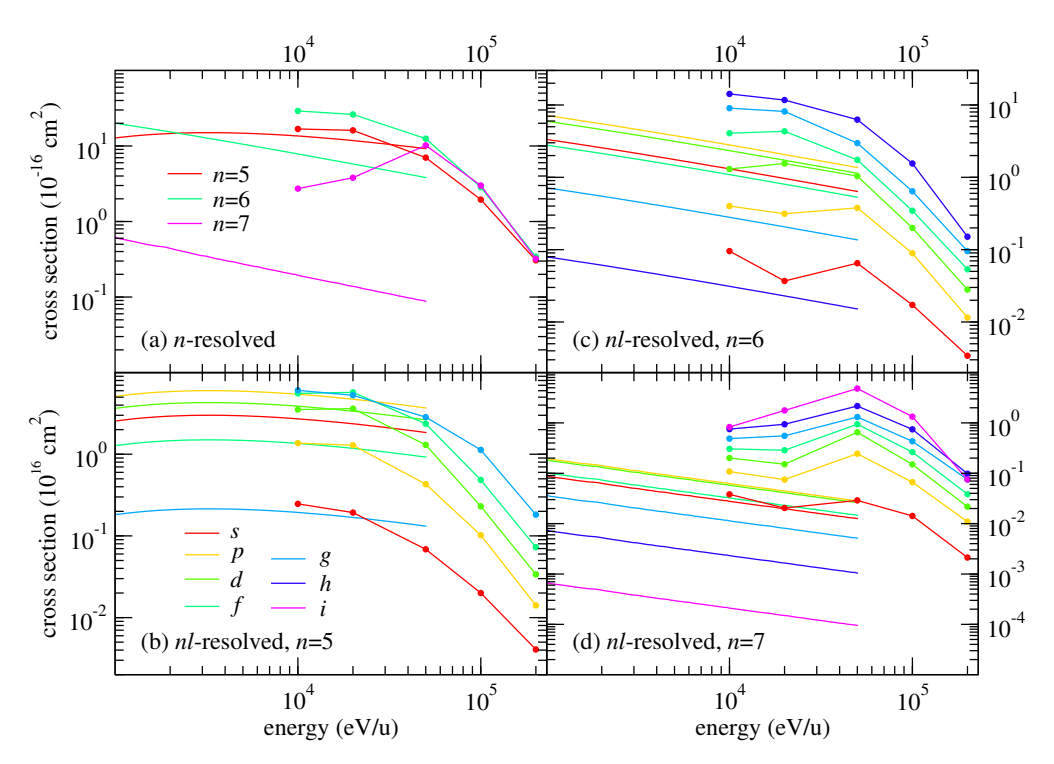


Figure 3.3: $Ne^{10+}+H\rightarrow Ne^{9+}+H^+$ $n\ell$ -resolved (low-energy) cross section comparisons. MCLZ (lines); CTMC (Schultz and Kristić 1996) (lines with circles).

For n=5 and n=6, the cross sections are within an order of magnitude of those of Schultz and Kristić (1996). In fact, in the lower range of the data, n=5 is very similar to Schultz and Kristić (1996), and in the $n\ell$ -resolved case, they can be seen to be in close agreement. However, Figure 3.3 (b) shows the correspondence between the ℓ states of each method to be out of order. The MCLZ states, from highest to lowest are ordered: d, p, s, f, and g, while for Schultz and Kristić (1996), they are arranged as: g, f, d, p, and s, i.e., the latter follow a statistical distribution, though it is expected that for energies less than 1 keV/u, the ℓ distribution should follow more closely the low-energy distribution form. A similar phenomenon appears in graphs (c) and (d).

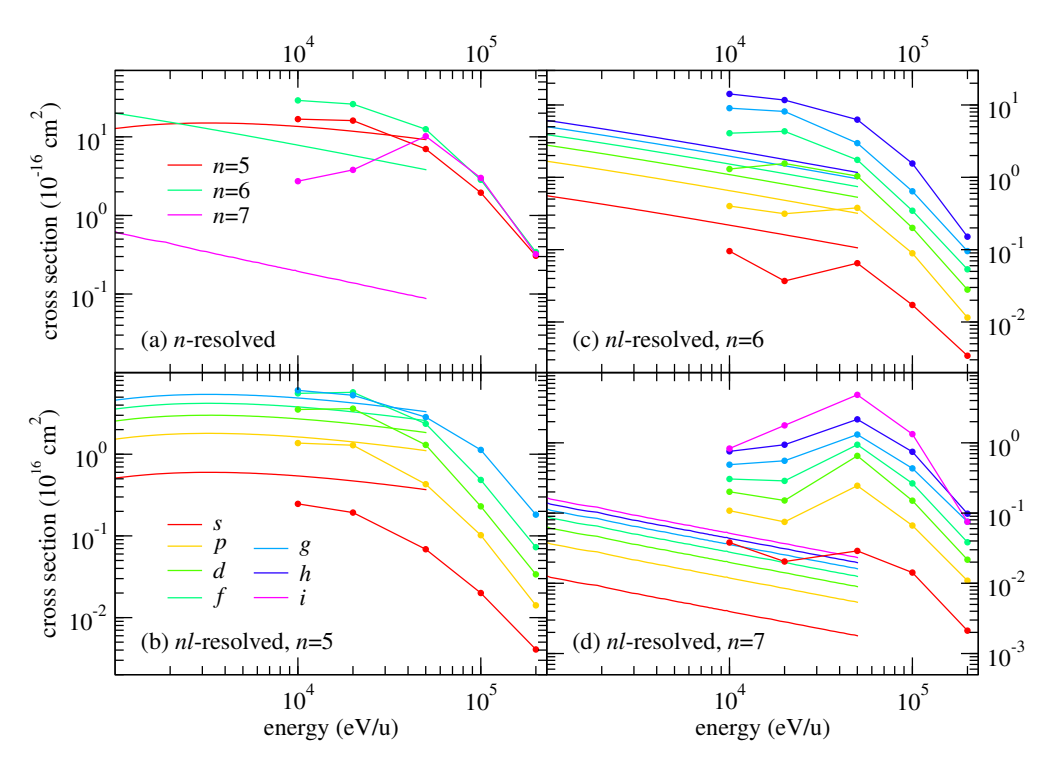


Figure 3.4: $Ne^{10+}+H\rightarrow Ne^{9+}+H^+$ $n\ell$ -resolved (statistical) cross section comparisons. MCLZ (lines); CTMC (Schultz and Kristić 1996) (lines with circles).

As a consequence, the MCLZ $n\ell$ -resolved statistical cross sections, as shown in Figure 3.4, are in better agreement with the CTMC results (Schultz and Kristić 1996), as might be expected. It should be noted that 10 keV/u corresponds to the region where the applicability of both methods, MCLZ and CTMC, begins to be questionable, i.e. MCLZ is expected to be reliable for lower kinetic energies and CTMC for higher energies, likewise, the statistical ℓ -distribution is likely valid at 10 keV/u, while the low-energy distribution may be expected to be reasonable below 1 keV/u. How the transition should be made from statistical to low-energy, and at what kinetic energy, is unknown.

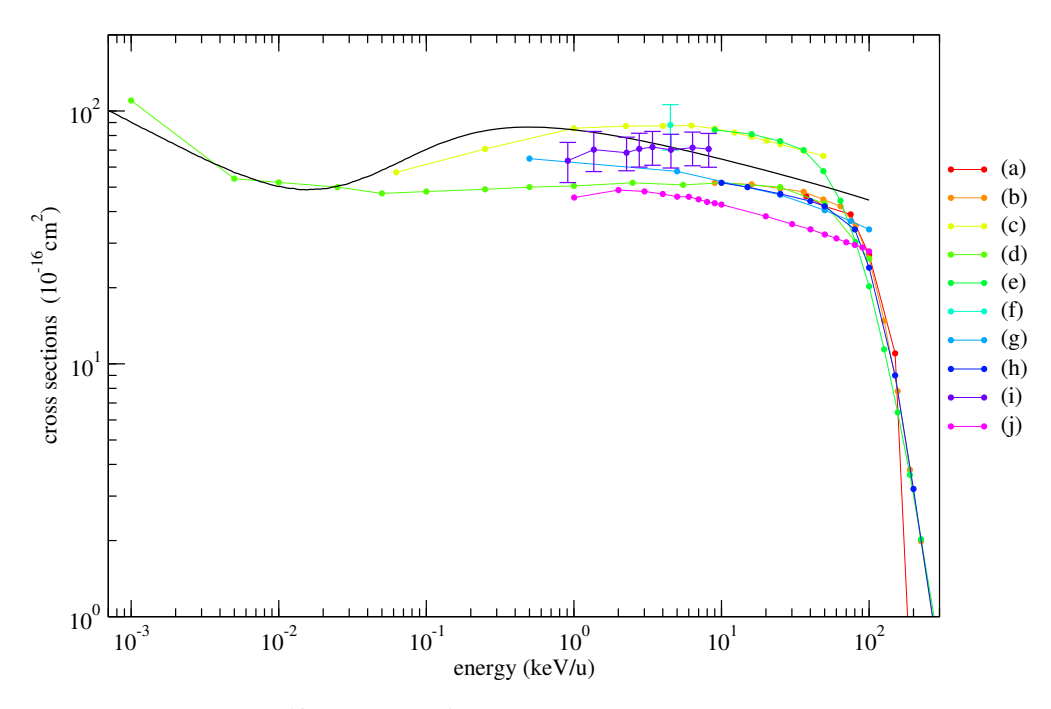


Figure 3.5: $Ne^{10+}+H\rightarrow Ne^{9+}+H^+$ total cross section comparison.

MCLZ - solid black line; (a) CTMC (Olson and Salop 1977); (b) CTMC microcanonical (Errea et al. 2004); (c) OEDM (Errea et al. 2004); (d) CTMC (Perez et al. 2001); (e) CTMC hydrogenic (Errea et al. 2004); (f) experimental (Bendahman et al. 1985); (g) theory (Grozdanov 1980); (h) CTMC (Maynard et al. 1992); (i) experimental (Meyer et al. 1985); (j) CTMC (Schultz and Kristić 1996)

In Figure 3.5, the total MCLZ cross section for Ne¹⁰⁺+H is compared to other calculations and experimental data. It can be seen that the MCLZ results are very close to those obtained by other methods. These comparisons suggest that the MCLZ method is sufficiently accurate in the domain of $10^0 - 10^5$ eV/u.

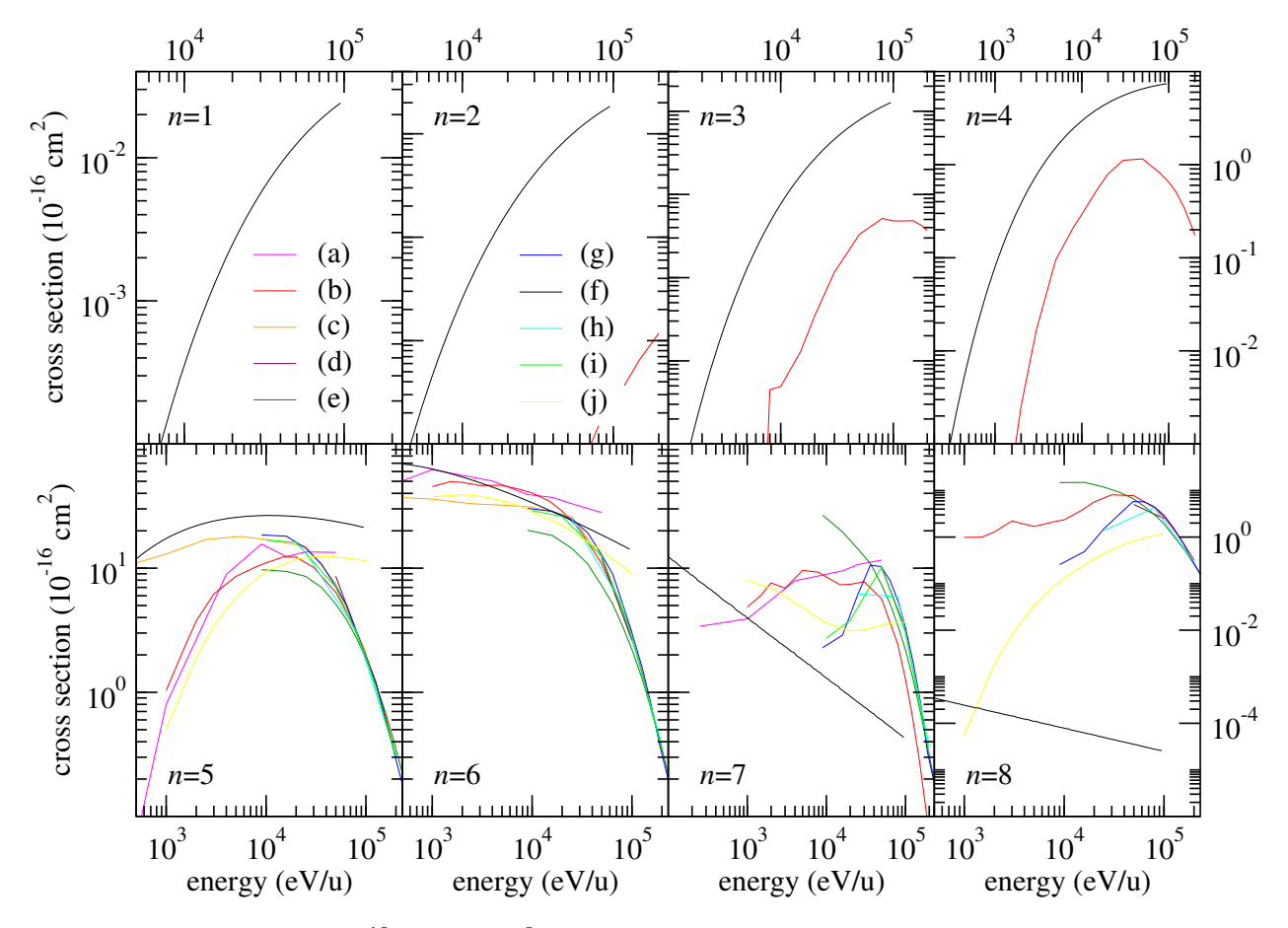


Figure 3.6: $Ne^{10+}+H\rightarrow Ne^{9+}+H^+$ n-resolved cross section comparison.

(a) Bendahman et al. (1985); (b) AOCC (Cumbee et al. 2016); (c) CTMC (Perez et al. 2001); (d) CTMC (Olson and Salop 1977); (e) CTMC hydrogenic (Errea et al. 2004); (f) current MCLZ; (g) CTMC microcanonical (Errea et al. 2004); (h) CTMC (Maynard et al. 1992); (i) OEDM (Errea et al. 2004); (j) CTMC (Schultz and Kristić 1996).

MCLZ n-resolved cross sections are compared to available data, as presented in Figure 3.6. For each cross section, there are atomic orbital close-coupling (AOCC) data available for comparison (Cumbee et al. 2016), but in the cases of n=1 and n=2, the AOCC cross sections are significantly smaller, being off the scale of the plots. For n=4, the MCLZ cross section comes within an order of magnitude of the AOCC calculation. While for n=5 and n=6, the MCLZ and AOCC cross sections overlap at higher energies. Compared to other data, n=5 gives the closest agreement, especially around 20-30 keV/u compared to the measurements of Bendahman et al. (1985) and the CTMC calculations of Perez et al. (2001). The results

for n=6 are somewhat smaller than all previous results, while the n=7 and 8 cross sections are underestimates, again due to the lack of short-range couplings in the MCLZ model. The underestimation of the MCLZ n=6 cross section accounts for most of the discrepancy in the total cross section given in Figure 3.5.

$3.3.2 \text{ NE}^{10+} + \text{HE}$

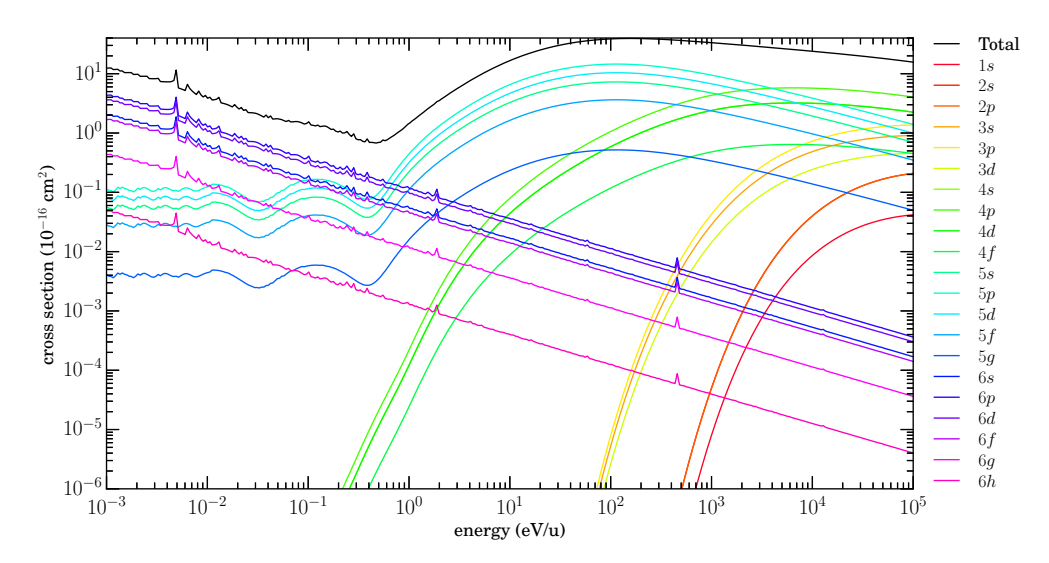


Figure 3.7: $Ne^{10+}+He\rightarrow Ne^{9+}+He^+$ $n\ell$ -resolved cross sections.

Low-energy distribution function.

MCLZ $n\ell$ -resolved cross sections for Ne¹⁰⁺+He are presented in Figure 3.7 (low-energy distribution function) and Figure 3.8 (statistical distribution function).

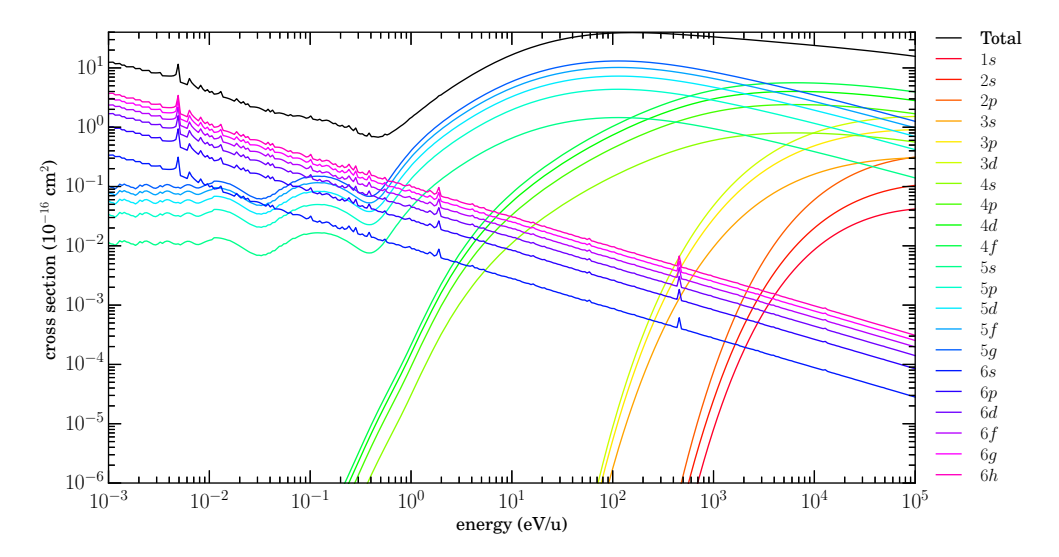


Figure 3.8: $Ne^{10+}+He\rightarrow Ne^{9+}+He^+$ $n\ell$ -resolved cross sections.

Statistical distribution function.

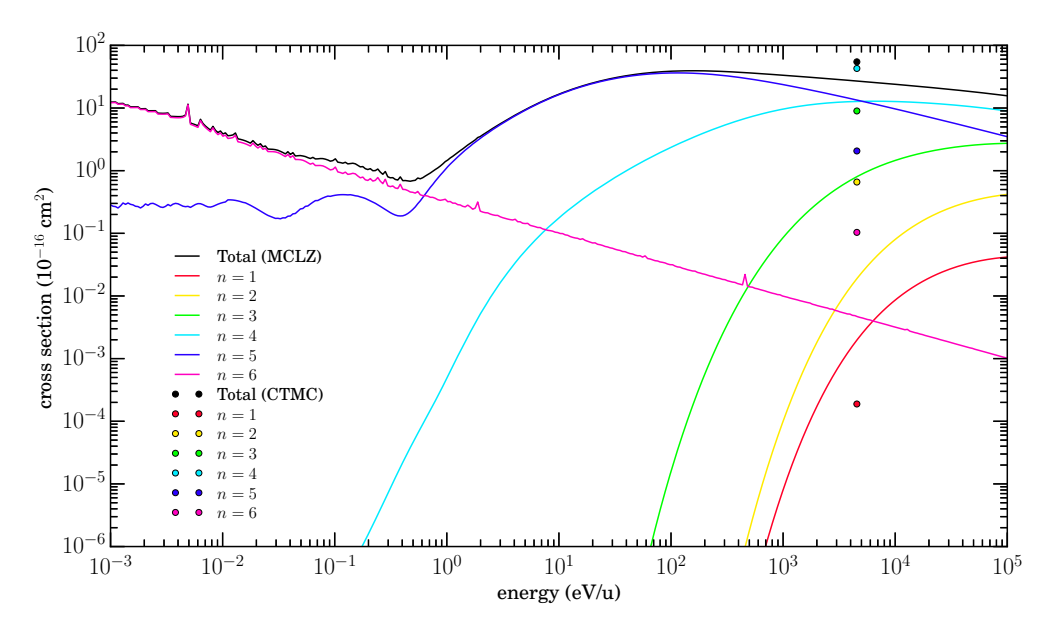


Figure 3.9: $Ne^{10+}+He\rightarrow Ne^{9+}+He^+$ *n*-resolved cross sections.

MCLZ comparison to the CTMC cross sections of Ali et al. (2010).

Figure 3.9 shows n-resolved cross sections. Comparison is made at 4550 eV/u, to the CTMC results of Ali et al. (2010) where general agreement is seen with the current MCLZ calculations, both indicating that the dominant capture channels are n=4, 5, and 6, but with

Table 3.1. Low-energy distribution function factors

	n=1	n=2	n=3	n=4	n=5	n=6	n=7	n=8
$\begin{array}{c} \ell = 0 \\ \ell = 1 \\ \ell = 2 \\ \ell = 3 \\ \ell = 4 \\ \ell = 5 \end{array}$	1.00e+00	5.00e-01 5.00e-01	3.33e-01 5.00e-01 1.67e-01	2.50e-01 4.50e-01 2.50e-01 5.00e-02	2.00e-01 4.00e-01 2.86e-01 1.00e-01 1.43e-02	1.67e-01 3.57e-01 2.98e-01 1.39e-01 3.57e-02 3.97e-03	1.43e-01 3.21e-01 2.98e-01 1.67e-01 5.84e-02 1.19e-02	1.25e-01 2.92e-01 2.92e-01 1.86e-01 7.95e-02 2.24e-02
$\substack{\ell=6\\\ell=7}$							1.08e-03	3.79e–03 2.91e–04

Table 3.2. $Ne^{10+}+He\rightarrow Ne^{9+}+He^+$ MCLZ and CTMC n-resolved cross section differences at 4550 eV/u.

Channel	MCLZ	CTMC	% Difference
Total	$2.6981e{+01}$	$5.4636 \mathrm{e}{+01}$	67.677
$n{=}1$	1.9726e-03	1.8858e-04	165.10
$n{=}2$	1.8877e-02	6.5847e - 01	96.555
n=3	8.0112e-01	$8.9748\mathrm{e}{+00}$	167.22
$n{=}4$	$1.2729\mathrm{e}{+01}$	$4.2818\mathrm{e}{+01}$	42.818
$n{=}5$	$1.3414\mathrm{e}{+01}$	$2.0630 \mathrm{e}{+00}$	146.68
n=6	$4.7142 \mathrm{e}{-03}$	1.0353e-01	182.58

different ordering. This is due to the low-energy distribution function (Equation 3.2), which produces the factors shown in Table 3.1. The statistical distribution function (Equation 3.1) will produce factors which increase with ℓ for all n. It should be noted that the MCLZ method is approaching its range of applicability at our high energy limit, while the CTMC results approach their low energy validity range (i.e., the uncertainty in both CTMC and MCLZ are expected to be relatively high at this collision energy). The differences between these two sets of data are listed in Table 3.2.

$3.4~{ m NE}^{9+}$

Total MCLZ SEC cross sections for $Ne^{9+}+H$ and $Ne^{9+}+He$ are presented in Figure 3.10.

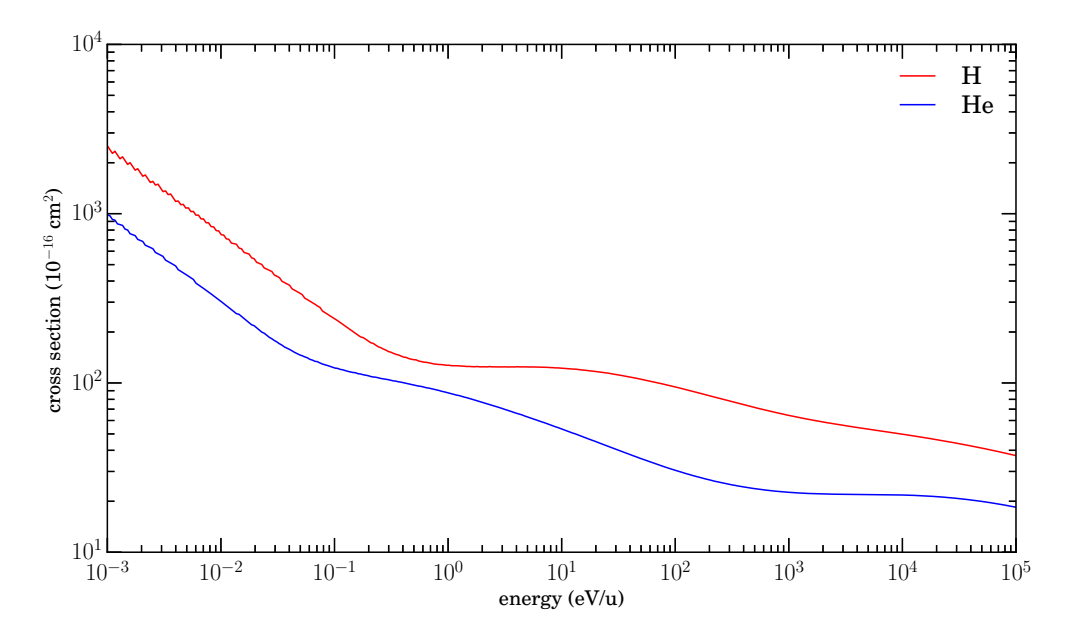


Figure 3.10: $Ne^{9+}+X\rightarrow Ne^{8+}+X^+$ total cross sections.

Additional details for Ne⁹⁺+X, where X=H, are given in Section 3.4.1; and for X=He, Section 3.4.2.

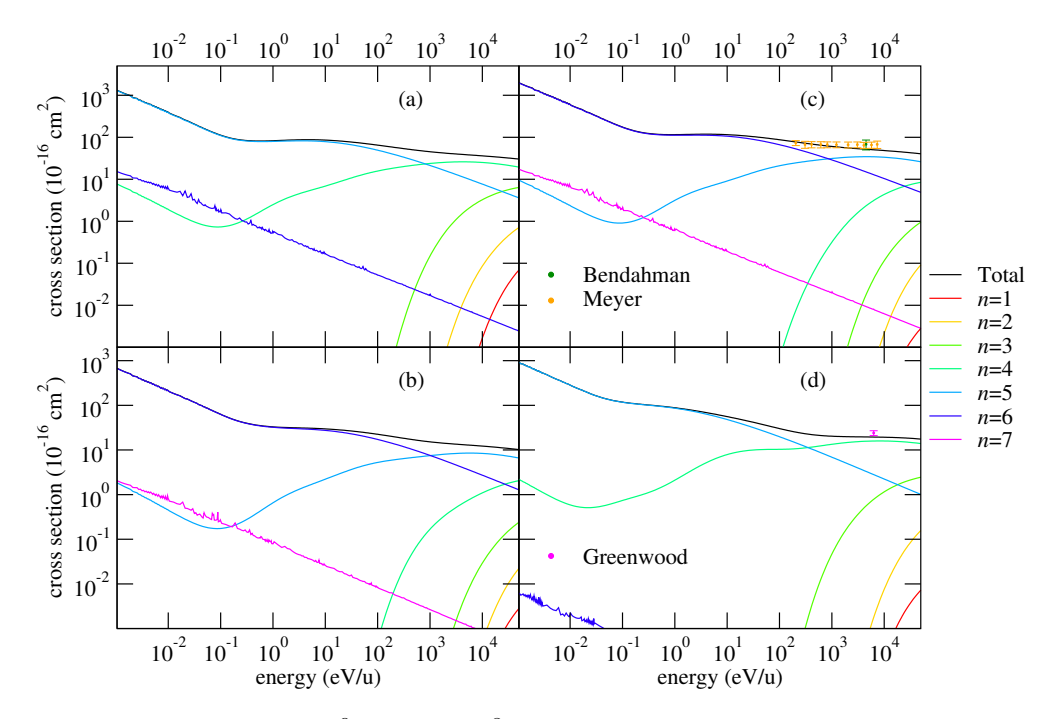


Figure 3.11: $Ne^{9+}+X\rightarrow Ne^{8+}+X^+$ n-resolved cross sections.

(a) X=H (triplets); (b) X=H (singlets); (c) X=H (sums of singlets and triplets), and experimental data (Bendahman et al. 1985; Meyer et al. 1985); (d) X=He, and comparison to experimental result of Greenwood et al. (2001).

$3.4.1 \text{ NE}^{9+} + \text{H}$

For Ne⁹⁺+H, the singlet and triplet cross sections are calculated separately due to symmetry considerations. Figure 3.11 (a) shows the n-resolved triplet cross sections, where the dominant capture channel is n=5 (for energies below ~ 854 eV/u), and n=4 for energies above that value. In (b), the n-resolved singlet cross sections are similar. Graph (c) shows the total n-resolved cross sections, which are the sums of each n state in the singlets and triplets, and they are compared to experimental total cross section data from Bendahman et al. (1985) and Meyer et al. (1985). The MCLZ cross section is in close agreement with results of both Bendahman et al. (1985) and Meyer et al. (1985). Dominant channels are listed in Table 3.3.

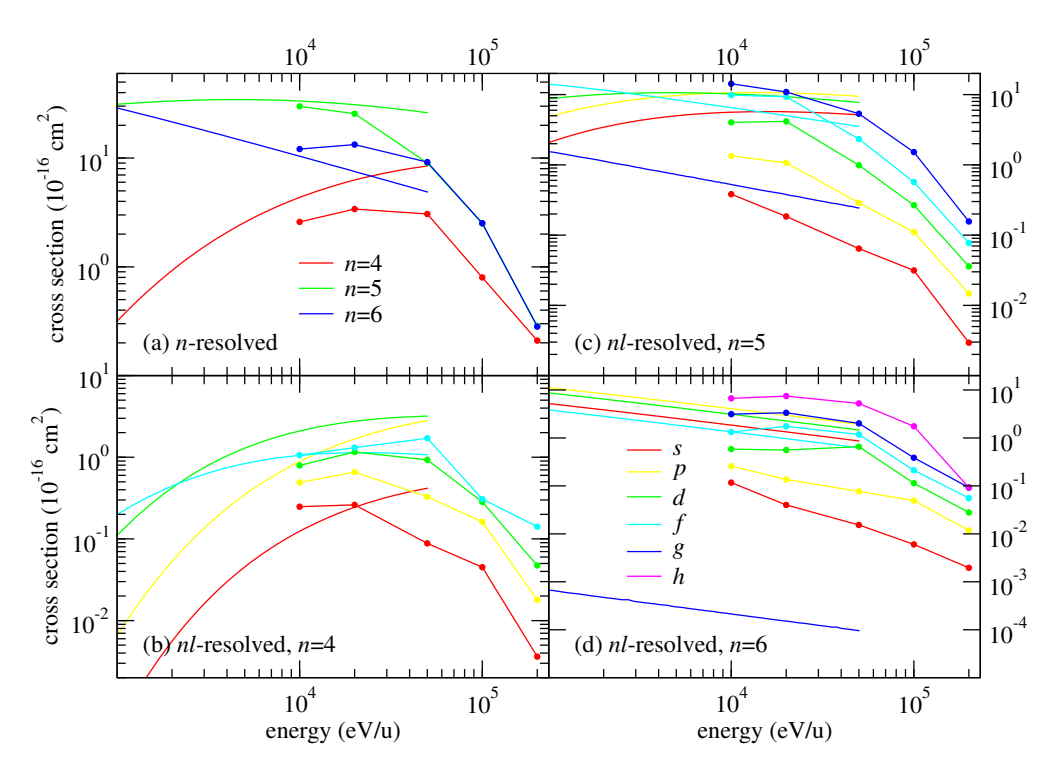


Figure 3.12: $Ne^{9+}+H\rightarrow Ne^{8+}+H^+$ n- and $n\ell$ -resolved cross section comparisons.

MCLZ (lines); CTMC (Schultz and Kristić 1996) (lines with circles). Note that ℓ -distribution functions are not needed for two or more electron ions for MCLZ calculations.

Figure 3.12 displays a comparison of MCLZ $n\ell$ -resolved cross sections for Ne⁹⁺+H with CTMC data (Schultz and Kristić 1996). The data are in good agreement with each other at 10 keV/u for the n-resolved cross sections, but they diverge at higher energies as would be expected. Further, the CTMC calculations adopt an effective one-electron model and cannot distinguish final singlet or triplet ions. As a consequence, CTMC results generally follow a statistical ℓ -distribution pattern. On the other hand, each $n\ell S$ -cross section is explicitly calculated, without a distribution function, with the MCLZ method. Further, for He-like ions, the degeneracy in an n-manifold is lifted, but the energy of the states may be in a counter-intuitive order. As an example, the 4 3L ordering is S, P, F, and D, which partially explains the same ordering in the MCLZ cross sections about \sim 2 keV/u in Figure 3.12(b).

$3.4.2 \ NE^{9+} + HE$

Figure 3.11 (d) shows the single electron capture n-resolved cross sections for Ne⁹⁺+He, with comparison to the single measurement of Greenwood et al. (2001). The latter is also in excellent agreement with the MCLZ results.

3.5 NE^{8+}

Total MCLZ SEC cross sections for $Ne^{8+}+H$ and $Ne^{8+}+He$ are presented in Figure 3.13.

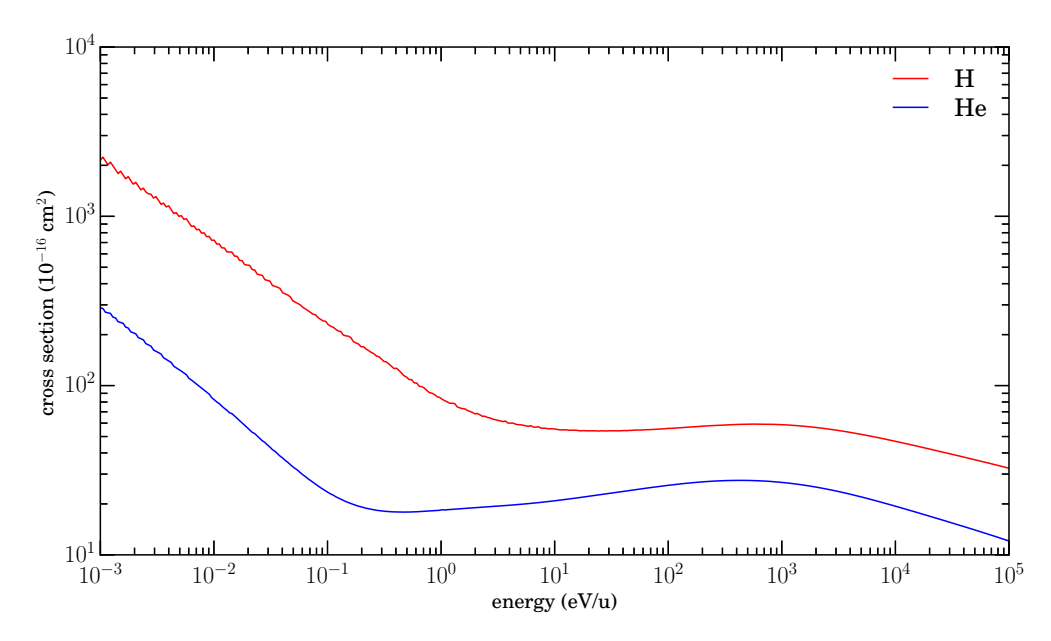


Figure 3.13: $Ne^{8+}+X\rightarrow Ne^{7+}+X^+$ total cross sections.

Additional details for Ne⁸⁺+X, where X=H, are given in Section 3.5.1; and for X=He, Section 3.5.2.

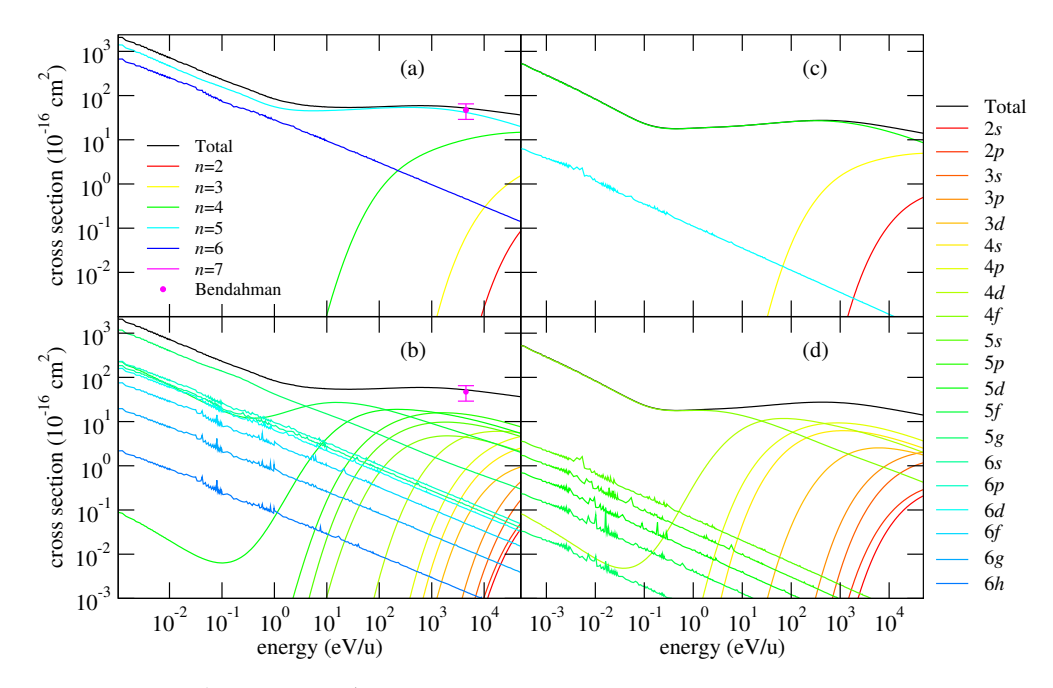


Figure 3.14: $Ne^{8+}+X\rightarrow Ne^{7+}+X^+$ n- and $n\ell$ -resolved cross section comparisons.

(a) X=H (n-resolved), and experimental data of Bendahman et al. (1985); (b) X=H ($n\ell$ -resolved), and experimental data of Bendahman et al. (1985); (c) X=He (n-resolved); (d) X=He ($n\ell$ -resolved).

$3.5.1 \text{ NE}^{8+} + \text{H}$

 $Ne^{8+}+H$ cross sections, n- and $n\ell$ -resolved, are presented in Figure 3.14(a) and (b). For comparison purposes, there is also an experimental data point from Bendahman et al. (1985), which agrees with the MCLZ total cross section at 4500 eV/u.

Figure 3.15 shows a comparison of MCLZ n- and $n\ell$ -resolved cross sections with CTMC data (Schultz and Kristić 1996). At 10 keV/u, n=4 and n=5 closely agree with the CTMC results from Schultz and Kristić (1996). For the $n\ell$ -resolved cross sections in (b), the agreement at 10 keV/u is very good since the effective one-electron CTMC model should be valid for the Li-like Ne product ions. However, as for Ne⁹⁺ collisions, the CTMC ℓ -distributions are statistical, while MCLZ ℓ -cross section orders are controlled mostly by the energy ordering of states.

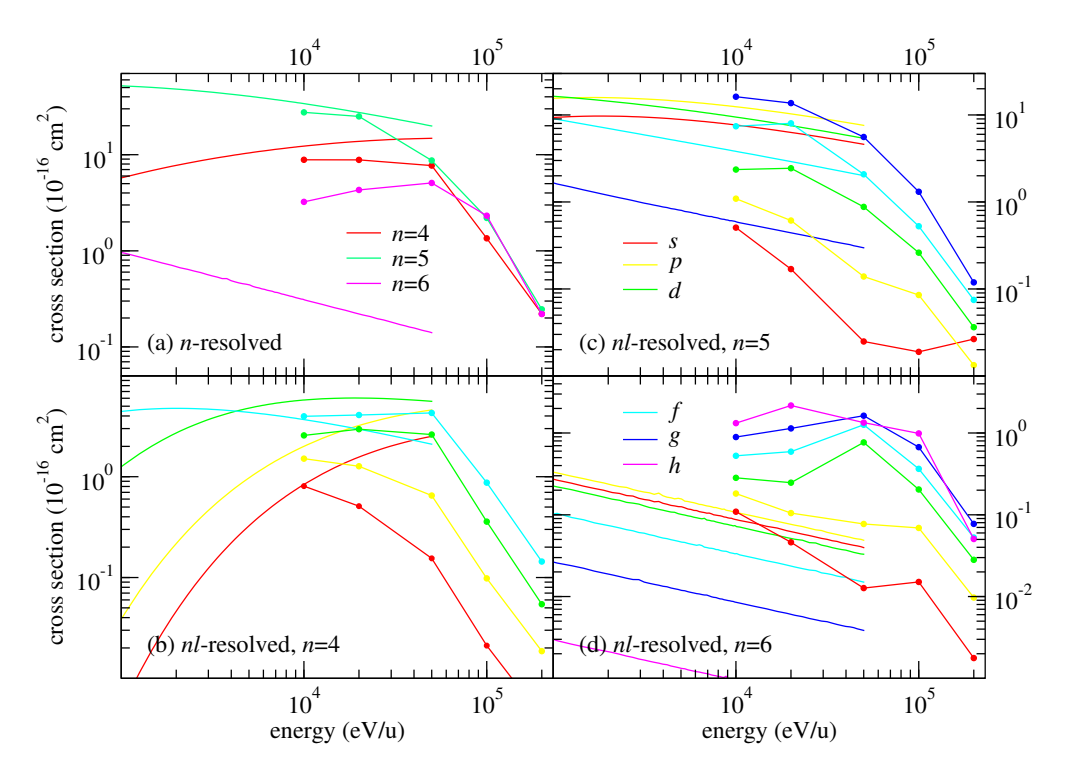


Figure 3.15: Ne⁸⁺+H \rightarrow Ne⁷⁺+H⁺ n- and $n\ell$ -resolved cross section comparisons.

 MCLZ (lines); CTMC (Schultz and Kristić 1996) (lines with circles).

$3.5.2 \text{ NE}^{8+} + \text{He}$

 Ne^{8+} +He cross sections, n- and $n\ell$ -resolved, are presented in Figure 3.14(c) and (d). Dominant channels are listed in Table 3.3. There are no other data available for the purpose of comparison.

$3.6 \, \text{Mg}^{12+}$

Total cross sections for ${\rm Mg^{12+}}$ with H and He are shown in Figure 3.16.

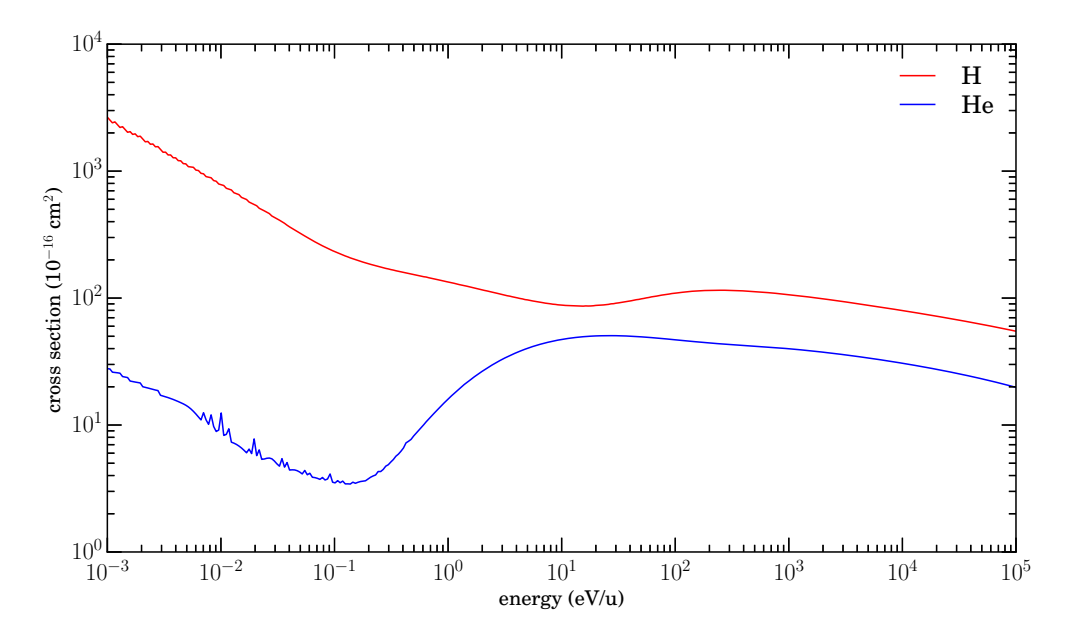


Figure 3.16: $Mg^{12+}+X\rightarrow Mg^{11+}+X^+$ total cross sections.

The $n\ell$ -resolved cross sections are calculated using the statistical (Equation 3.1) and low-energy (Equation 3.2) distribution functions. Plots for these results are shown in the appropriate sections below. Furthermore, previously published results for Mg^{12+} ionic collisions with H and He are not available. The results here can serve as a basis for future comparisons.

Additional details for $Mg^{12+}+X$, where X=H, are given in Section 3.6.1; and for X=He, Section 3.6.2.

$3.6.1 \quad MG^{12+} + H$

Figure 3.17 shows the *n*-resolved cross sections for $Mg^{12+}+H\rightarrow Mg^{11+}+H^+$. The dominant channels, as shown in the figure, are listed in Table 3.4.

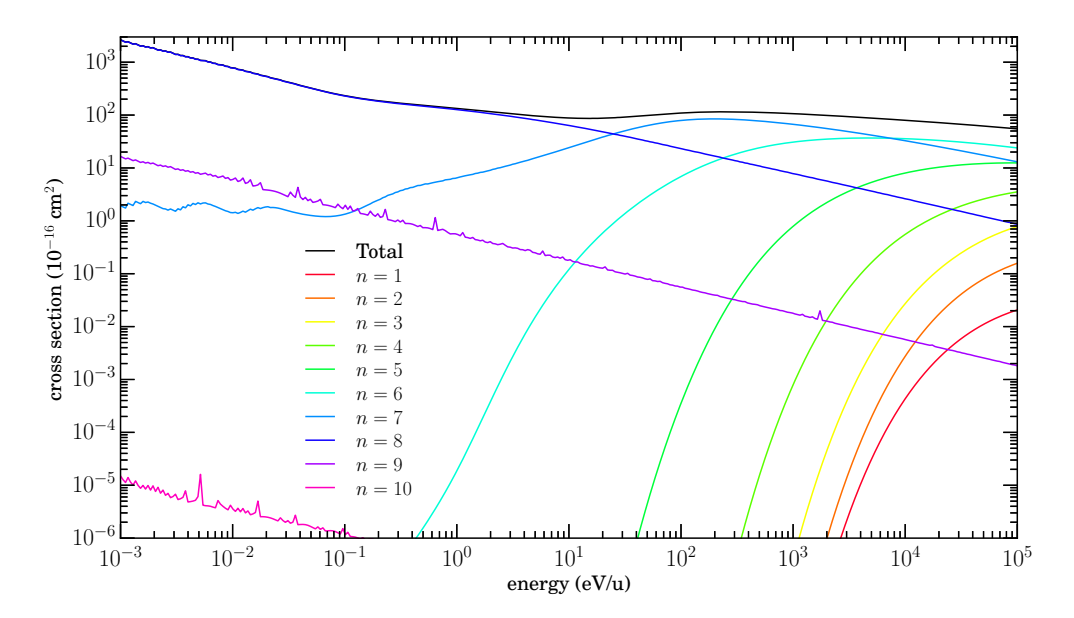


Figure 3.17: $Mg^{12+}+H\rightarrow Mg^{11+}+H^+$ n-resolved cross sections.

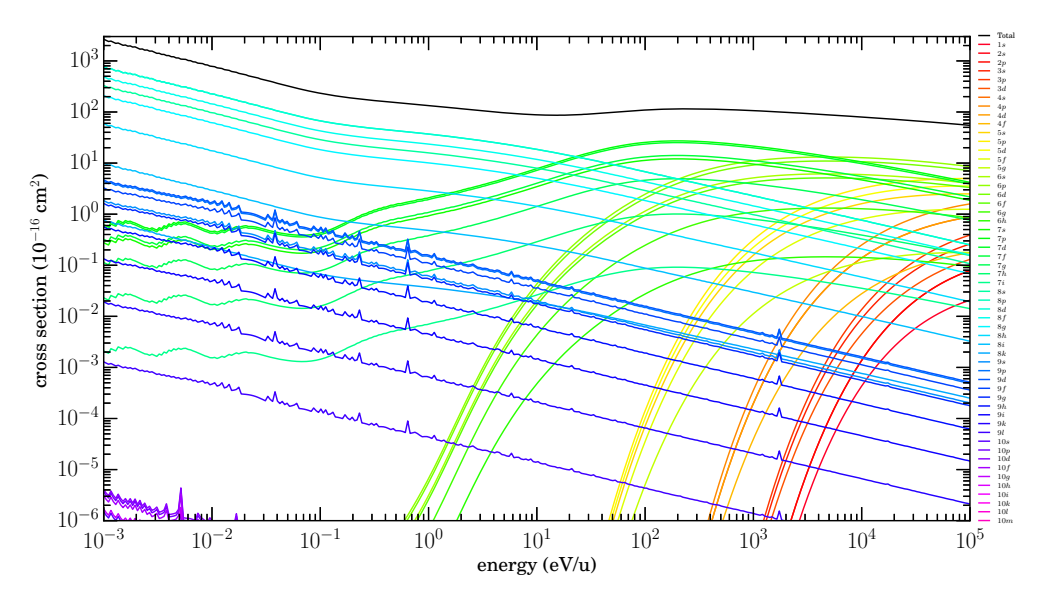


Figure 3.18: $Mg^{12+}+H\rightarrow Mg^{11+}+H^+$ $n\ell$ -resolved cross sections.

Low-energy distribution function.

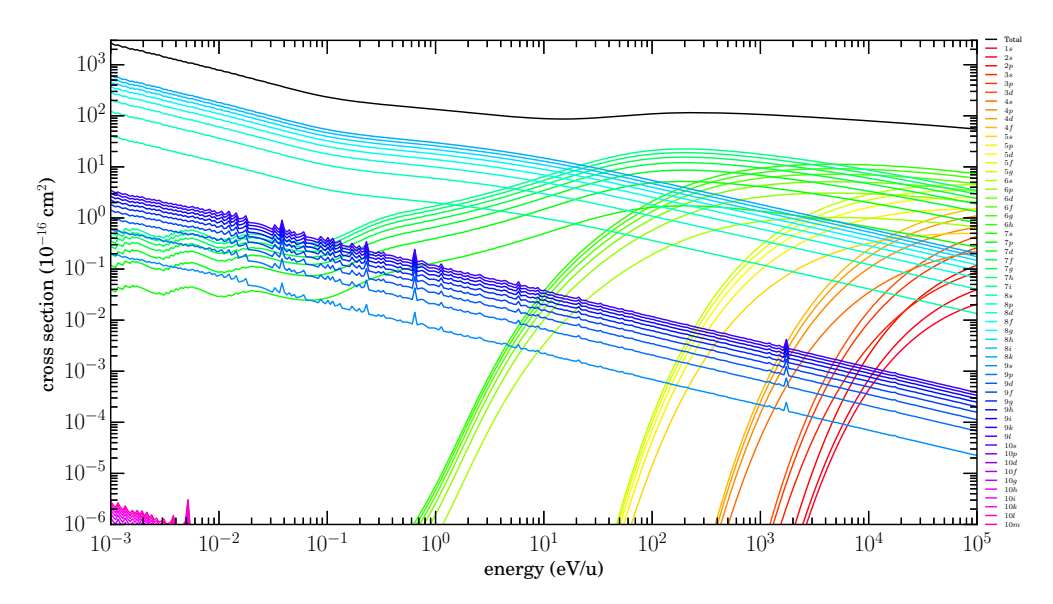


Figure 3.19: Mg^{12+}+H \rightarrow Mg^{11+}+H^+ $n\ell$ -resolved cross sections.

Statistical distribution function.

$3.6.2~{\rm MG^{12+}\!+\!HE}$

Figure 3.20 shows the *n*-resolved cross sections for $Mg^{12+}+He \rightarrow Mg^{11+}+He^+$. The dominant channels, as shown in the figure, are listed in Table 3.4.

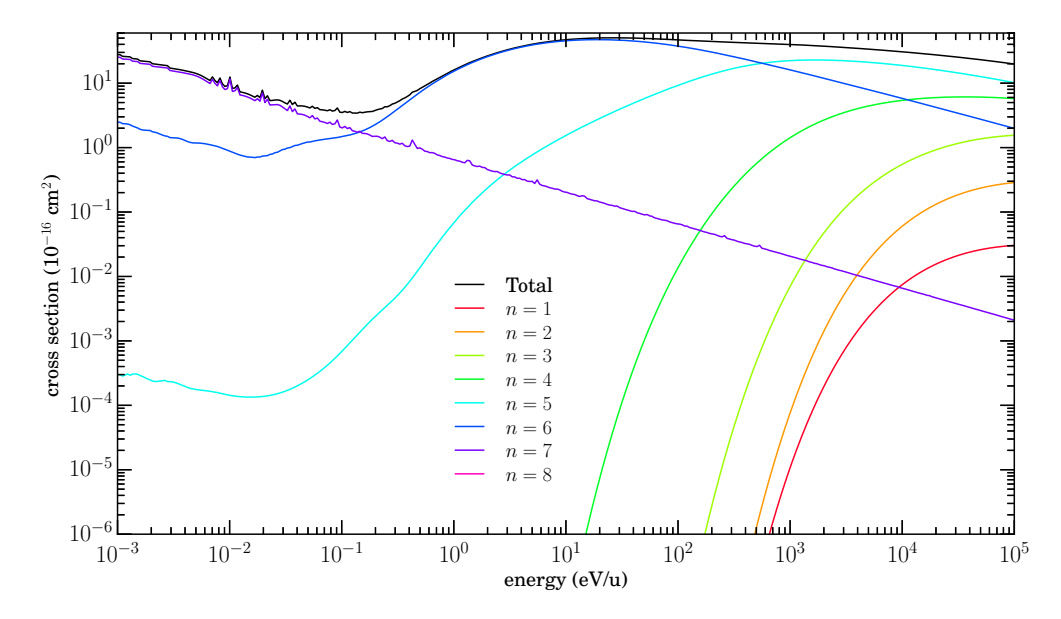


Figure 3.20: Mg^{12+}+He \rightarrow Mg^{11+}+He⁺ n-resolved cross sections.

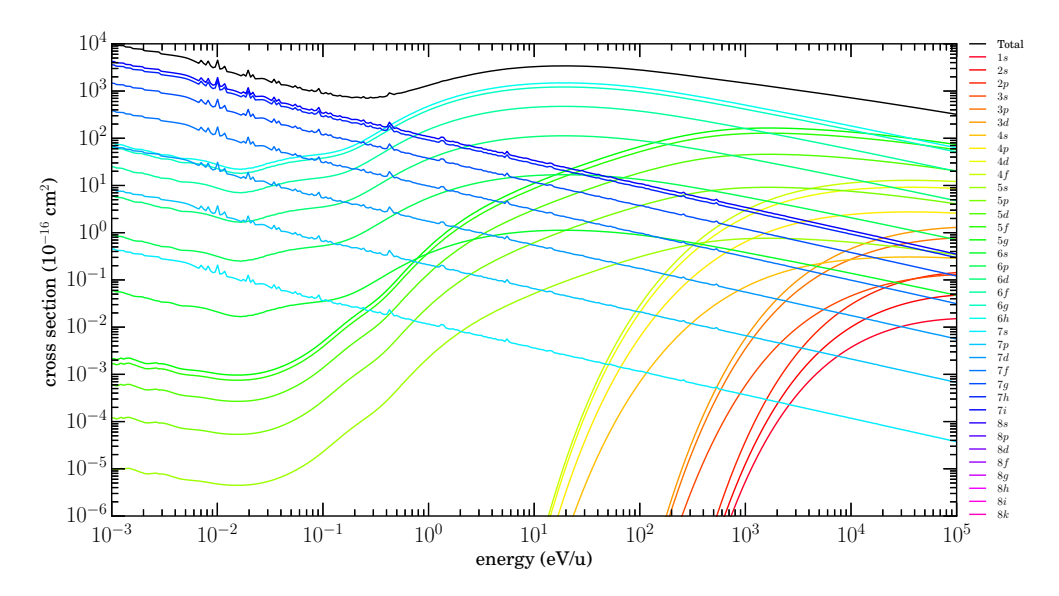
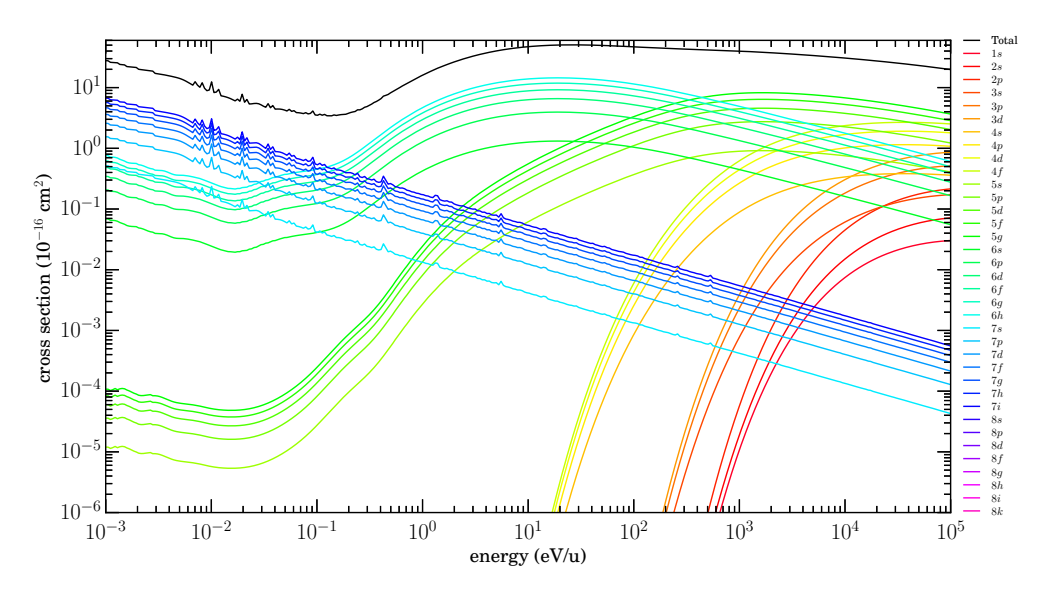


Figure 3.21: $Mg^{12+}+He\rightarrow Mg^{11+}+He^+$ $n\ell$ -resolved cross sections.

Low-energy distribution function.



Statistical distribution function.

$3.7 \, \text{Mg}^{11+}$

Total cross sections for Mg^{11+} with H and He are shown in Figure 3.23. Additional details for $Mg^{11+}+X$, where X=H are given in Section 3.7.1; and for X=He, Section 3.7.2.

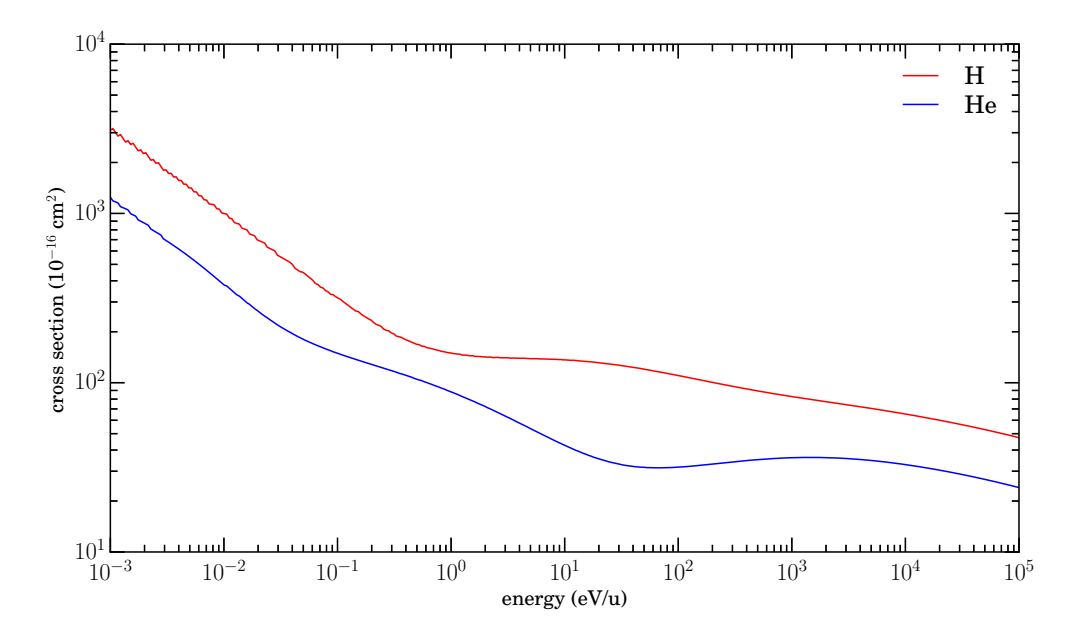


Figure 3.23: $Mg^{11+}+X\rightarrow Mg^{10+}+X^+$ total cross sections.

$3.7.1 \quad MG^{11+} + H$

Cross sections for singlets (Figure 3.24) and triplets (Figure 3.25) are calculated separately for $Mg^{11+}+H\rightarrow Mg^{10+}+H^+$. The total n-resolved cross sections, which are the sums of the singlets and triplets, are shown in Figure 3.26. Dominant channels are listed in Table 3.4. There are no other known available data for this collision system.

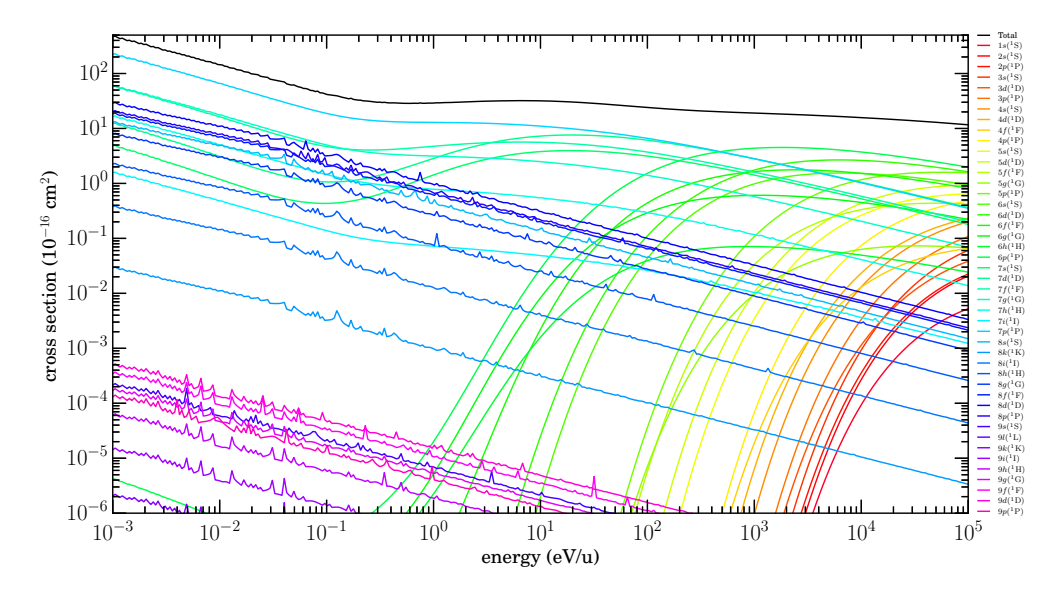


Figure 3.24: Mg^11++H \rightarrow Mg^10++H+ $n\ell$ -resolved cross sections. Singlets.

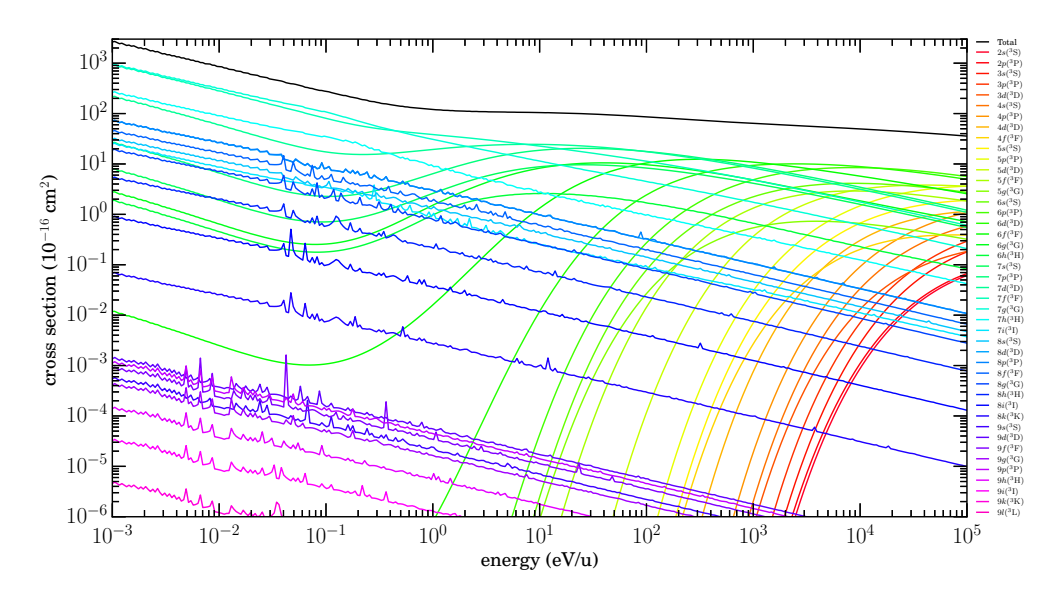


Figure 3.25: Mg^11++H →Mg^10++H+ $n\ell$ -resolved cross sections. Triplets.

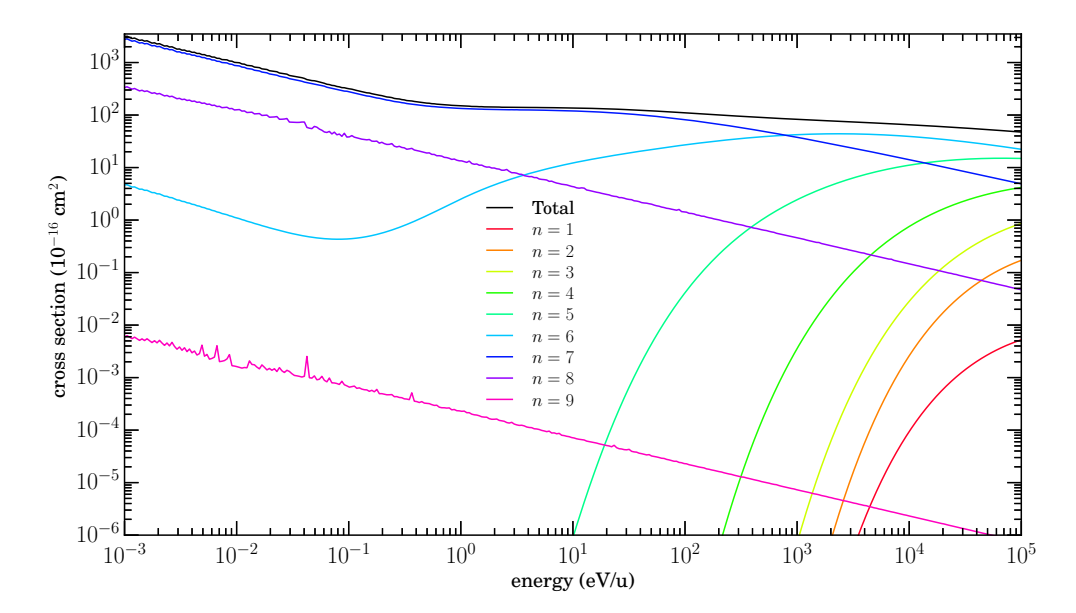


Figure 3.26: $Mg^{11+}+H\rightarrow Mg^{10+}+H^+$ n-resolved cross sections.

Sums of singlets and triplets.

$3.7.2~{\rm Mg^{11+}}{+}{\rm He}$

Cross sections for $Mg^{11+}+He\rightarrow Mg^{10+}+He^+$ are shown in Figures 3.27 ($n\ell$ -resolved) and 3.28 (n-resolved). Dominant channels are listed in Table 3.4. Again, with this system, no previously published results are available.

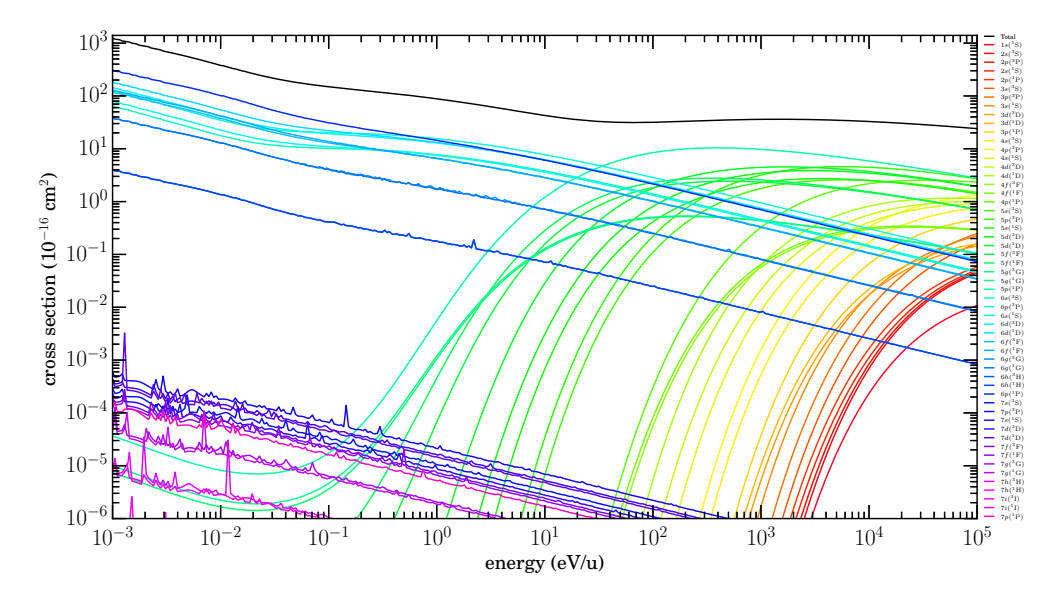


Figure 3.27: $Mg^{11+}+He\rightarrow Mg^{10+}+He^+$ $n\ell$ -resolved cross sections.

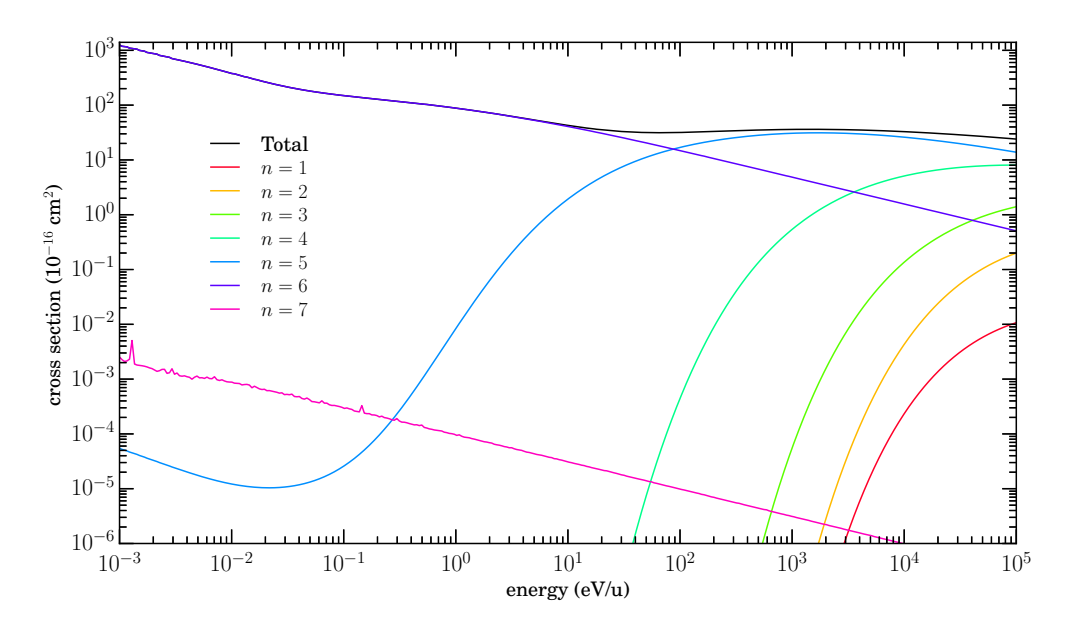


Figure 3.28: $Mg^{11+}+He\rightarrow Mg^{10+}+He^+$ n-resolved cross sections.

$3.8 \, \text{Mg}^{10+}$

Total cross sections for Mg^{10+} with H and He are shown in Figure 3.29. Additional details for $Mg^{10+}+X$, where X=H are given in Section 3.8.1; and for X=He, Section 3.8.2.

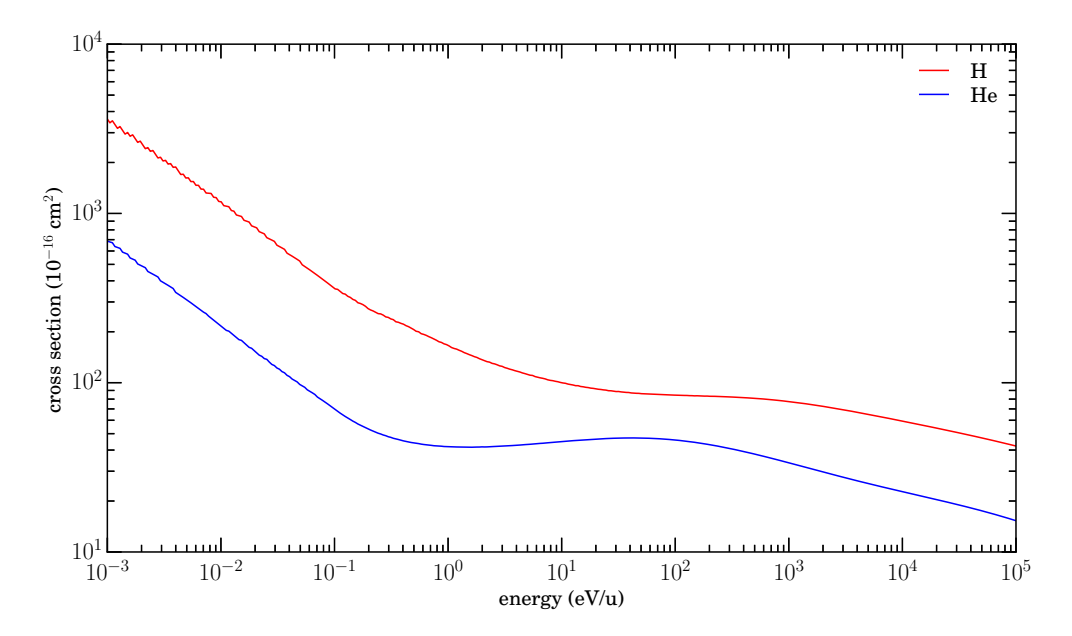


Figure 3.29: ${\rm Mg^{10+}}{+}X{\rightarrow}{\rm Mg^{9+}}{+}X^+$ total cross sections.

$3.8.1 \quad MG^{10+} + H$

Figure 3.30 shows $n\ell$ -resolved cross sections for $Mg^{10+}+H\to Mg^{9+}+H^+$, and Figure 3.31 shows n-resolved cross sections for this system. There are no other known available data for comparison. The dominant channels are listed in Table 3.4.

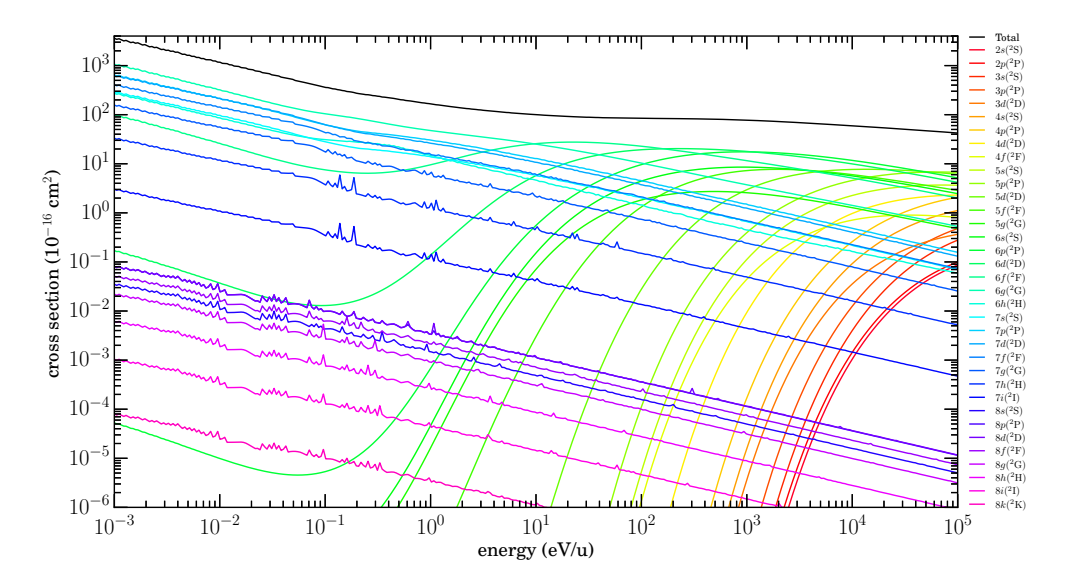


Figure 3.30: Mg^{10+}+H \rightarrow Mg^{9+}+H^+ $n\ell$ -resolved cross sections.

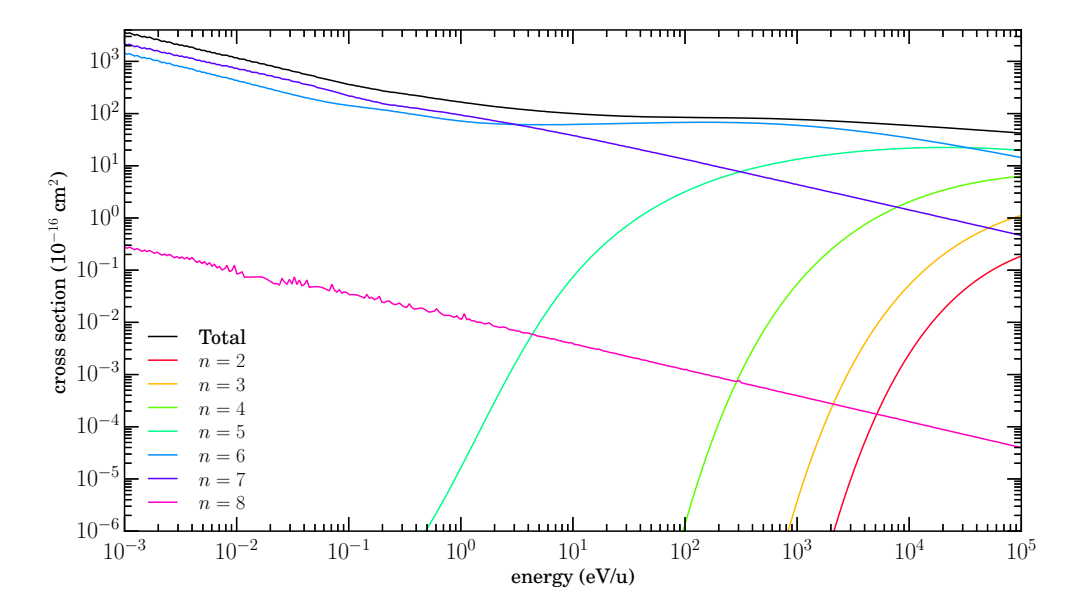


Figure 3.31: $Mg^{10+}+H\rightarrow Mg^{9+}+H^+$ n-resolved cross sections.

$3.8.2~{\rm MG^{10+} + HE}$

Figure 3.32 shows $n\ell$ -resolved cross sections for $Mg^{10+}+He\to Mg^{9+}+He^+$, and Figure 3.33 shows n-resolved cross sections for this system. There are no other known available data for comparison. The dominant channels are listed in Table 3.4.

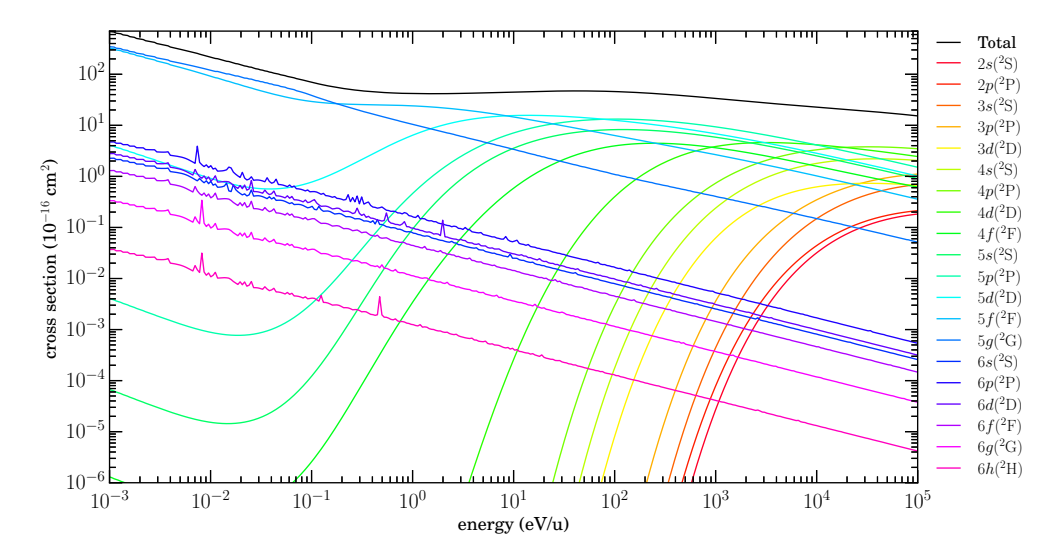


Figure 3.32: $Mg^{10+}+He \rightarrow Mg^{9+}+He^+$ $n\ell$ -resolved cross sections.

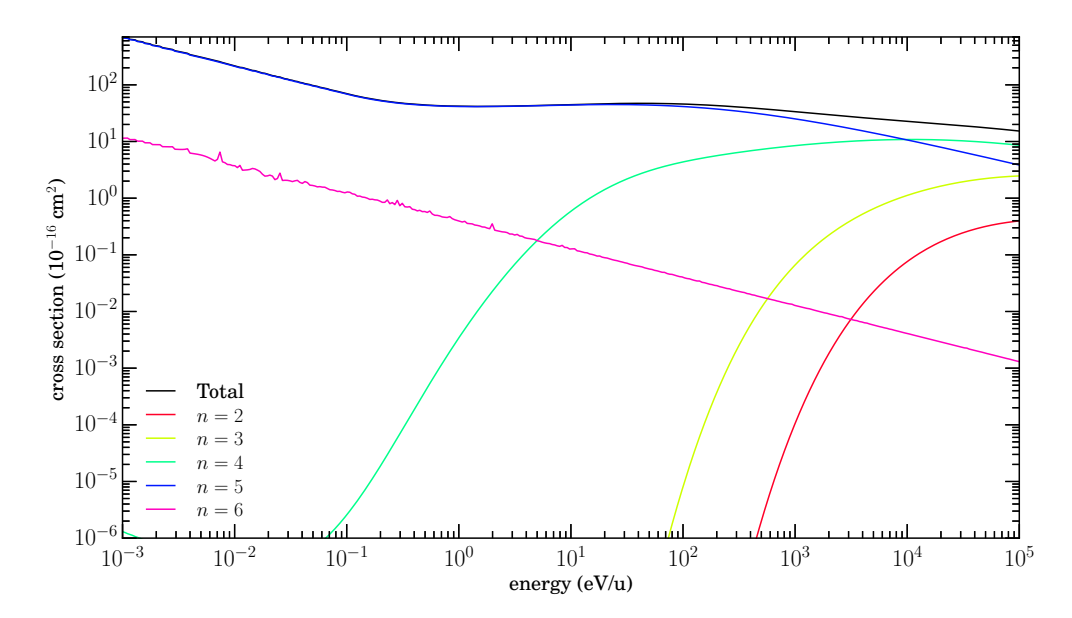


Figure 3.33: $Mg^{10+}+He\rightarrow Mg^{9+}+He^+$ n-resolved cross sections.

$3.9 \, \text{Mg}^{9+}$

Total cross sections for Mg^{9+} with H and He are shown in Figure 3.34. Additional details for $Mg^{9+}+X$, where X=H are given in Section 3.9.1; and for X=He, Section 3.9.2.

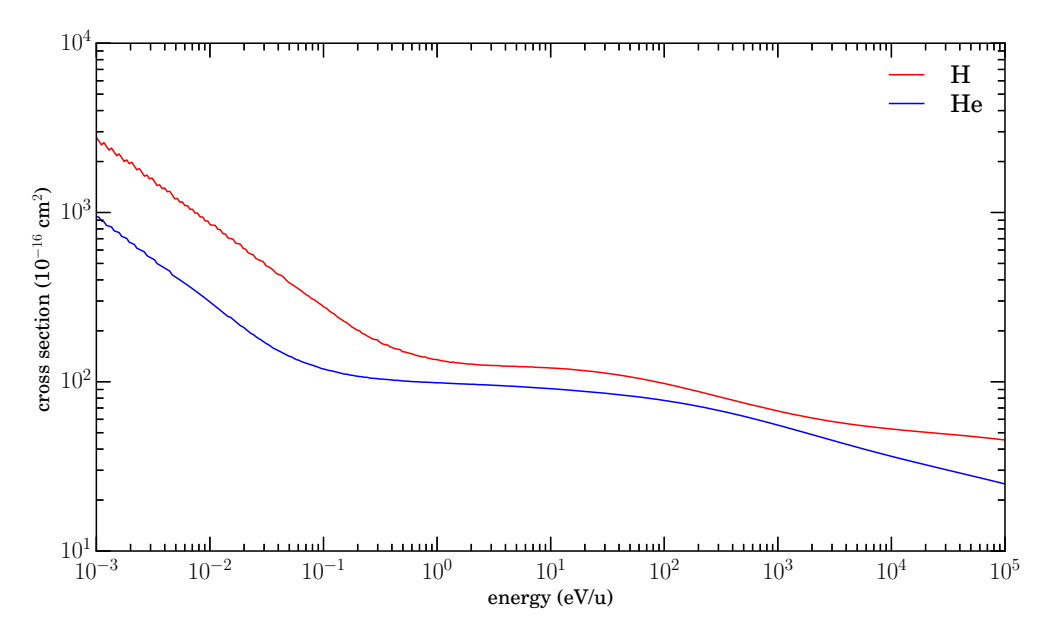


Figure 3.34: $Mg^{9+}+X\rightarrow Mg^{8+}+X^+$ total cross sections.

$3.9.1 \quad MG^{9+} + H$

Singlets and triplets are calculated separately for $Mg^{9+}+H\rightarrow Mg^{8+}+H^+$, and the results are shown in Figures 3.35 (singlets) and 3.36 (triplets). The *n*-resolved cross sections are the sums of the singlet and triplet cross sections, and they are shown in Figure 3.37. There are no other known available data for comparison.

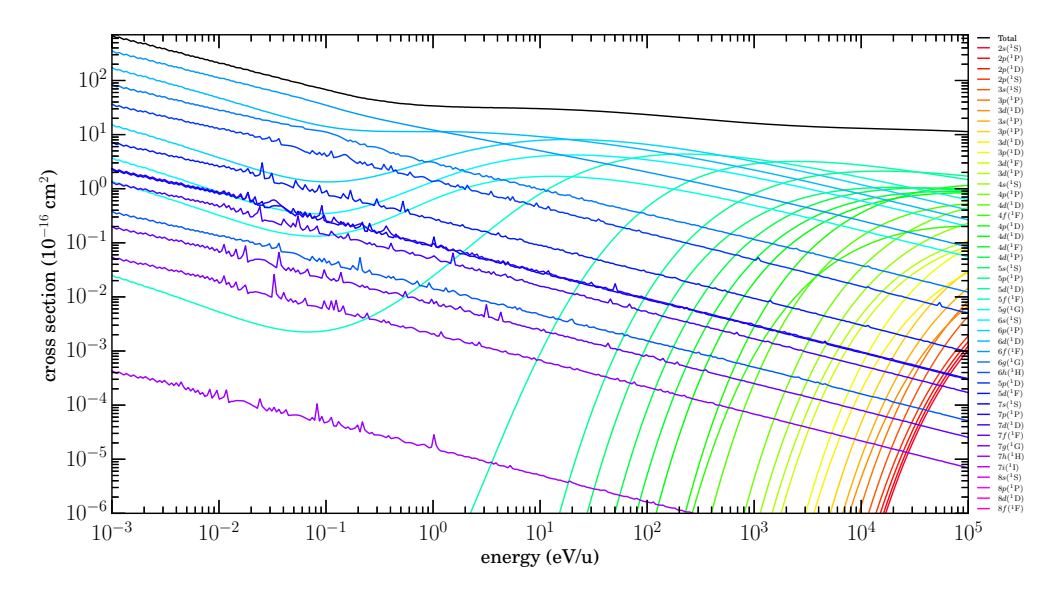


Figure 3.35: ${\rm Mg}^{9+}{+}{\rm H}{\to}{\rm Mg}^{8+}{+}{\rm H}^{+}$ $n\ell$ -resolved cross sections. Singlets.

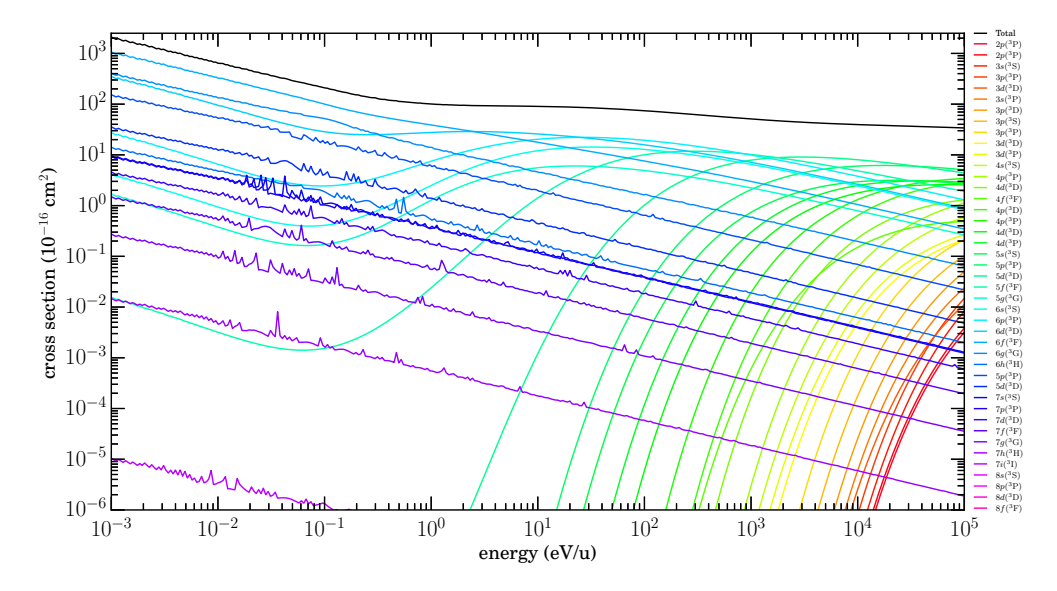


Figure 3.36: Mg⁹⁺+H \rightarrow Mg⁸⁺+H⁺ $n\ell$ -resolved cross sections. Triplets.

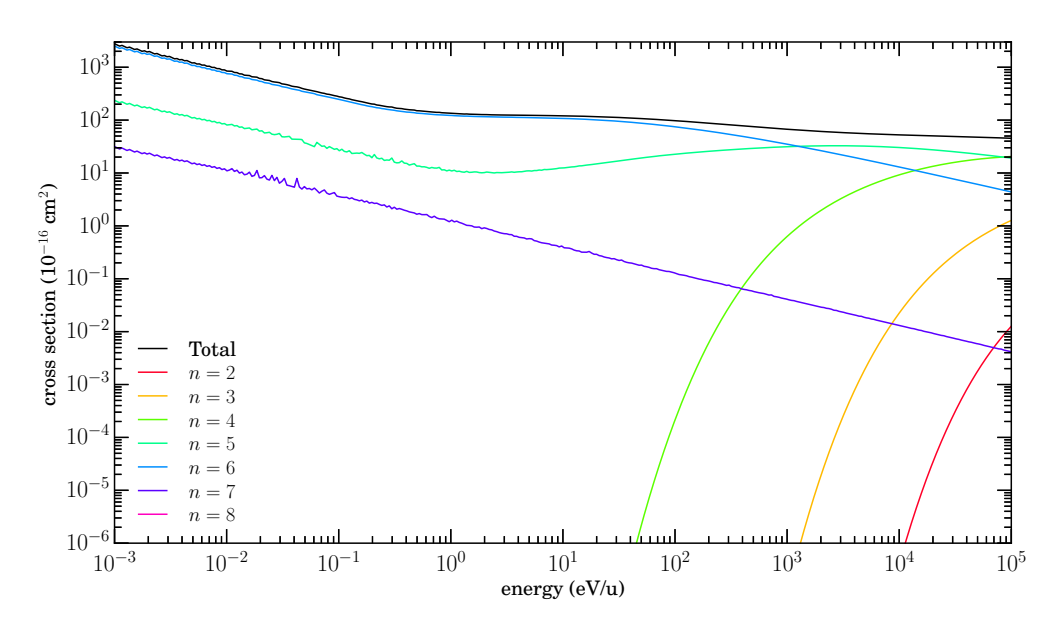


Figure 3.37: Mg^9++H \rightarrow Mg⁸⁺+H⁺ n-resolved cross sections.

Sums of singlets and triplets.

$3.9.2~{\rm Mg^{9+}}{+}{\rm HE}$

Figure 3.38 shows $n\ell$ -resolved cross sections for $Mg^{9+}+He \rightarrow Mg^{8+}+He^+$, and Figure 3.39 shows n-resolved cross sections for this system. There are no other known available data for comparison. The dominant channels are listed in Table 3.4.

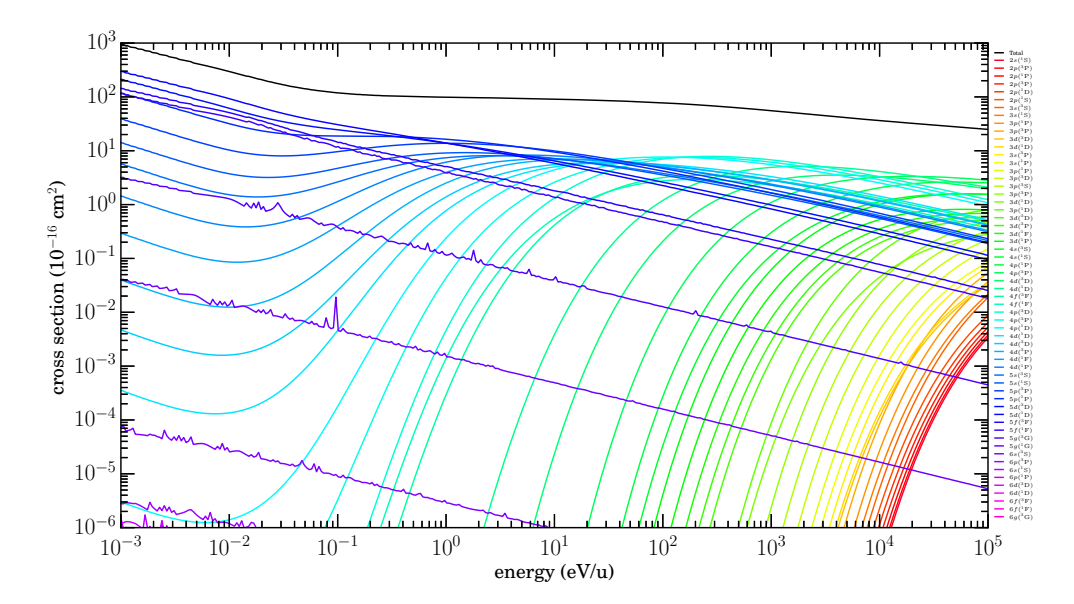


Figure 3.38: ${\rm Mg^{9+}}{+}{\rm He}{\rightarrow}{\rm Mg^{8+}}{+}{\rm He^{+}}$ $n\ell$ -resolved cross sections.

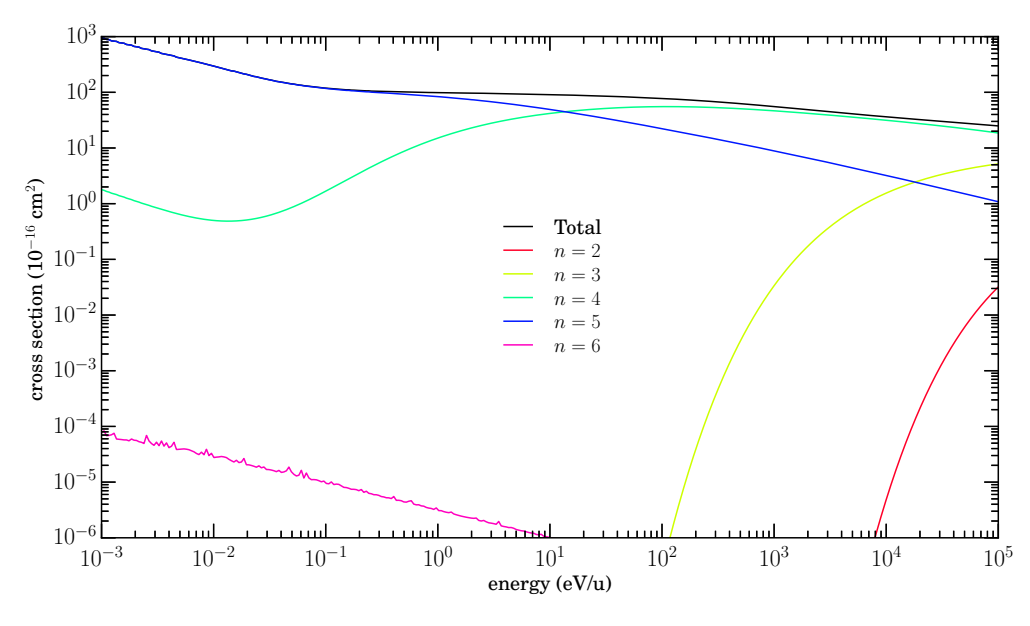


Figure 3.39: ${\rm Mg}^{9+}{\rm +He}{\rightarrow}{\rm Mg}^{8+}{\rm +He}^+$ $n{\rm -resolved}$ cross sections.

3.10 Mg^{8+}

Total cross sections for Mg^{8+} with H and He are shown in Figure 3.40. Additional details for $Mg^{8+}+X$, where X=H are given in Section 3.10.1; and X=He, Section 3.10.2.

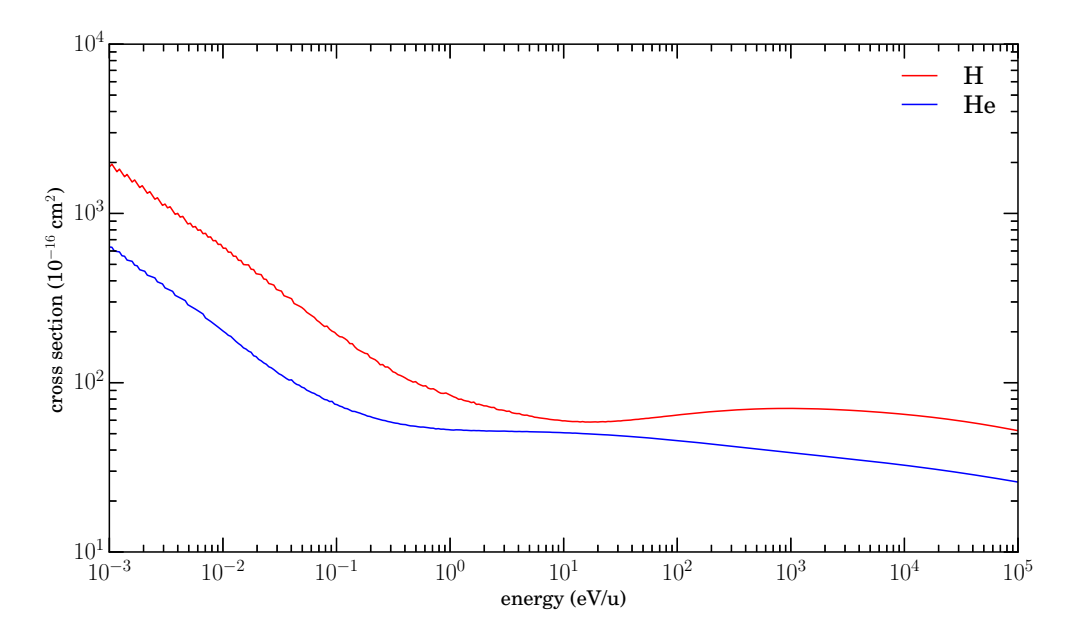


Figure 3.40: ${\rm Mg^{8+}}{+}X{\rightarrow}{\rm Mg^{7+}}{+}X^{+}$ total cross sections.

$3.10.1 \, \mathrm{Mg^{8+}} + \mathrm{H}$

Figure 3.41 shows $n\ell$ -resolved cross sections for Mg⁸⁺+H \rightarrow Mg⁷⁺+H⁺, and Figure 3.42 shows n-resolved cross sections for this system. There are no other known available data for comparison. The dominant channels are listed in Table 3.4.

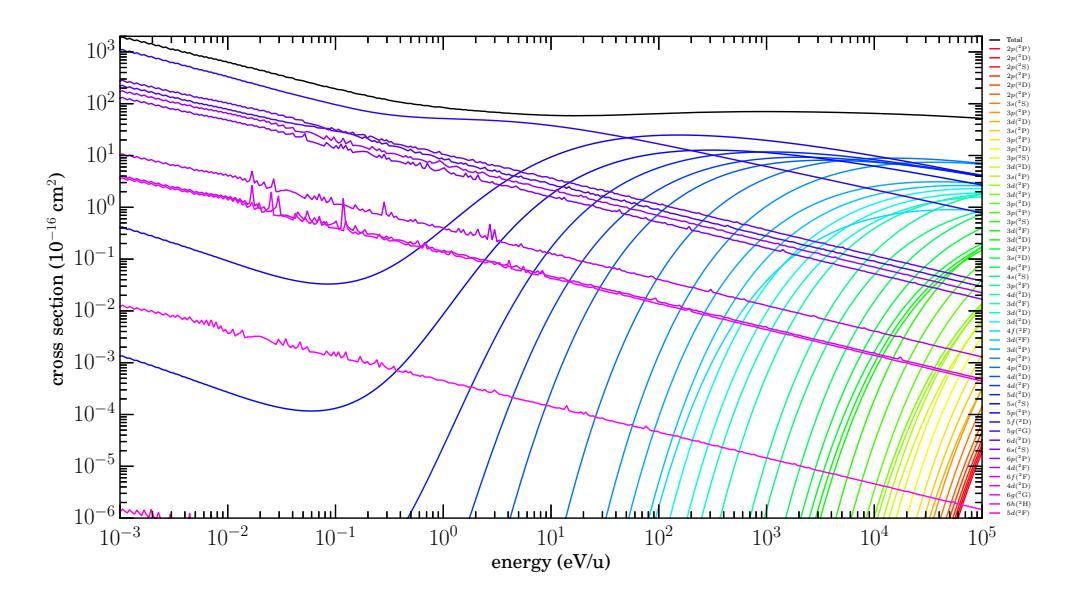


Figure 3.41: $Mg^{8+}+H\rightarrow Mg^{7+}+H^+$ $n\ell$ -resolved cross sections.

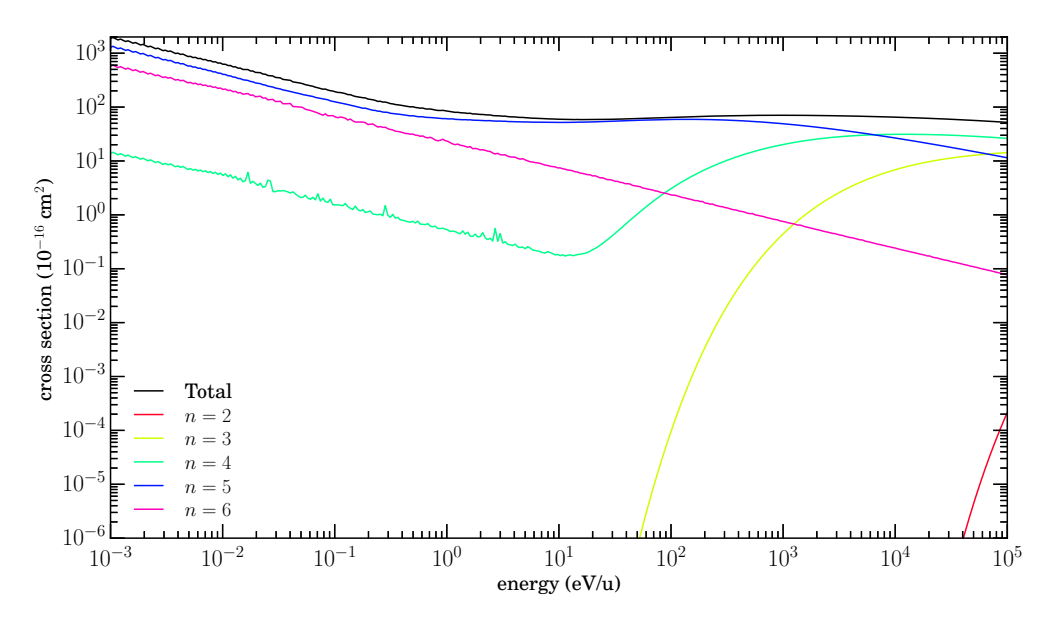


Figure 3.42: $Mg^{8+}+H\rightarrow Mg^{7+}+H^+$ n-resolved cross sections.

$3.10.2~{\rm Mg^{8+}}{+}{\rm HE}$

Figure 3.43 shows $n\ell$ -resolved cross sections for $Mg^{8+}+He \rightarrow Mg^{7+}+He^{+}$, and Figure 3.44 shows n-resolved cross sections for this system. There are no other known available data for comparison. The dominant channels are listed in Table 3.4.

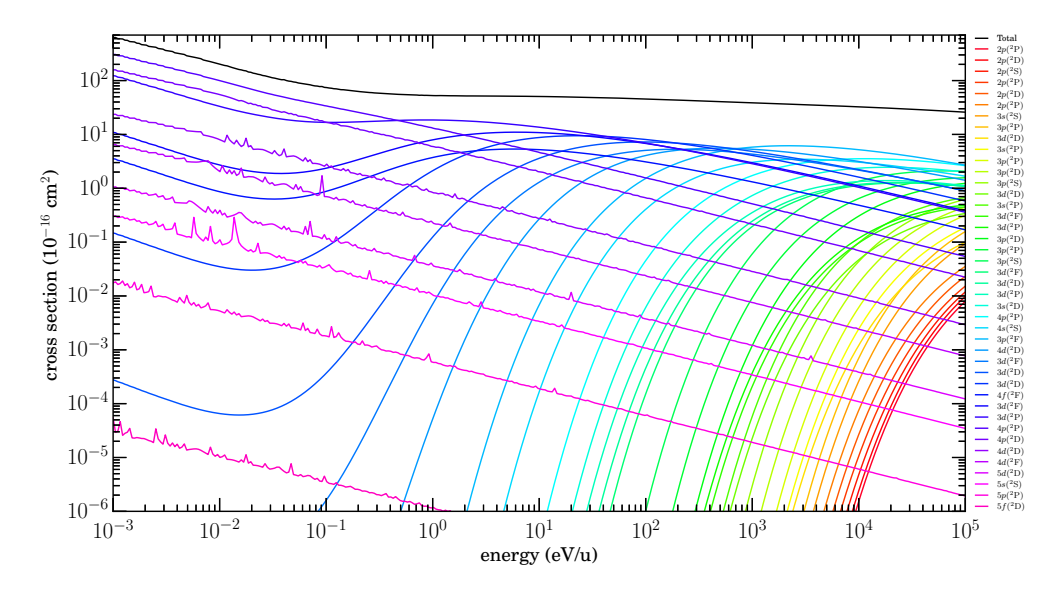


Figure 3.43: Mg⁸⁺+He \rightarrow Mg⁷⁺+He⁺ $n\ell$ -resolved cross sections.

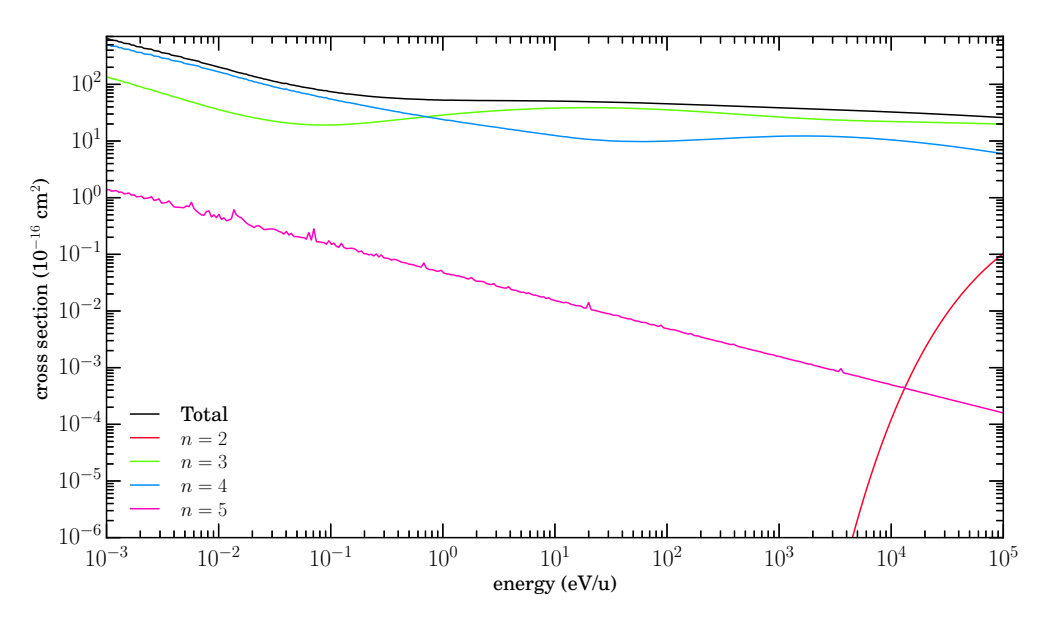


Figure 3.44: ${\rm Mg^{8+} + He \rightarrow Mg^{7+} + He^{+}}$ n-resolved cross sections.

3.11 Summary

Using the MCLZ method, SEC cross sections were calculated and plotted for $Ne^{q+}+X$, where q=8-10, and for $Mg^{q+}+X$, where q=8-12, and X=H and He. These results were compared to previous theoretical and experiemental results where available. It was determined that the

Table 3.3. $Ne^{(8-10)+}$ Dominant Channels.

System	Channel	eV/u
$Ne^{10+} + H \rightarrow Ne^{9+} + H^{+}$	n=7	$\lesssim 2.3 \mathrm{e}1$
	n=6	2.3e1 - 2.1e4
	$n{=}5$	$\gtrsim 2.1e4$
$Ne^{10+} + He \rightarrow Ne^{9+} + He^{+}$	n=6	\lesssim 6.3e-1
	$n{=}5$	6.3e-1-5.1e3
	$n{=}4$	\gtrsim 5.1e3
$Ne^{9+} + H \rightarrow Ne^{8+} + H^{+}$	n=6	$\lesssim 9.8e2$
	$n{=}5$	$\gtrsim 9.8e2$
$Ne^{9+}+He\rightarrow Ne^{8+}+He^{+}$	$n{=}5$	$\lesssim 2.0e2$
	$n{=}4$	$\gtrsim 2.0e2$
$Ne^{8+}+H\to Ne^{7+}+H^{+}$	$n{=}5$	1.0e-3-1.0e5
$Ne^{8+}+He\rightarrow Ne^{7+}+He^{+}$	n=4	1.0e-3-1.0e5

results in this study were consistent with the compared data, and thus, the MCLZ method is a reasonably accurate estimation of SEC cross sections.

Because of the lack of available data for comparison with the Mg systems, it can only be said that the results appeared to be consistent. It was assumed the same accuracy was present in these systems as in the Ne systems, which were shown to agree with other sources of data.

Presented are Tables 3.3 and 3.4, which show the dominant channels which were found in each system.

Table 3.4. $Mg^{(8-12)+}$ Dominant Channels.

System	Channel	$\mathrm{eV/u}$
M ₀ 12+ + II - M ₀ 11+ + II+	Q	<0 to1
$Mg^{12+} + H \rightarrow Mg^{11+} + H^{+}$	$n=8 \\ n=7$	$\lesssim 2.5e1$ 2.5e1-7.4e3
	n=1 $n=6$	2.5e1-7.4e3 \ge 7.4e3
$\mathrm{Mg^{12+}}\mathrm{+He}\mathrm{\to}\mathrm{Mg^{11+}}\mathrm{+He^{+}}$	n=0 $n=7$	$\lesssim 1.5 \text{e-}1$
Mg He /Mg He	n=6	1.5e-1–5.6e2
	n=5	$\gtrsim 5.6e2$
${\rm Mg^{11+}}{+}{\rm H}{ ightarrow}{\rm Mg^{10+}}{+}{\rm H^{+}}$	n=7	$\stackrel{\sim}{\lesssim} 7.9 \mathrm{e}2$
1120 1110	n=6	$\gtrsim 7.9e2$
$Mg^{11+} + He \rightarrow Mg^{10+} + He^{+}$	n=6	$\lesssim 8.7e1$
	n=5	$\gtrsim 8.7 \mathrm{e}1$
${ m Mg^{10+}\!+\!H\!\! o\!\!Mg^{9+}\!+\!H^{+}}$	n=7	$\lesssim 3.1e0$
	n=6	3.1e0 - 3.3e4
	n=5	$\gtrsim 3.3e4$
$\mathrm{Mg^{10+}\!+\!He}{ ightarrow}\mathrm{Mg^{9+}\!+\!He^{+}}$	n=5	$\lesssim 9.6e3$
	$n{=}4$	$\gtrsim 9.6e3$
${\rm Mg^{9+}}{+}{\rm H}{ ightarrow}{\rm Mg^{8+}}{+}{\rm H^{+}}$	n=6	$\lesssim 1.3e3$
	n=5	1.3e3 - 8.4e4
	$n{=}4$	$\gtrsim 8.4 e4$
$\mathrm{Mg^{9+}\!+\!He}{ ightarrow}\mathrm{Mg^{8+}\!+\!He^{+}}$	n=5	$\lesssim 1.4e1$
	n=4	$\gtrsim 1.4e1$
$\mathrm{Mg^{8+}}\mathrm{+H}\mathrm{\to}\mathrm{Mg^{7+}}\mathrm{+H^{+}}$	n=5	\lesssim 6.5e3
25 21 77 25 71 1	n=4	$\gtrsim 6.5 e3$
$Mg^{8+}+He\rightarrow Mg^{7+}+He^{+}$	n=4	$\lesssim 7.1 \text{e-}1$
	n=3	≳7.1e-1

Chapter 4

 $\mathrm{Fe^{(8-9)+}}$ with H, H₂, He, H₂O, CO, CO₂, and N₂ using MCLZ¹

4.1 Introduction

The calculation of cross sections for collisions of $Fe^{(8-9)+}$ with H, H₂, He, H₂O, CO, CO₂, and N₂, resulting in single electron capture, using the Landau-Zener method (Butler and Dalgarno 1980; Janev et al. 1983) is the same as that discussed in Chapter 3 (Lyons et al. 2017). However, since atomic energies for the Rydberg levels (given by the electron configurations) of the resulting ion are required to begin the calculations, an additional step is necessary to obtain those energies when they are unavailable. For example, Table 4.1 shows the energy levels which are available on the NIST Atomic Spectra Database (Kramida et al. 2018).

Of particular concern are the energies of each singly-excited doublet state, i.e., where only the valence electron is excited, as seen in Table 4.2. In these tables, the highly-excited term energies for $3p^64s$, $3p^65s$, $3p^65p$, $3p^65d$, $3p^65g$, etc., are not given. If these energies are unavailable from other sources, they can be calculated or estimated using a variety of methods. These missing energies are estimated using a form of the quantum defect relation (Connerade 1998; Lyons et al. 2017; Mullen et al. 2016):

$$E(n) = E_0 \left(1 - \frac{1}{(n-\mu)^2} \right) \tag{4.1}$$

¹David A. Lyons and Phillip C. Stancil, 2019. To be submitted to *The Astrophysical Journal*.

Table 4.1. Fe VIII ($\mathrm{Fe^{7+}}$) NIST Atomic Energies.

Configuration	Term	J	Level (cm^{-1})	Term Energy (cm ⁻¹)
$3p^63d$	$^{2}\mathrm{D}$	$3/_{2}$	0	0
1		5/2	1836	
$3p^5(^2P^\circ)3d^2(^1G)$	$^2\mathrm{F}^\circ$	5/2	431250	432037
1 () ()		7/2	434555	
$3p^5(^2P^\circ)3d^2(^1D)$	$^2\mathrm{F}^\circ$	7/2	447658	451575
- \		5/2	459367	
$3p^5(^2P^\circ)3d^2(^1S)$	$^2\mathrm{P}^\circ$	3/2	508518	511518
-		1/2	520822	
$3p^{6}4p$	$^2\mathrm{P}^\circ$	1/2	510277	512691
		3/2	515550	
$3p^5(^2P^\circ)3d^2(^3F)$	$^2\mathrm{F}^\circ$	$\frac{5}{2}$	535909	538988
- \		7/2	541755	
$3p^5(^2P^\circ)3d^2(^3P)$	$^2\mathrm{P}^\circ$	1/2	591964	592988
		$^{3/_{2}}$	595152	
$3p^5(^2P^\circ)3d^2(^3F)$	$^2\mathrm{D}^\circ$	$\frac{5}{2}$	596463	595656
		$^{3/_{2}}$	597065	
$3p^{6}4f$	$2F^{\circ}$	$\frac{5}{2}$	763703	762656
		$^{7}/_{2}$	763799	
$3p^{5}3d(^{3}P^{\circ})4s$	$^2\mathrm{P}^\circ$	1/2	837661	840005
		$^{3/_{2}}$	842829	
$3p^{5}3d(^{3}P^{\circ})4s$	$^4\mathrm{F}^\circ$	$^{7/_{2}}$	847145	848229
		$^{5/2}$	849899	
		$^{3/_{2}}$	852849	
$3p^{5}3d(^{3}\mathrm{F}^{\circ})4s$	$^2\mathrm{F}^\circ$	$^{7/_{2}}$	855100	856362
		5/2	860615	
$3p^53d(^3D^\circ)4s$	$^4\mathrm{D}^\circ$	$^{7/_{2}}$	874711	875134

Solving for μ in Equation 4.1 gives

$$\mu = n \pm \sqrt{\frac{1}{1 - \frac{E(n)}{E_0}}} \tag{4.2}$$

Table 4.1 (cont'd)

Configuration	Term	J	Level (cm^{-1})	Term Energy (cm ⁻¹)
		5/2	876765	
		3/2	877476	
		1/2	878264	
$3p^{5}3d(^{1}\mathrm{D}^{\circ})4s$	$^2\mathrm{D}^\circ$	$\frac{5}{2}$	879021	878849
		$^{3/_{2}}$	881345	
$3p^5 3d({}^1{\rm F}^{\circ})4s$	$^2\mathrm{F}^\circ$	$\frac{5}{2}$	884331	884940
		$^{7/_{2}}$	887325	
$3p^{5}3d(^{3}\mathrm{D}^{\circ})4s$	$^2\mathrm{D}^\circ$	$^{3/_{2}}$	889113	889051
		5/2	890845	
$3p^{6}5f$	$^2\mathrm{F}^{\circ}$	5/2	927059	925982
		$^{7/_{2}}$	927102	
$3p^{6}6f$	$^2\mathrm{F}^\circ$	5/2	1016560	1015464
		$^{7/_{2}}$	1016570	
$3p^{6}7f$	$^2\mathrm{F}^\circ$	5/2	1069873	1068861
		$^{7/_{2}}$	1070029	
Fe IX $(3p^6(^1S_0))$	Limit	_	1218380.1	

Equation 4.2 shows that there can be two values for μ , which are called μ_+ and μ_- . Using the term energies in Table 4.2, the values of μ_+ and μ_- are plotted and shown in Figure 4.1, where the linearity of the μ_+ and μ_- values for $\ell=3$ (f states) appear to converge at or near the origin. It is assumed that for all other values of ℓ , the values of μ_+ and μ_- are also linear and converge at the same point. Thus, the values of μ_+ and μ_- are calculated for all n where $\ell=1$, $\ell=2$, and $\ell=3$.

Table 4.2. Fe VIII (Fe⁷⁺) NIST Term Energies: Singly-Excited Doublets.

Configuration	Term	Energy (cm^{-1})
$3p^63d$	$^2\mathrm{D}$	0
$3p^{6}4p$	$^2\mathrm{P}^\circ$	512691
$3p^{6}4f$	$^2\mathrm{F}^\circ$	762656
$3p^{6}5f$	$^2\mathrm{F}^\circ$	925982
$3p^{6}6f$	$^2\mathrm{F}^\circ$	1015464
$3p^67f$	$^2\mathrm{F}^\circ$	1068861

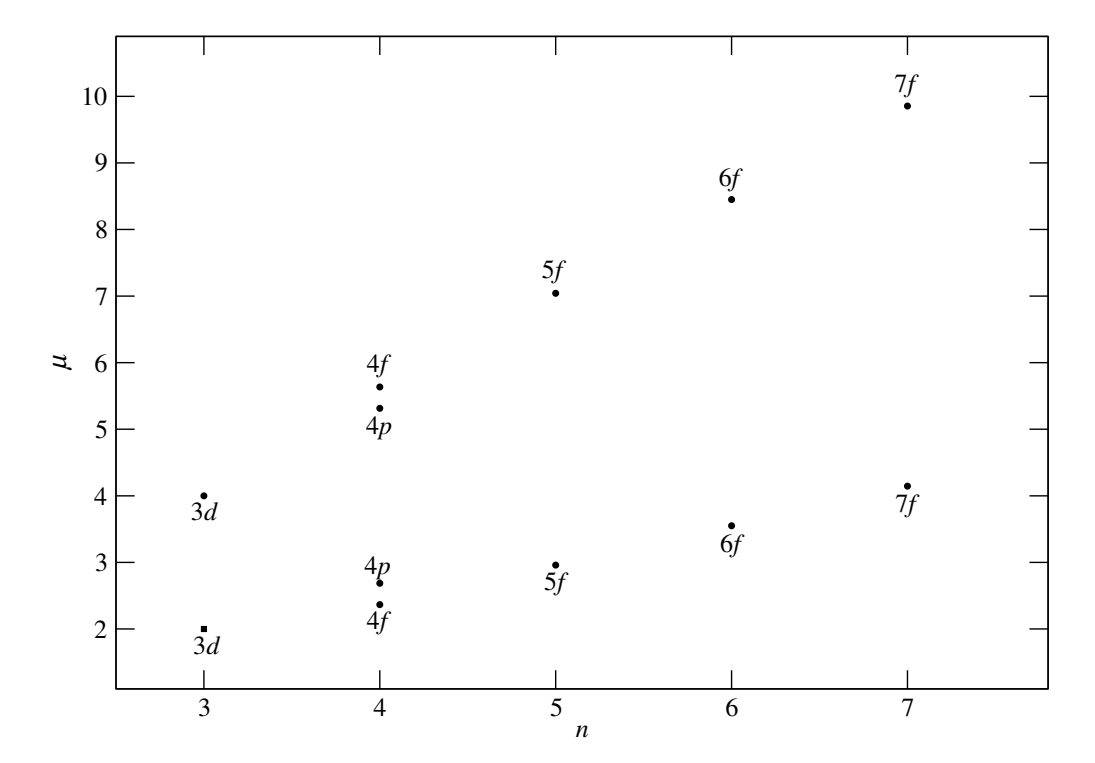


Figure 4.1: μ vs. n — Fe⁷⁺ NIST excitation energies.

Singly-excited doublet states.

The results of quantum defect estimations are shown in Figure 4.2. Since there are no data available for states where $\ell=4$ and above, the values of μ are estimated graphically and adjusted until the resulting term energies (obtained with Equation 4.1) fit as expected with the rest of the data. The resulting estimated term energies, along with those provided by

NIST, are shown in Table 4.3. These are the energies used to calculate the MCLZ SEC cross section of ${\rm Fe^{8+}}+X\to {\rm Fe^{7+}}+X^+$.

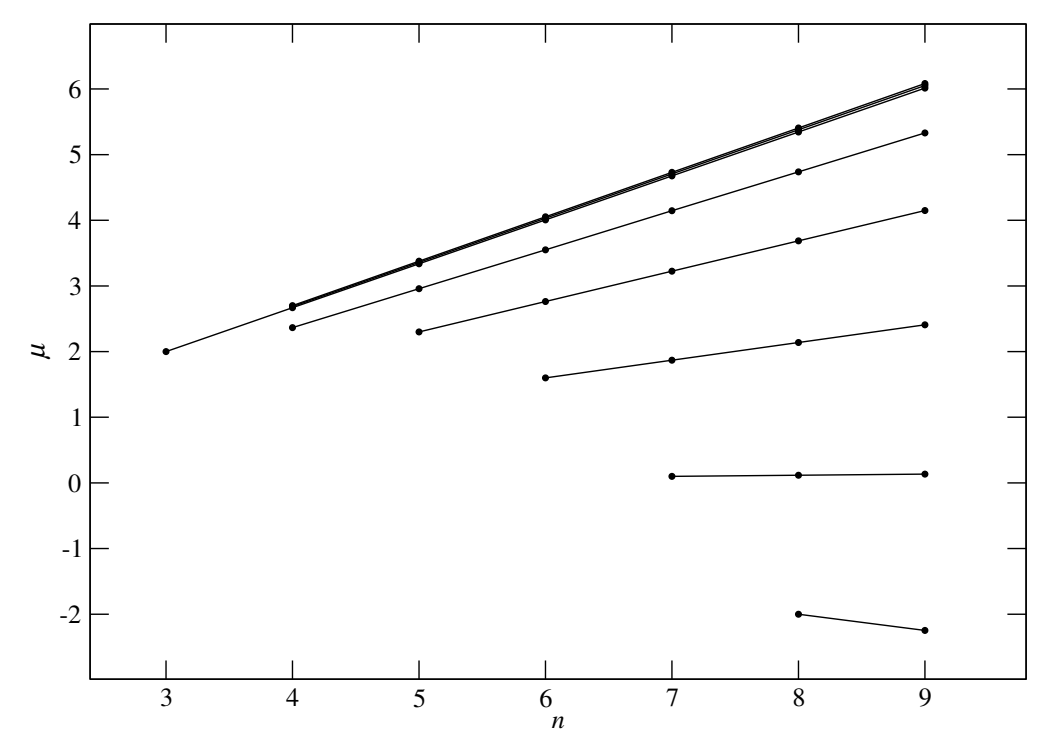


Figure 4.2: μ vs. n — Fe⁷⁺ estimated and NIST excitation energies. Singly-excited doublet states.

Table 4.3. Fe VIII (Fe $^{7+}$) Term Energies: Estimated and NIST.

Valence Electron	Term	Energy (cm^{-1})
3d	$^{2}\mathrm{D}$	0
3d	$^2\mathrm{F}^\circ$	432037
3d	$^2\mathrm{F}^\circ$	451575
4s	2 S	497445
3d	$^2\mathrm{P}^\circ$	511518
4p	$^2\mathrm{P}^\circ$	512691
4d	$^{2}\mathrm{D}$	530760
3d	$^2\mathrm{F}^\circ$	538988
3d	$^2\mathrm{P}^\circ$	592988
3d	$^2\mathrm{D}^\circ$	595656
5s	2 S	756060
4f	$^2\mathrm{F}^\circ$	762656
5p	$^{2}\mathrm{P}$	765836
5d	$^{2}\mathrm{D}$	777424
4s	$^2\mathrm{P}^\circ$	840005
4s	$^2\mathrm{F}^\circ$	856362
4s	$^2\mathrm{D}^\circ$	878849
4s	$^2\mathrm{F}^\circ$	884940
4s	$^2\mathrm{D}^\circ$	889051
6s	2 S	896896
6p	$^{2}\mathrm{P}$	903695
6d	$^{2}\mathrm{D}$	911752
5f	$^2\mathrm{F}^\circ$	925982
7s	$^2\mathrm{S}$	981963
7p	$^{2}\mathrm{P}$	986962
7d	$^{2}\mathrm{D}$	992888

Table 4.3 (cont'd)

Valence Electron	Term	Energy (cm^{-1})
6f	$^2\mathrm{F}^\circ$	1015464
8s	2 S	1037244
8p	$^{2}\mathrm{P}$	1041074
8d	$^{2}\mathrm{D}$	1045614
5g	$^{2}\mathrm{G}$	1051250
7f	$^2\mathrm{F}^\circ$	1068861
9s	$^2\mathrm{S}$	1075180
9p	$^{2}\mathrm{P}$	1078209
9d	$^{2}\mathrm{D}$	1081798
6g	$^{2}\mathrm{G}$	1102163
8f	$^2\mathrm{F}^\circ$	1103894
9f	$^2\mathrm{F}^\circ$	1127872
7g	^{2}G	1132915
8g	$^{2}\mathrm{G}$	1152899
6h	$^{2}\mathrm{H}$	1155447
9g	^{2}G	1166613
7h	$^{2}\mathrm{H}$	1172100
8h	$^{2}\mathrm{H}$	1182921
9h	$^{2}\mathrm{H}$	1190348
7i	$^2\mathrm{I}$	1192789
8i	^{2}I	1198773
9i	$^2\mathrm{I}$	1202880
8k	2 K	1206196
9k	2 K	1208748
9l	$^{2}\mathrm{L}$	1213309

Fe⁸⁺ has even fewer energies available which can be used to predict the missing values. Furthermore, this ion has a number of ambiguous states (i.e., it is unclear whether these ambiguous states are singlets or triplets). However, the same assumptions are used for Fe⁸⁺ as those used for Fe⁷⁺: the μ values are linear in n for a given ℓ , and they pass through the origin for n=0. For Fe⁸⁺, singlets and triplets are calculated separately. For the ambiguous states, assumptions are made whether these are included in the calculations for singlets or triplets. These assumptions are based on the electron configuration and term. For this ion, Wigner-Witmer rules are applied, and the resulting molecular channels are further divided into Σ and Π states. As with singlets and triplets, these are calculated separately. For these

Table 4.4. Fe IX (Fe $^{8+}$) NIST Atomic Energies.

Configuration	Term	J	Level (cm^{-1})	Term Energy (cm ⁻¹)
$3s^23p^6$	$^{1}\mathrm{S}$	0	0	0
$3s^23p^53d$	$^{3}\mathrm{P}^{\circ}$	0	405772	411007
1		1	408315.1	
		2	413669.2	
$3s^23p^53d$	${}^3\mathrm{F}^\circ$	4	425809.8	428883.7
		3	429310.9	
		2	433818.8	
$3s^23p^53d$	$^3\mathrm{D}^\circ$	3	455612.2	458948
		1	460616	
		2	462616.6	
$3s^23p^53d$	$^{1}\mathrm{D}^{\circ}$	2	456752.7	456752.7
$3s^23p^53d$	$^1\mathrm{F}^\circ$	3	465828.4	465828.4
$3s^23p^53d$	$^{1}\mathrm{P}^{\circ}$	1	584546	584546
$3s3p^63d$	$^{3}\mathrm{D}$	1	726734	728036
		2	727560	
		3	728935	
$3s3p^63d$	$^{1}\mathrm{D}$	2	749871	749871
$3s^23p^5(^2\mathrm{P}^{\circ}_{^{3/2}})4s$	$(3/2, 1/2)^{\circ}$	1	950500	950500
$3s^23p^5(^2\mathrm{P}^{\circ}_{^{1}/_{2}})4s$	$(1/2, 1/2)^{\circ}$	1	965570	965570
$3s^23p^54d$	$^{3}\mathrm{P}^{\circ}$	1	1198220	1198220
$3s^23p^54d$	$^{1}\mathrm{P}^{\circ}$	1	1213150	1213150
$3s^23p^5(^2\mathrm{P}^{\circ}_{^{3/2}})4f$	$^{2}[^{3}/_{2}]$	1	1300920	1302120
,		2	1302840	
$3s^23p^5(^2\mathrm{P}^{\circ}_{^{3/2}})4f$	$^{2}[^{9}/_{2}]$	5	1304600	1305374

states, there are also degeneracy factors which are needed in the cross section calculations, as shown in Table 4.7.

Table 4.4 (cont'd)

Configuration	Term	J	Level (cm^{-1})	Term Energy (cm ⁻¹)
		4	1306320	
$3s^23p^5(^2\mathrm{P}^{\circ}_{3/2})4f$	$^{2}[5/2]$	3	1305760	1305760
$3s^23p^5(^2\mathrm{P}_{3/2}^{\circ})4f$	$^{2}[7/_{2}]$	3	1310160	1311054
, ,=-		4	1311750	
$3s^23p^5(^2\mathrm{P}^{\circ}_{^{1/2}})4f$	$^{2}[5/2]$	3	1323660	1323660
$3s^23p^5(^2\mathrm{P}_{1/2}^{\circ'})4f$	$^{2}[7/_{2}]$	3	1324720	1324765
, ,=,		4	1324800	
$3s^23p^5(^2\mathrm{P}^{\circ}_{^{3/2}})5s$	$(3/2, 1/2)^{\circ}$	1	1358140	1358140
$3s3p^64p$	$^{1}\mathrm{P}^{\circ}$	1	1371910	1371910
$3s^2 3p^5 (^2 P_{1/2}^{\circ}) 5s$	$(1/2, 1/2)^{\circ}$	1	1372670	1372670
Fe X $(3p^{52}P_{3/2}^{\circ})$	Limit		1884000.3	

The available energies are sourced from the NIST database, and are shown in Table 4.4. Based on those term energies of the singly-excited states, the μ values are adjusted such that the resulting energy falls into an expected range, based on the other energies given. For example, a singly-exited state should have a lower energy than a similar state where the core is excited. An example would be as follows: the singly-excited state $3s^23p^54p(^1P^\circ)$ should have a lower energy than that for the core-excited state $3s3p^64p(^1P^\circ)$. The value of μ is adjusted in increments of 0.1 until the term energy falls into the appropriate range. In some cases, increments of μ are adjusted by 0.01 or even 0.001 until the energy for that state falls into a reasonable range. After μ is estimated for $3s^23p^54p(^1P^\circ)$, then μ is found for $3s^23p^55p(^1P^\circ)$, $3s^23p^56p(^1P^\circ)$, and so on, using the linear assumption. Next, it is assumed that $3s^23p^54s(^1S^\circ)$ will have a lower energy than $3s^23p^54p(^1P^\circ)$. So a similar adjustment of μ is made until the energy is satisfactorily estimated. Then the rest of the μ values for 5s, 6s, etc. can be calculated. The process continues for the next ℓ quantum number, d, then f, and so on. MCLZ SEC cross sections are calculated using the resulting estimated and given energies shown in Table 4.5 (singlets) and Table 4.6 (triplets).

Table 4.5. Fe IX (Fe $^{8+}$) Singlet Term Energies: Estimated and NIST.

Valence Electron	Term	Energy (cm^{-1})
3p	$^{1}\mathrm{S}$	0.000000000e+00
3d	$^{1}\mathrm{D}^{\circ}$	$4.56752700\mathrm{e}{+05}$
3d	$^{1}\mathrm{F}^{\circ}$	$4.65828400\mathrm{e}{+05}$
3d	$^{1}\mathrm{P}^{\circ}$	$5.84546000\mathrm{e}{+05}$
3d	$^{1}\mathrm{D}$	$7.49871000\mathrm{e}{+05}$
4s	$(1/2, 1/2)^{\circ}$	$9.65570000\mathrm{e}{+05}$
4d	$^{1}P^{\circ}$	$1.21315000\mathrm{e}{+06}$
4f	$^{2}[5/2]$	$1.32366000\mathrm{e}{+06}$
4f	$^{2}[7/_{2}]$	$1.32476500\mathrm{e}{+06}$
5p	^{1}P	$1.36958893\mathrm{e}{+06}$
5d	$^{1}\mathrm{D}$	$1.37019116\mathrm{e}{+06}$
4p	$^{1}\mathrm{P}^{\circ}$	$1.37191000\mathrm{e}{+06}$
5s	$^{(1/2, 1/2)^{\circ}}_{}^{1}\mathrm{F}$	$1.37267000\mathrm{e}{+06}$
5f	$^{1}\mathrm{F}$	$1.51143825\mathrm{e}{+06}$
6s	$^{1}\mathrm{S}$	$1.52630306\mathrm{e}{+06}$
6p	$^{1}\mathrm{P}$	$1.52677018\mathrm{e}{+06}$
6d	$^{1}\mathrm{D}$	$1.52718840\mathrm{e}{+06}$
5g	$^{1}\mathrm{G}$	$1.55691692\mathrm{e}{+06}$
7s	$^{1}\mathrm{S}$	$1.62120233\mathrm{e}{+06}$
7p	$^{1}\mathrm{P}$	$1.62154552\mathrm{e}{+06}$
7d	$^{1}\mathrm{D}$	$1.62185278\mathrm{e}{+06}$
6f	$^{1}\mathrm{F}$	$1.62527665\mathrm{e}{+06}$
6g	$^{1}\mathrm{G}$	$1.65685906\mathrm{e}{+06}$
8s	$^{1}\mathrm{S}$	$1.68279560\mathrm{e}{+06}$
8p	$^{1}\mathrm{P}$	$1.68305836\mathrm{e}{+06}$
8d	$^{1}\mathrm{D}$	$1.68329361\mathrm{e}{+06}$

Table 4.5 (cont'd)

Valence Electron	Term	Energy (cm^{-1})
6h	$^{1}\mathrm{H}$	1.68795448e + 06
7f	$^{1}\mathrm{F}$	$1.69391762\mathrm{e}{+06}$
7g	$^{1}\mathrm{G}$	$1.71712102\mathrm{e}{+06}$
9s	$^{1}\mathrm{S}$	$1.72502375\mathrm{e}{+06}$
9p	$^{1}\mathrm{P}$	$1.72523136\mathrm{e}{+06}$
9d	$^{1}\mathrm{D}$	$1.72541723\mathrm{e}{+06}$
8f	$^{1}\mathrm{F}$	$1.73846825\mathrm{e}{+06}$
7h	$^{1}\mathrm{H}$	1.73996664e+06
7i	$^{1}\mathrm{I}$	$1.74638158\mathrm{e}{+06}$
8g	$^{1}\mathrm{G}$	$1.75623335\mathrm{e}{+06}$
9f	$^{1}\mathrm{F}$	$1.76901201\mathrm{e}{+06}$
8h	$^{1}\mathrm{H}$	1.77372453e + 06
8i	^{1}I	1.77863597e + 06
9g	$^{1}\mathrm{G}$	$1.78304864\mathrm{e}{+06}$
8k	$^{1}\mathrm{K}$	$1.79096325\mathrm{e}{+06}$
9h	$^{1}\mathrm{H}$	1.79686883e+06
9i	$^{1}\mathrm{I}$	$1.80074947\mathrm{e}{+06}$
9k	$^{1}\mathrm{K}$	$1.81048954\mathrm{e}{+06}$
9l	$^{1}\mathrm{L}$	1.82171930e + 06

Table 4.6. Fe IX (Fe $^{8+})$ Triplet Term Energies: Estimated and NIST.

Valence Electron	Term	Energy (cm^{-1})
3d	³ P°	$4.11007000\mathrm{e}{+05}$
3d	$^3\mathrm{F}^\circ$	$4.28883700\mathrm{e}{+05}$
3d	$^3\mathrm{D}^\circ$	$4.58948000\mathrm{e}{+05}$
3d	$^{3}\mathrm{D}$	$7.28036000\mathrm{e}{+05}$
4s	$(3/2, 1/2)^{\circ}$	$9.50500000\mathrm{e}{+05}$
4d	$^{3}P^{\circ}$	$1.19822000\mathrm{e}{+06}$
4p	$^{3}\mathrm{P}$	$1.29046568\mathrm{e}{+06}$
4f	$^{2}[3/_{2}]$	$1.30212000\mathrm{e}{+06}$
4f	$^{2}[^{9}/_{2}]$	$1.30537400\mathrm{e}{+06}$
4f	$^{2}[^{5}/_{2}]$	$1.30576000\mathrm{e}{+06}$
4f	$^{2}[7/_{2}]$	$1.31105400\mathrm{e}{+06}$
5p	^{3}P	$1.35624063\mathrm{e}{+06}$
5s	$(3/2, 1/2)^{\circ}$	$1.35814000\mathrm{e}{+06}$
5d	$^{3}\mathrm{D}$	$1.35814943\mathrm{e}{+06}$
5f	$^{3}\mathrm{F}$	$1.50413814\mathrm{e}{+06}$
6s	$^3\mathrm{S}$	$1.51701127\mathrm{e}{+06}$
6p	$^{3}\mathrm{P}$	$1.51750053\mathrm{e}{+06}$
6d	$^{3}\mathrm{D}$	$1.51882609\mathrm{e}{+06}$
5g	$^{3}\mathrm{G}$	$1.55070963\mathrm{e}{+06}$
7s	3S	$1.61437571\mathrm{e}{+06}$
7p	$^{3}\mathrm{P}$	$1.61473516\mathrm{e}{+06}$
7d	$^{3}\mathrm{D}$	$1.61570904\mathrm{e}{+06}$
6f	$^3\mathrm{F}$	$1.62020713\mathrm{e}{+06}$
6g	^{3}G	$1.65254845\mathrm{e}{+06}$
8s	$^3\mathrm{S}$	$1.67756897\mathrm{e}{+06}$
8p	$^{3}\mathrm{P}$	$1.67784418\mathrm{e}{+06}$

Table 4.6 (cont'd)

Valence Electron	Term	Energy (cm^{-1})
8d	$^{3}\mathrm{D}$	$1.67858980\mathrm{e}{+06}$
6h	$^{3}\mathrm{H}$	$1.68446797\mathrm{e}{+06}$
7f	$^{3}\mathrm{F}$	$1.69019308\mathrm{e}{+06}$
7g	$^{3}\mathrm{G}$	$1.71395404\mathrm{e}{+06}$
9s	$^3\mathrm{S}$	$1.72089407\mathrm{e}{+06}$
9p	$^{3}\mathrm{P}$	$1.72111151\mathrm{e}{+06}$
9d	$^{3}\mathrm{D}$	$1.72170065\mathrm{e}{+06}$
8f	$^{3}\mathrm{F}$	$1.73561664\mathrm{e}{+06}$
7h	$^{3}\mathrm{H}$	$1.73740512\mathrm{e}{+06}$
7i	^{3}I	$1.74386209\mathrm{e}{+06}$
8g	$^{3}\mathrm{G}$	$1.75380863\mathrm{e}{+06}$
9f	$^{3}\mathrm{F}$	$1.76675889\mathrm{e}{+06}$
8h	$^{3}\mathrm{H}$	$1.77176336\mathrm{e}{+06}$
8i	^{3}I	$1.77670698\mathrm{e}{+06}$
9g	$^{3}\mathrm{G}$	$1.78113281\mathrm{e}{+06}$
8k	$^{3}\mathrm{K}$	$1.78937009\mathrm{e}{+06}$
9h	$^{3}\mathrm{H}$	$1.79531926\mathrm{e}{+06}$
9i	^{3}I	$1.79922533\mathrm{e}{+06}$
9k	$^{3}\mathrm{K}$	$1.80923075\mathrm{e}{+06}$
91	^{3}L	$1.82078846\mathrm{e}{+06}$

$4.2 ext{ Fe}^{9+}$

For systems where the neutral atom is not hydrogen-like, it is necessary to perform separate calculations for Σ and Π states using degeneracy factors shown in Table 4.7, according to Wigner-Witmer rules. These Σ and Π calculations are combined into single cross-section results for each system, shown in Figures 4.3–4.17.

Table 4.7. Degeneracy Factors.

State	Factor
$^{1}\Sigma$ $^{1}\Pi$ $^{3}\Sigma$ $^{3}\Pi$	0.08333 0.1667 0.2500 0.5000

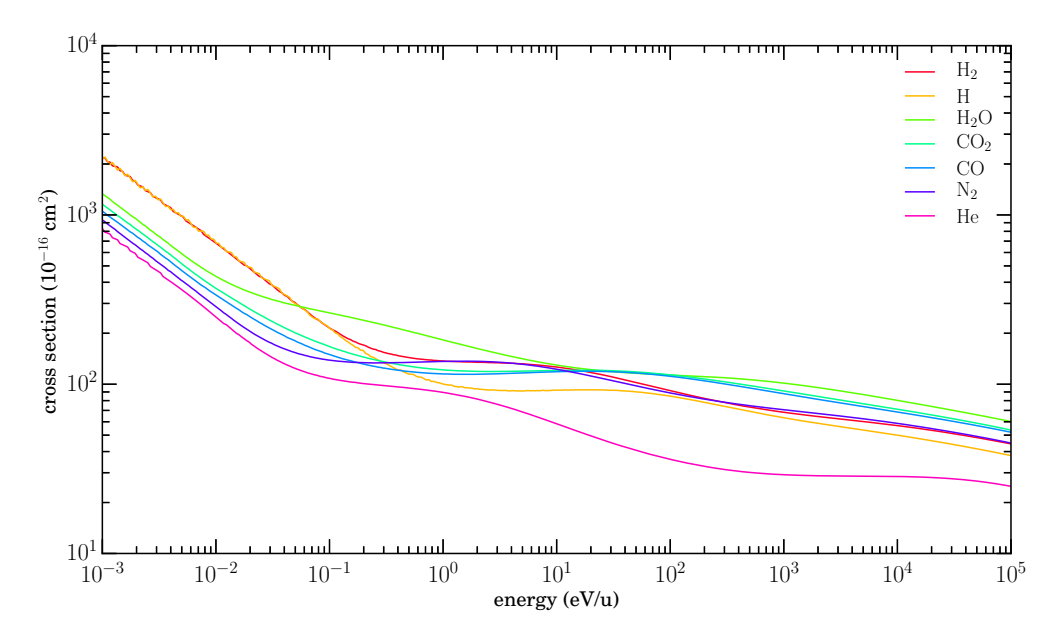


Figure 4.3: $\text{Fe}^{9+} + X \rightarrow \text{Fe}^{8+} + X^+$ total cross sections.

$4.2.1 ext{ FE}^{9+} + H$

For this system, singlet and triplet cross sections are calculated separately. Furthermore, separate calculations are performed for Σ and Π states for the singlets and triplets. Thus, there are 4 separate calculations performed for Fe⁹⁺+H \rightarrow Fe⁸⁺+H⁺, identified by $^{1}\Sigma$, $^{1}\Pi$, $^{3}\Sigma$ and $^{3}\Pi$, shown in Figure 4.4. These four results are summed into a final result, shown in Figure 4.5.

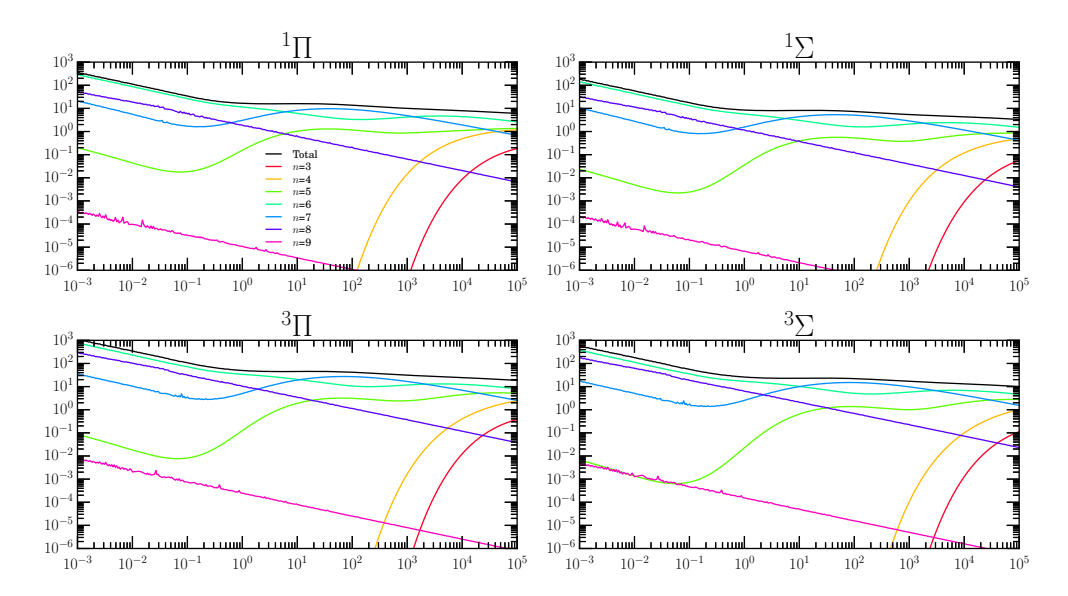


Figure 4.4: Fe⁹⁺+H \rightarrow Fe⁸⁺+H⁺ n-resolved cross sections.

 $^{1}\Pi$, $^{1}\Sigma$, $^{3}\Pi$, $^{3}\Sigma$.

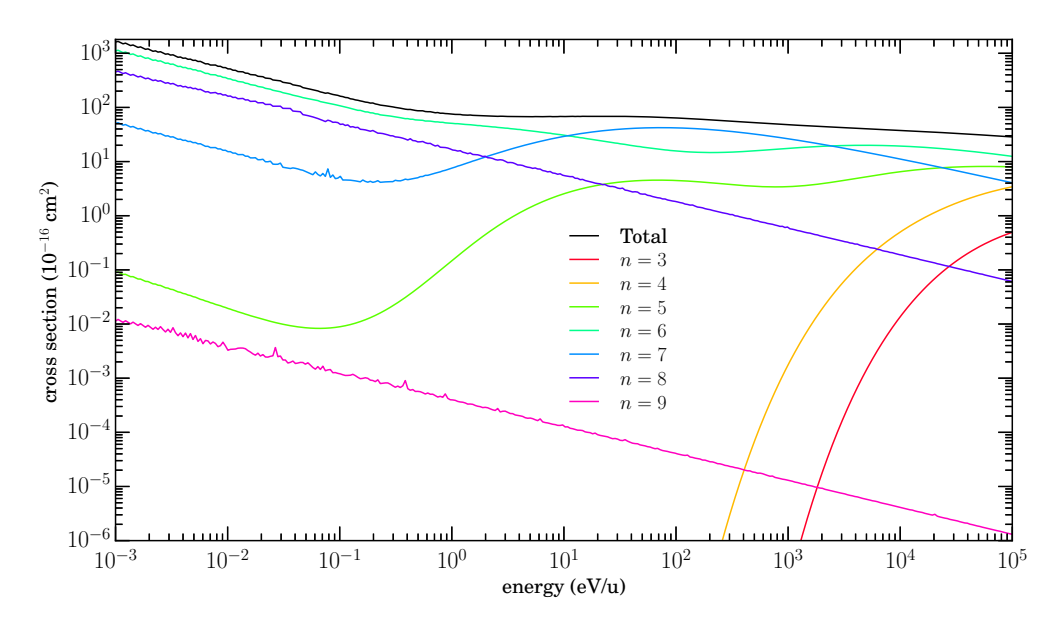


Figure 4.5: $Fe^{9+}+H\rightarrow Fe^{8+}+H^+$ n-resolved cross sections.

$$^{1}\Pi + ^{1}\Sigma + ^{3}\Pi + ^{3}\Sigma.$$

$4.2.2 ext{ FE}^{9+} + H_2$

Figure 4.6 shows $n\ell$ -resolved cross sections for $\text{Fe}^{9+} + \text{H}_2 \rightarrow \text{Fe}^{8+} + \text{H}_2^+$, and Figure 4.7 shows n-resolved cross sections for this system. There are no other known available data for comparison. The dominant channels are listed in Table 4.8.

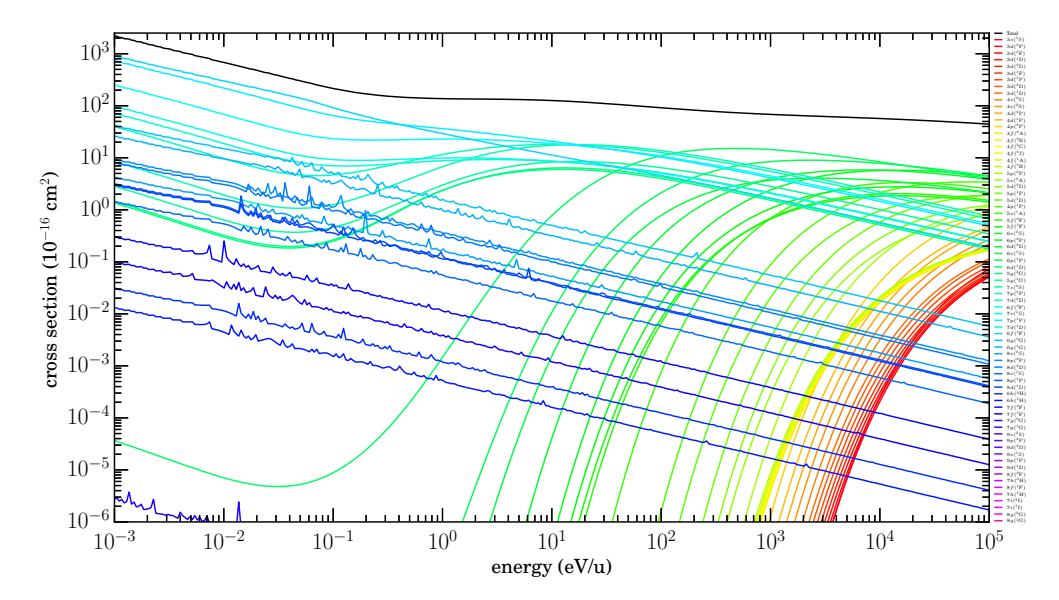


Figure 4.6: Fe⁹⁺+H₂ \rightarrow Fe⁸⁺+H₂⁺ $n\ell$ -resolved cross sections.

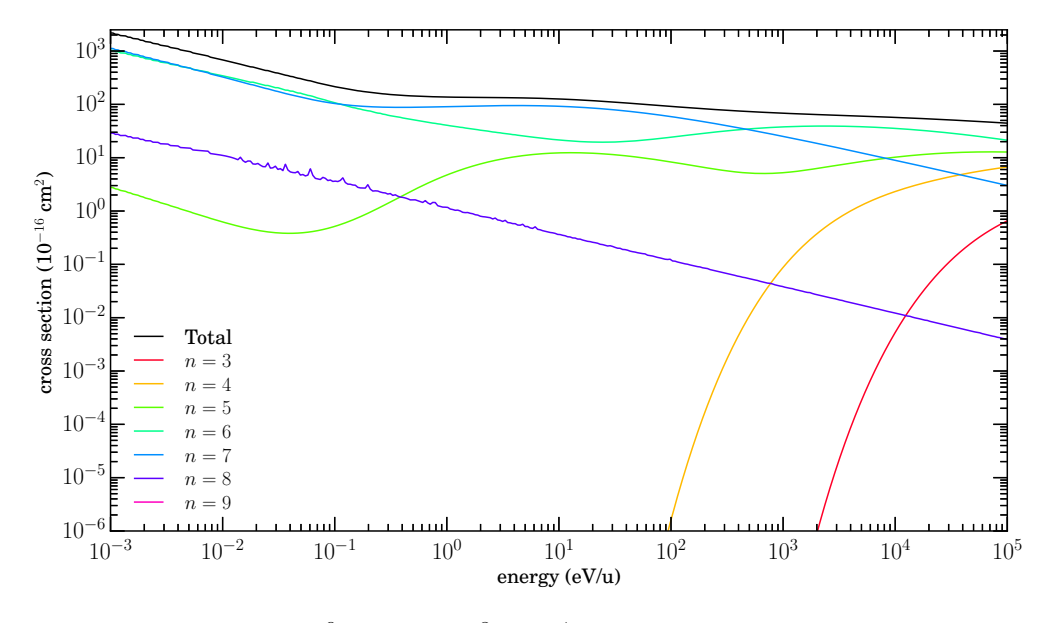


Figure 4.7: Fe⁹⁺+H₂ \rightarrow Fe⁸⁺+H₂⁺ n-resolved cross sections.

$4.2.3 ext{ FE}^{9+} + ext{HE}$

Figure 4.8 shows $n\ell$ -resolved cross sections for $Fe^{9+}+He \rightarrow Fe^{8+}+He^{+}$, and Figure 4.9 shows n-resolved cross sections for this system. There are no other known available data for comparison. The dominant channels are listed in Table 4.8.

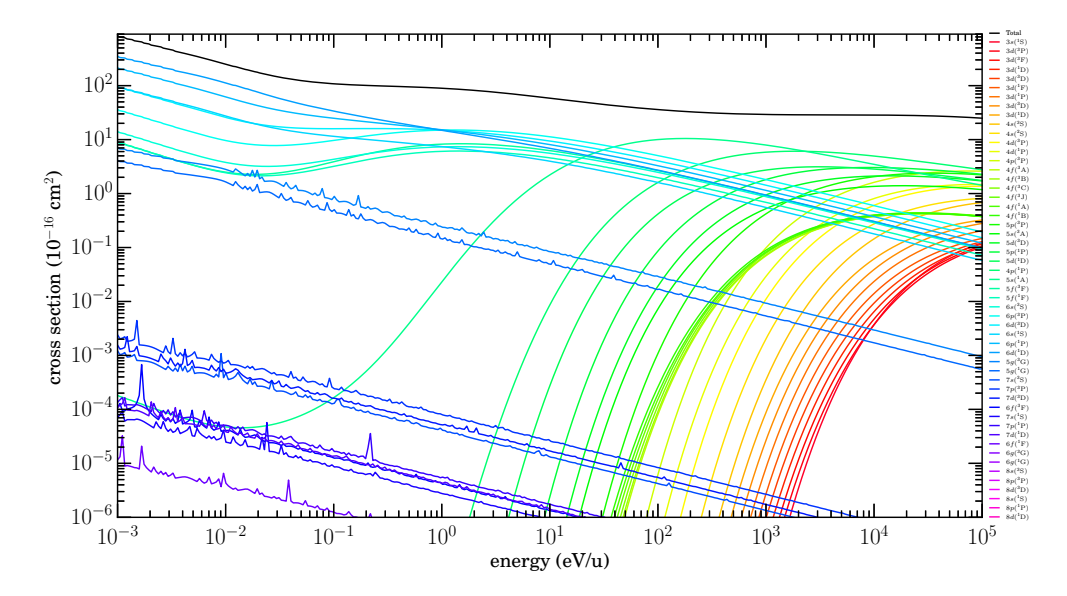


Figure 4.8: $Fe^{9+}+He\rightarrow Fe^{8+}+He^+$ n-resolved cross sections.

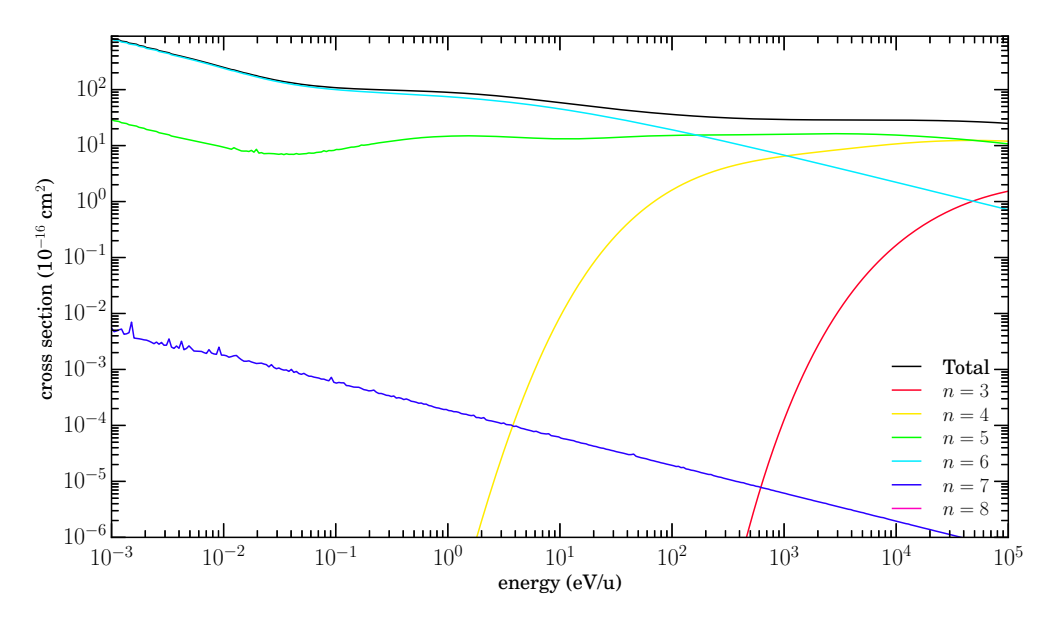


Figure 4.9: $Fe^{9+}+He\rightarrow Fe^{8+}+He^+$ *n*-resolved cross sections.

$4.2.4 ext{ FE}^{9+} + H_2O$

Figure 4.10 shows $n\ell$ -resolved cross sections for Fe⁹⁺+H₂O \rightarrow Fe⁸⁺+H₂O⁺. And Figure 4.11 shows n-resolved cross sections for this system along with CTMC and experimental total cross sections from Simcic et al. (2010a), which are in close agreement with the MCLZ total cross section.

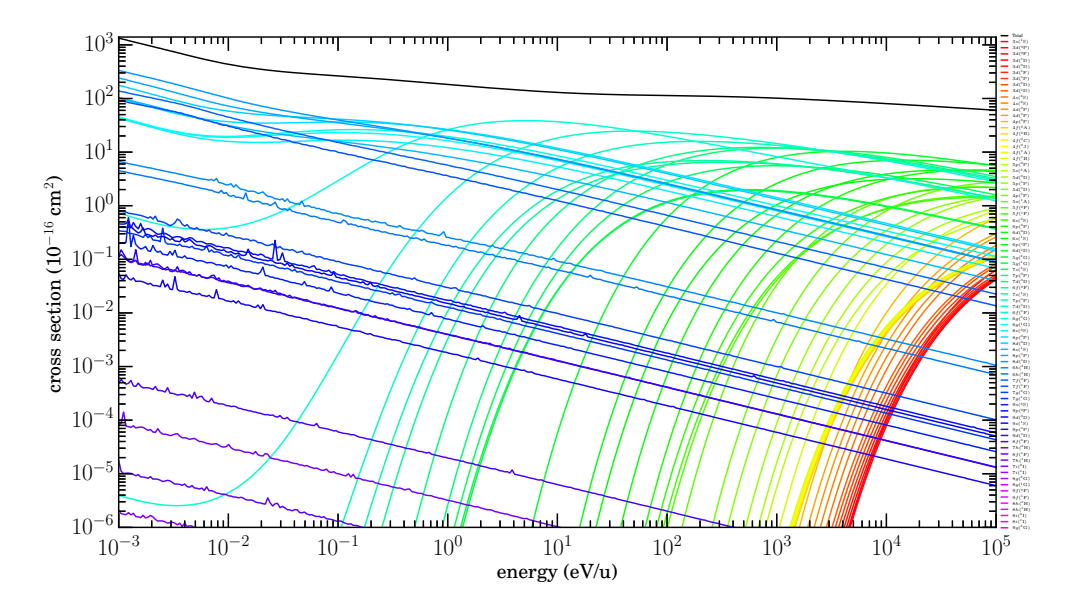


Figure 4.10: Fe⁹⁺+H₂O \rightarrow Fe⁸⁺+H₂O⁺ $n\ell$ -resolved cross sections.

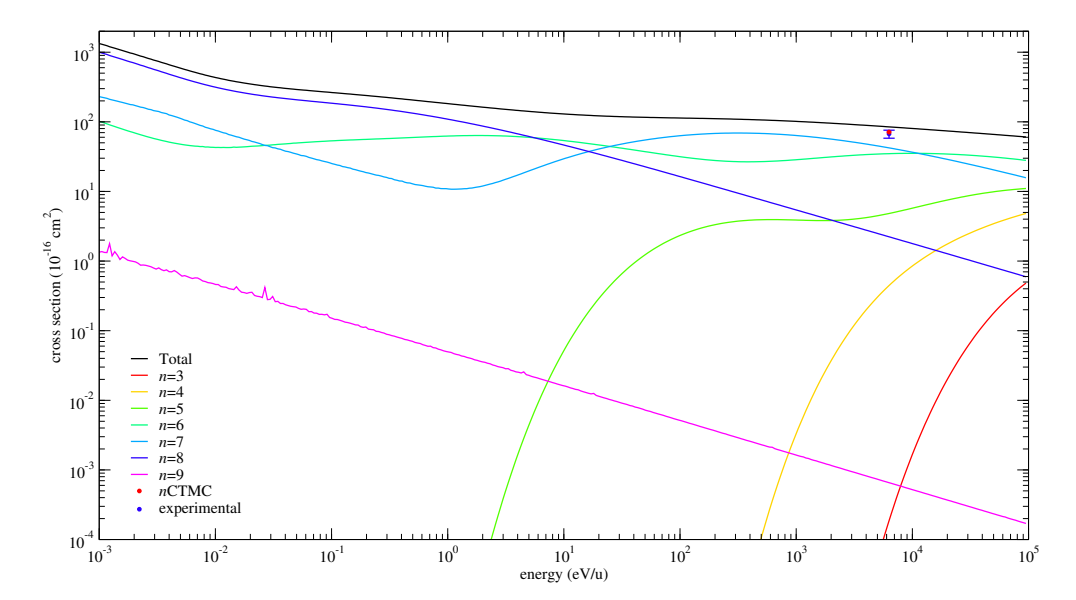


Figure 4.11: Fe⁹⁺+H₂O \rightarrow Fe⁸⁺+H₂O⁺ n-resolved cross sections.

MCLZ comparision to CTMC and experimental results of Simcic et al. (2010a).

$4.2.5 ext{ FE}^{9+} + CO$

Figure 4.12 shows $n\ell$ -resolved cross sections for Fe⁹⁺+CO \rightarrow Fe⁸⁺+CO⁺. And Figure 4.13 shows n-resolved cross sections for this system along with CTMC and experimental total cross sections from Simcic et al. (2010b), which are in close agreement with the MCLZ total cross section.

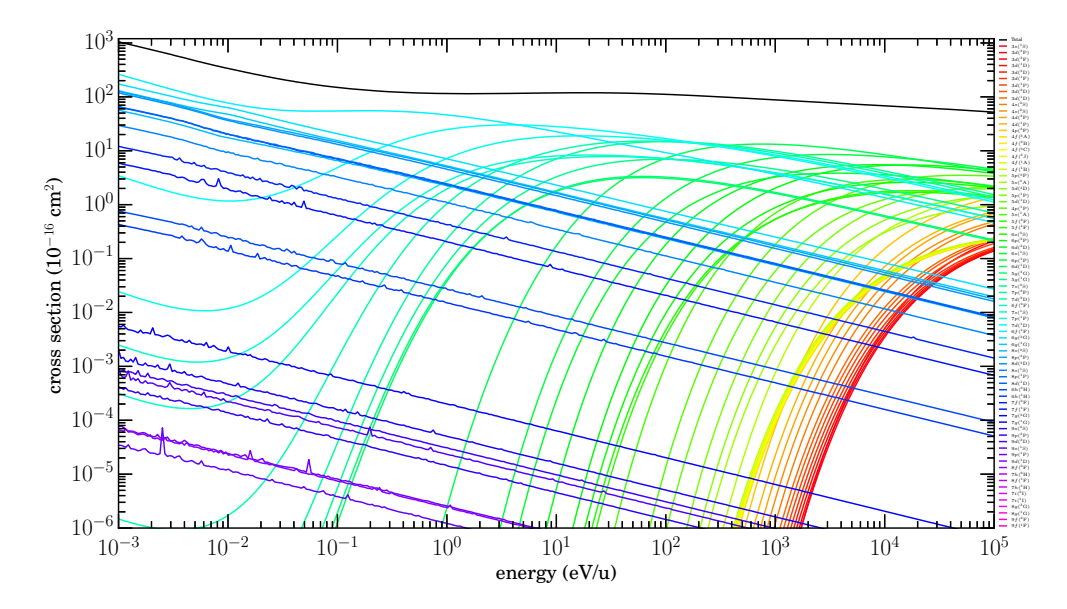


Figure 4.12: Fe⁹⁺+CO \rightarrow Fe⁸⁺+CO⁺ $n\ell$ -resolved cross sections.

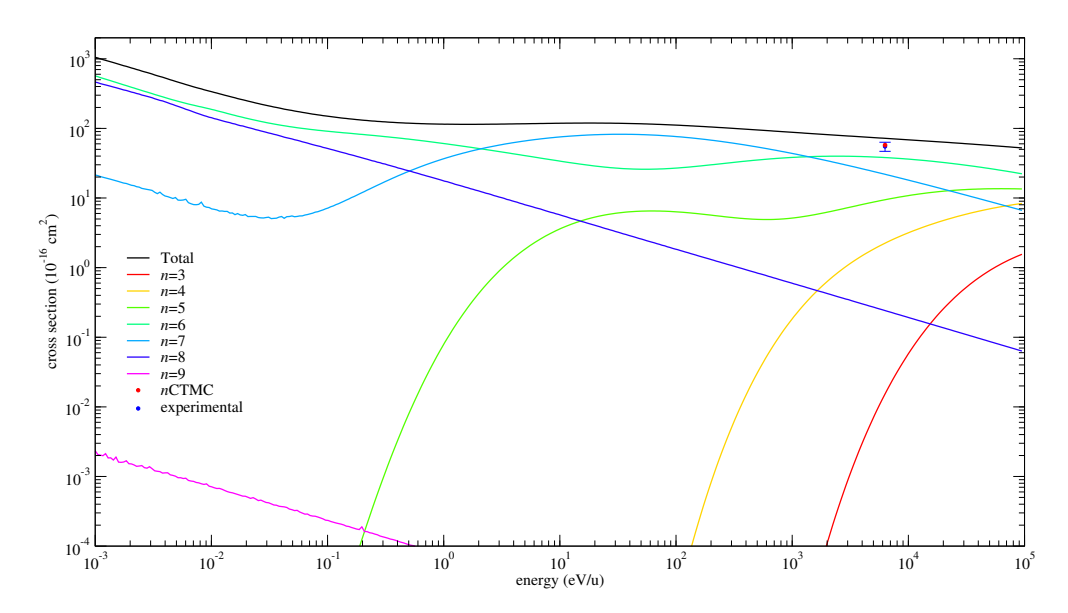


Figure 4.13: $Fe^{9+}+CO \rightarrow Fe^{8+}+CO^{+}$ n-resolved cross sections.

MCLZ comparision to CTMC and experimental results of Simcic et al. (2010b).

$4.2.6 \text{ FE}^{9+} + \text{CO}_2$

Figure 4.14 shows $n\ell$ -resolved cross sections for Fe⁹⁺+CO₂ \rightarrow Fe⁸⁺+CO₂⁺. And Figure 4.15 shows n-resolved cross sections for this system along with CTMC and experimental total

cross sections from Simcic et al. (2010b), which are in close agreement with the MCLZ total cross section.

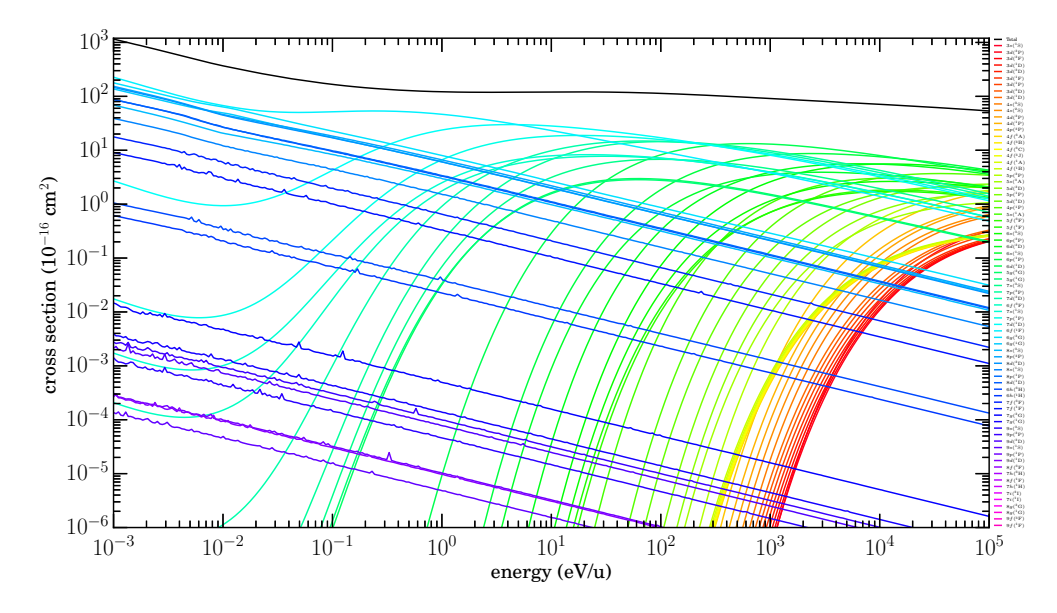


Figure 4.14: Fe⁹⁺+CO₂ \rightarrow Fe⁸⁺+CO₂⁺ $n\ell$ -resolved cross sections.

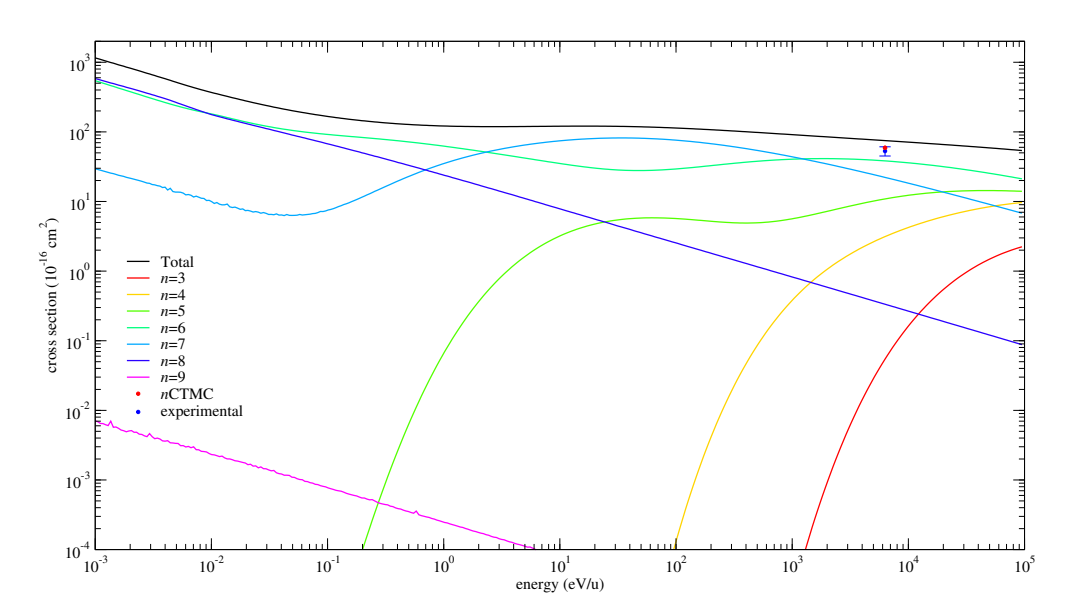


Figure 4.15: Fe⁹⁺+CO₂ \rightarrow Fe⁸⁺+CO₂⁺ n-resolved cross sections.

MCLZ comparision to CTMC and experimental results of Simcic et al. (2010b).

$4.2.7 \quad FE^{9+} + N_2$

Figure 4.16 shows $n\ell$ -resolved cross sections for $\mathrm{Fe^{9+}} + \mathrm{N_2} \rightarrow \mathrm{Fe^{8+}} + \mathrm{N_2^+}$, and Figure 4.17 shows n-resolved cross sections for this system. There are no other known available data for comparison. The dominant channels are listed in Table 4.8.

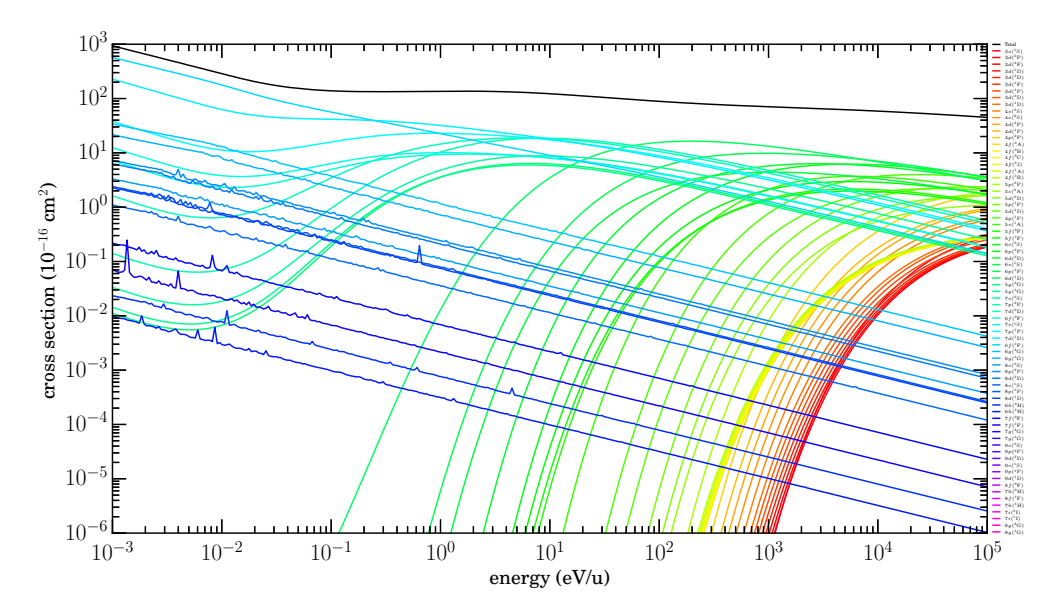


Figure 4.16: Fe⁹⁺+N₂ \rightarrow Fe⁸⁺+N₂⁺ $n\ell$ -resolved cross sections.

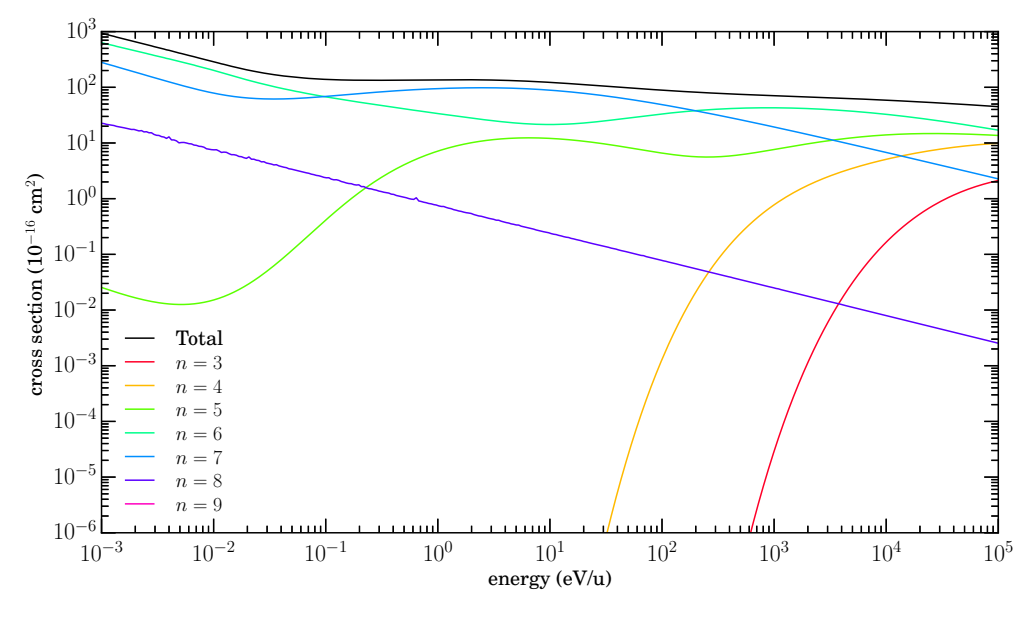


Figure 4.17: Fe⁹⁺+N₂ \rightarrow Fe⁸⁺+N₂⁺ n-resolved cross sections.

4.3 FE^{8+}

The energies (Table 4.3) are calculated from the estimated values of μ , and cross sections are obtained from these energies using the MCLZ method. Plots of these cross sections are shown in Figures 4.18–4.32. Comparisons are made with data available from Simcic et al. (2010a,b), and the results are in agreement. For those systems where no cross sectional data are available, the method used was shown to be sufficiently accurate for Ne and Mg ionic systems (Lyons et al. 2017) in the energy ranges which are presented here.

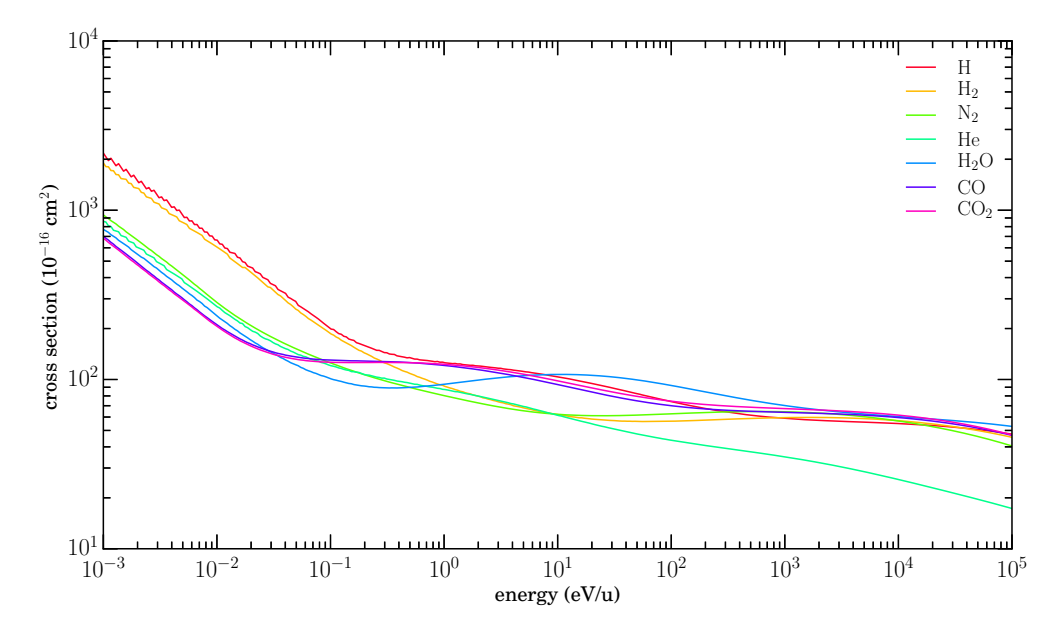


Figure 4.18: $Fe^{8+}+X\rightarrow Fe^{7+}+X^+$ total cross sections.

$4.3.1 \text{ Fe}^{8+} + \text{H}$

Figure 4.19 shows $n\ell$ -resolved cross sections for Fe⁸⁺+H \rightarrow Fe⁷⁺+H⁺, and Figure 4.20 shows n-resolved cross sections for this system. There are no other known available data for comparison. The dominant channels are listed in Table 4.8.

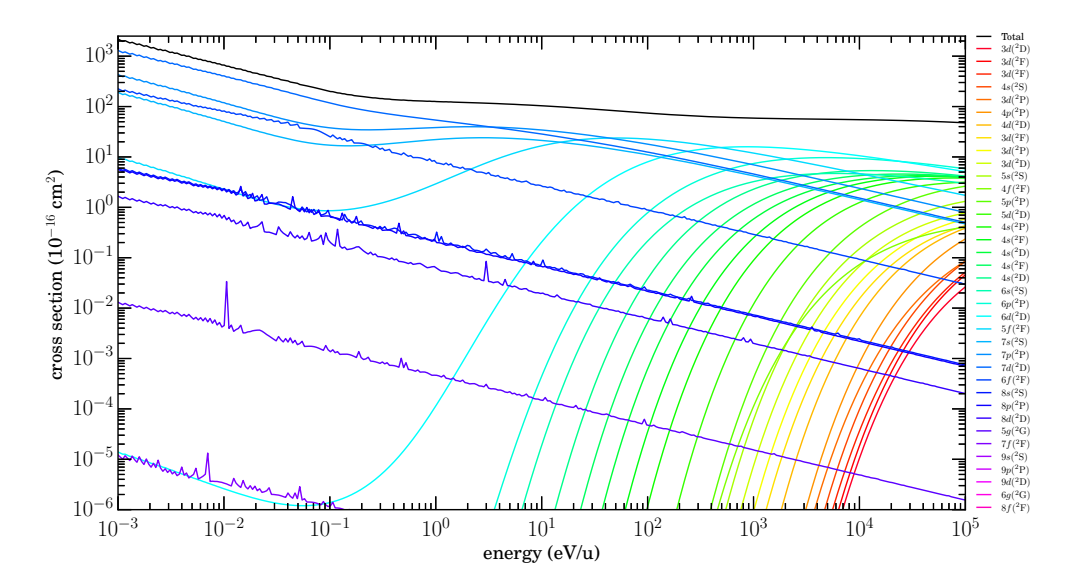


Figure 4.19: Fe⁸⁺+H \rightarrow Fe⁷⁺+H⁺ $n\ell$ -resolved cross sections.

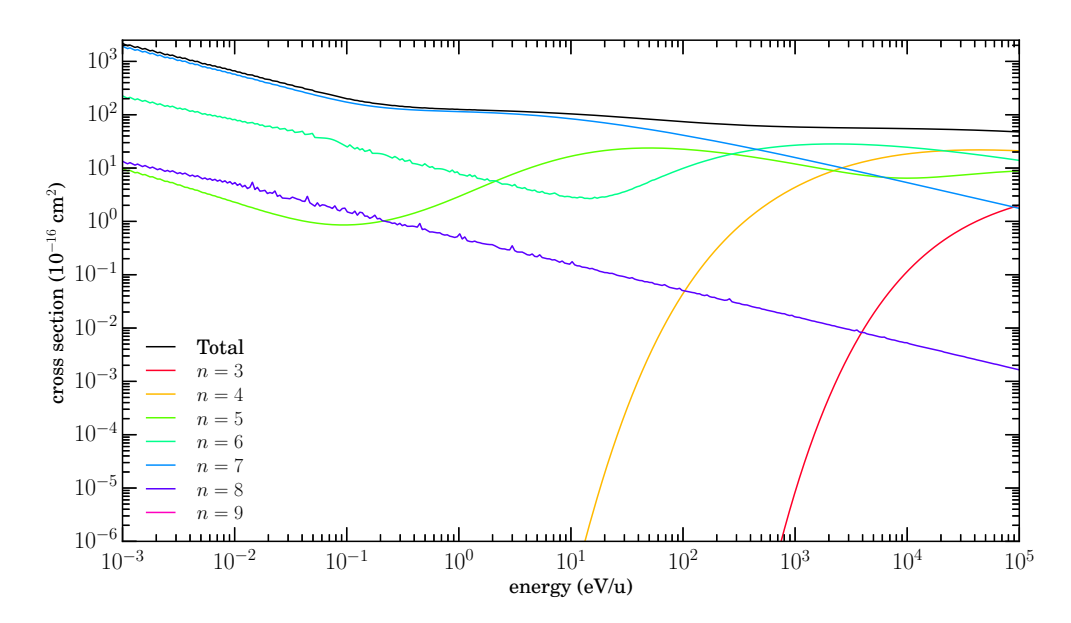


Figure 4.20: Fe⁸⁺+H \rightarrow Fe⁷⁺+H⁺ n-resolved cross sections.

$4.3.2 \text{ FE}^{8+} + \text{H}_2$

Figure 4.21 shows $n\ell$ -resolved cross sections for $\mathrm{Fe^{8+}} + \mathrm{H_2} \rightarrow \mathrm{Fe^{7+}} + \mathrm{H_2^+}$, and Figure 4.22 shows n-resolved cross sections for this system. There are no other known available data for comparison. The dominant channels are listed in Table 4.8.

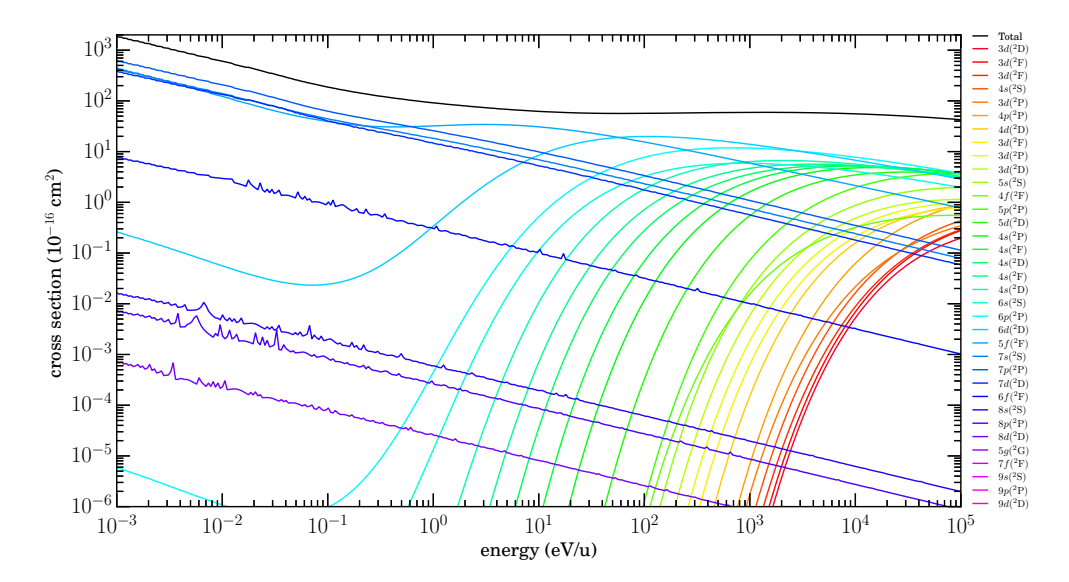


Figure 4.21: Fe⁸⁺+H₂ \rightarrow Fe⁷⁺+H₂⁺ $n\ell$ -resolved cross sections..

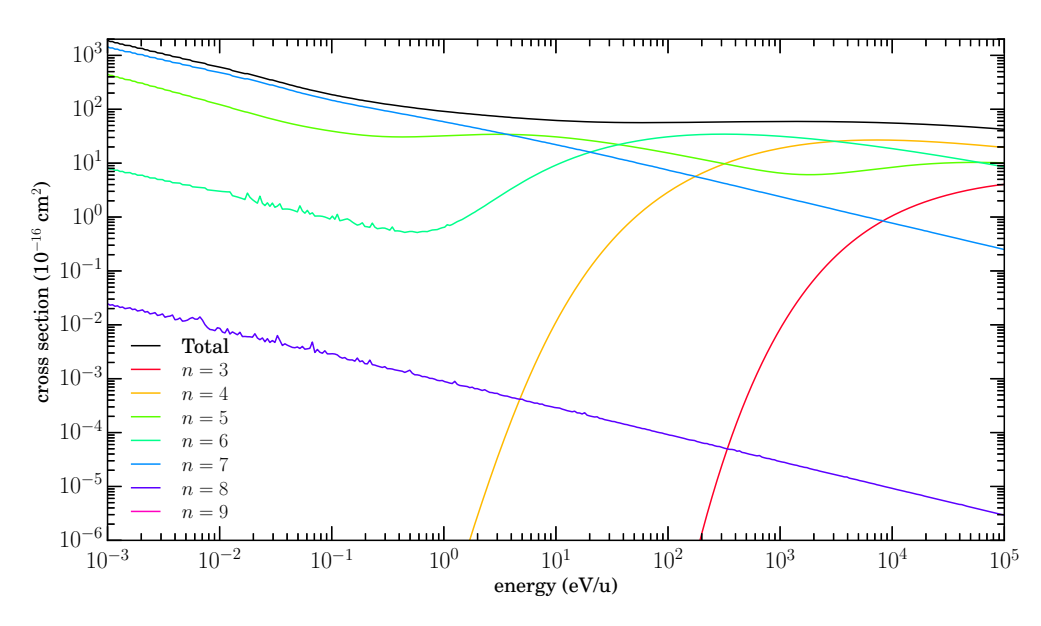


Figure 4.22: Fe⁸⁺+H₂ \rightarrow Fe⁷⁺+H₂⁺ n-resolved cross sections..

$4.3.3 ext{ FE}^{8+} + ext{He}$

Figure 4.23 shows $n\ell$ -resolved cross sections for Fe⁸⁺+He \rightarrow Fe⁷⁺+He⁺, and Figure 4.24 shows n-resolved cross sections for this system. There are no other known available data for comparison. The dominant channels are listed in Table 4.8.

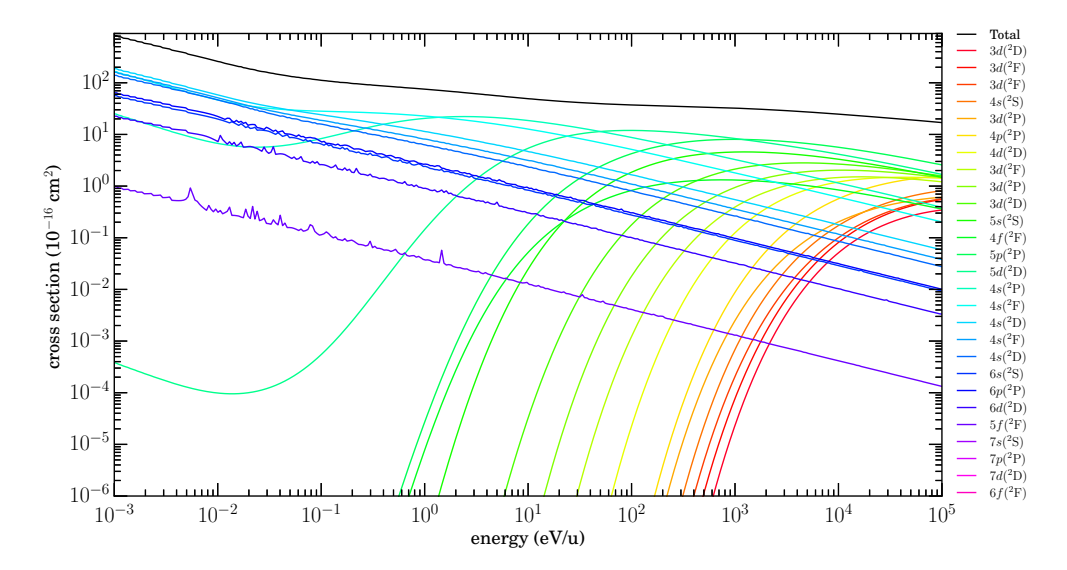


Figure 4.23: $Fe^{8+}+He\rightarrow Fe^{7+}+He^+$ $n\ell$ -resolved cross sections.

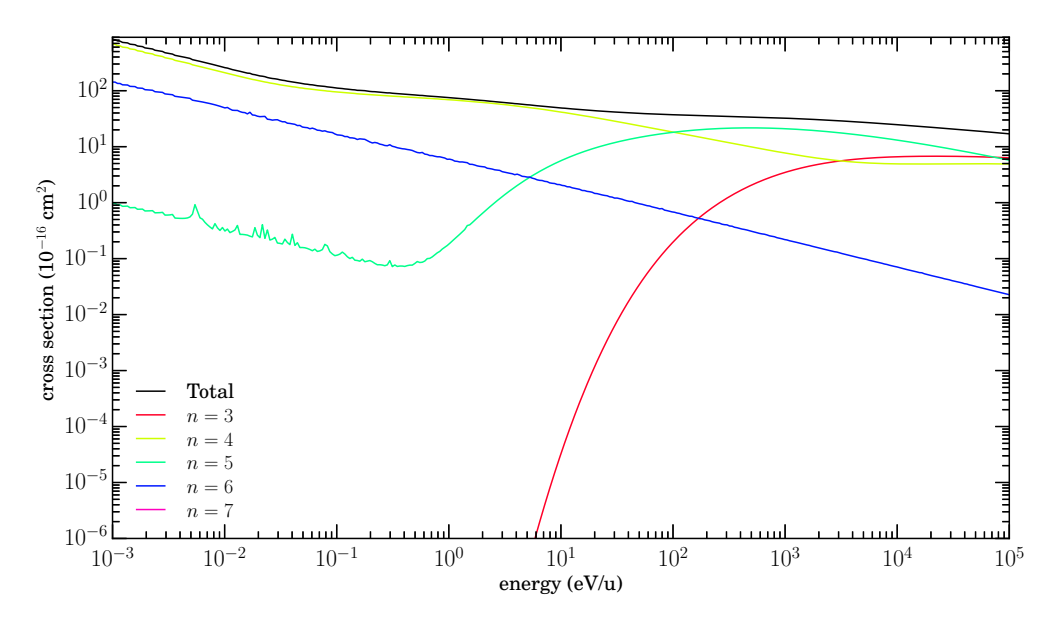


Figure 4.24: $Fe^{8+}+He\rightarrow Fe^{7+}+He^{+}$ n-resolved cross sections.

$4.3.4 \text{ Fe}^{8+} + \text{H}_2\text{O}$

Figure 4.25 shows $n\ell$ -resolved cross sections for Fe⁸⁺+H₂O \rightarrow Fe⁷⁺+H₂O⁺. And Figure 4.26 shows n-resolved cross sections for this system along with CTMC and experimental total

cross sections from Simcic et al. (2010a), which are in close agreement with the MCLZ total cross section.

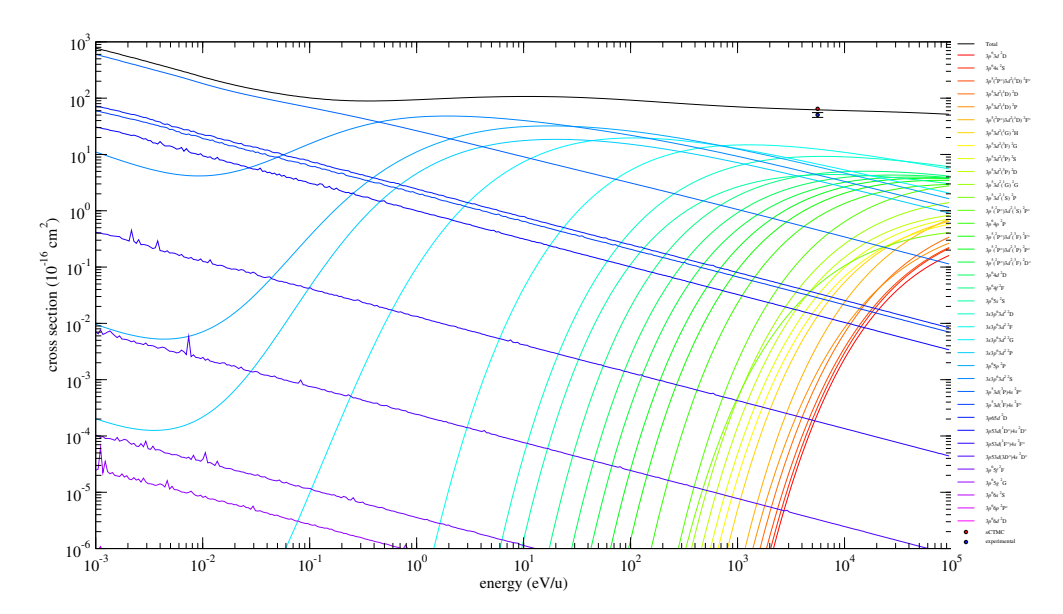


Figure 4.25: Fe⁸⁺+H₂O \rightarrow Fe⁷⁺+H₂O⁺ $n\ell$ -resolved cross sections.

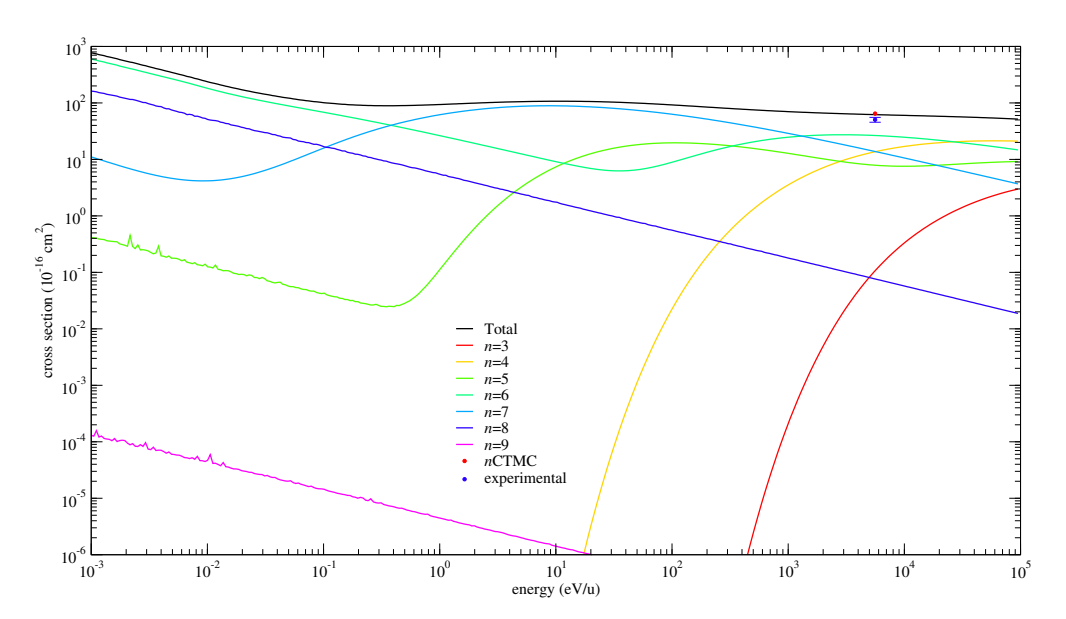


Figure 4.26: Fe⁸⁺+H₂O \rightarrow Fe⁷⁺+H₂O⁺ n-resolved cross sections.

MCLZ comparision to CTMC and experimental results of Simcic et al. (2010a) .

$4.3.5 ext{ FE}^{8+} + ext{CO}$

Figure 4.27 shows $n\ell$ -resolved cross sections for Fe⁸⁺+CO \rightarrow Fe⁷⁺+CO⁺. And Figure 4.28 shows n-resolved cross sections for this system along with CTMC and experimental total cross sections from Simcic et al. (2010b), which are in close agreement with the MCLZ total cross section.

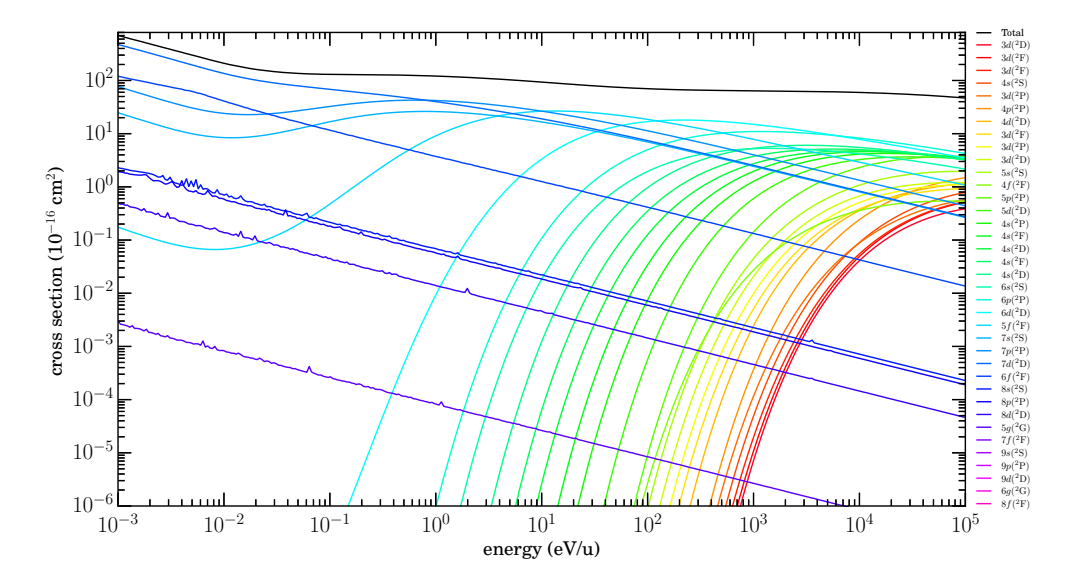


Figure 4.27: Fe⁸⁺+CO \rightarrow Fe⁷⁺+CO⁺ $n\ell$ -resolved cross sections.

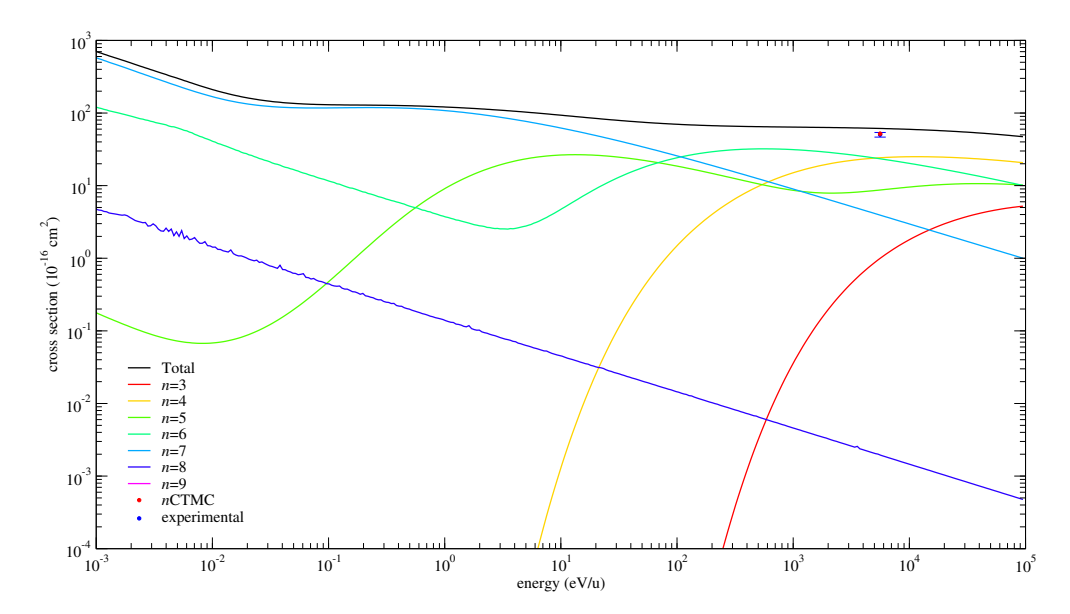


Figure 4.28: $Fe^{8+}+CO\rightarrow Fe^{7+}+CO^{+}$ n-resolved cross sections.

MCLZ comparision to CTMC and experimental results of Simcic et al. (2010b) .

$4.3.6 ext{ FE}^{8+} + ext{CO}_2$

Figure 4.29 shows $n\ell$ -resolved cross sections for $\mathrm{Fe^{8+}} + \mathrm{CO_2} \rightarrow \mathrm{Fe^{7+}} + \mathrm{CO_2}^+$. And Figure 4.30 shows n-resolved cross sections for this system along with CTMC and experimental total cross sections from Simcic et al. (2010b), which are slightly lower than the MCLZ total cross section at the same energy point.

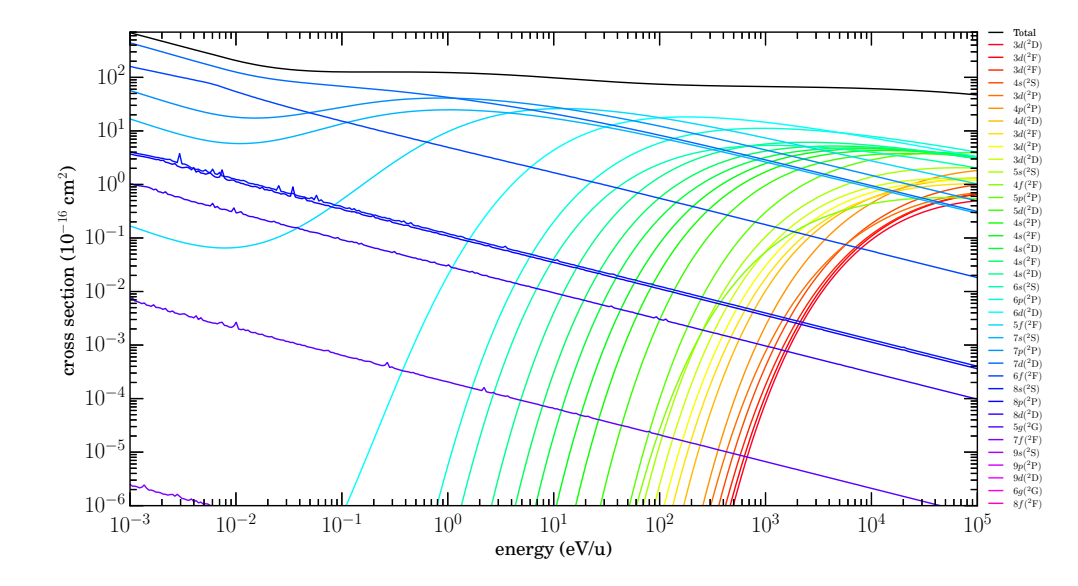


Figure 4.29: Fe⁸⁺+CO₂ \rightarrow Fe⁷⁺+CO₂⁺ $n\ell$ -resolved cross sections.

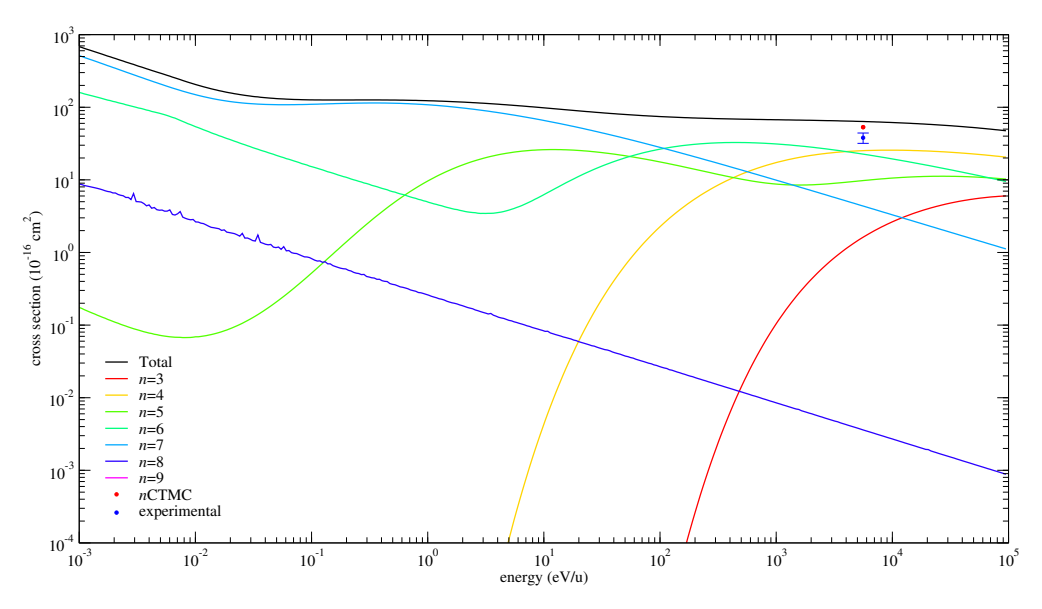


Figure 4.30: Fe⁸⁺+CO₂ \rightarrow Fe⁷⁺+CO₂+ n-resolved cross sections.

MCLZ comparision to CTMC and experimental results of Simcic et al. (2010b) .

$4.3.7 \quad FE^{8+} + N_2$

Figure 4.31 shows $n\ell$ -resolved cross sections for $\mathrm{Fe^{8+}} + \mathrm{N_2} \rightarrow \mathrm{Fe^{7+}} + \mathrm{N_2^+}$, and Figure 4.32 shows n-resolved cross sections for this system. There are no other known available data for comparison. The dominant channels are listed in Table 4.8.

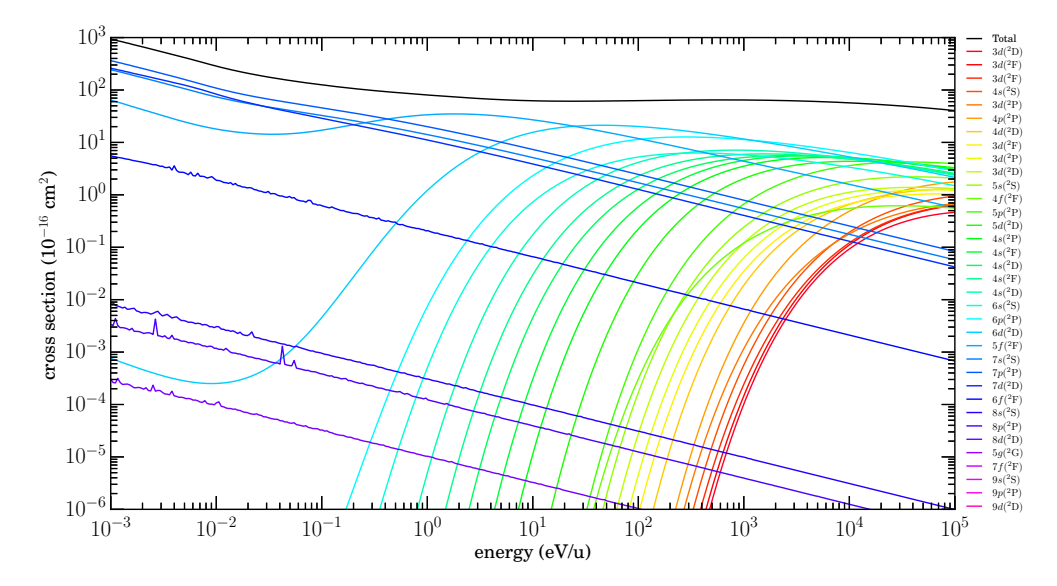


Figure 4.31: Fe⁸⁺+N₂ \rightarrow Fe⁷⁺+N₂⁺ $n\ell$ -resolved cross sections.

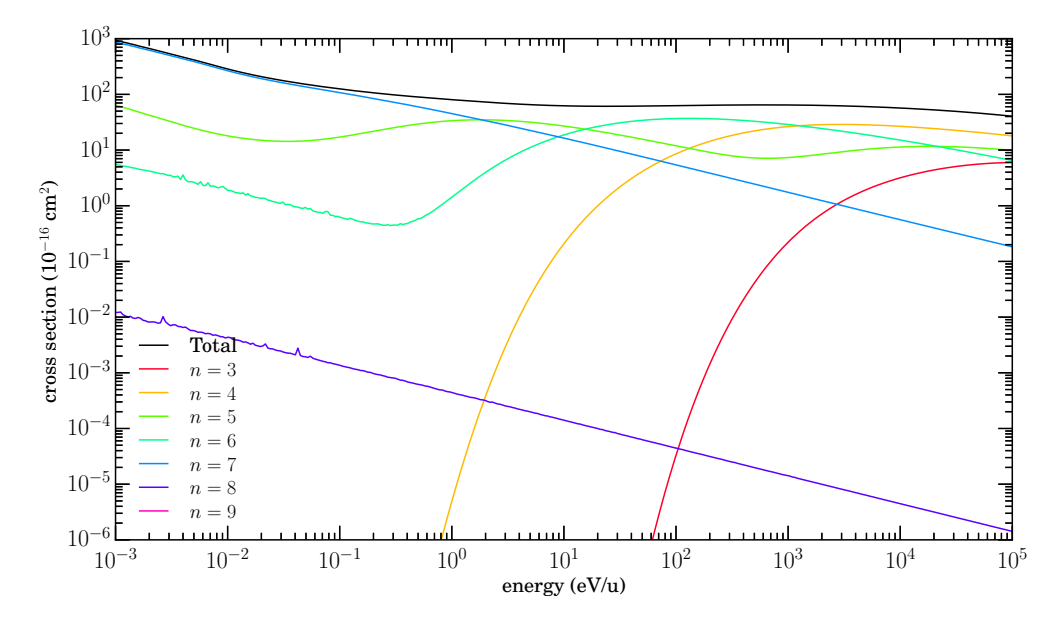


Figure 4.32: Fe⁸⁺+N₂ \rightarrow Fe⁷⁺+N₂⁺ n-resolved cross sections.

Table 4.8. $Fe^{(8-9)+}$ Dominant Channels.

System	Channel	$\mathrm{eV/u}$
$Fe^{9+}+H\to Fe^{8+}+H^{+}$	n=6	\lesssim 5.9e0
	$n{=}7$	5.9e0 - 1.5e3
	n=6	$\gtrsim 1.5e3$
$Fe^{9+} + H_2 \rightarrow Fe^{8+} + H_2^{+}$	$n{=}7$	\lesssim 5.0e-3
	$n{=}6$	5.0e-3-1.1e-1
	n=7	1.1e-1-4.7e2
	n=6	$\gtrsim 4.7 e2$
$\mathrm{Fe^{9+}} + \mathrm{He} \rightarrow \mathrm{Fe^{8+}} + \mathrm{H^{+}}$	n=6	$\lesssim 1.7e2$
	$n{=}5$	1.7e2 - 5.0e4
	$n{=}4$	$\gtrsim 5.0e4$
$Fe^{9+} + H_2O \rightarrow Fe^{8+} + H_2O^{+}$	n=8	\lesssim 5.6e0
	$n{=}6$	5.6e0 - 2.5e1
	$n{=}7$	2.5e1 - 1.1e4
	n=6	$\gtrsim 1.1e4$
$\mathrm{Fe^{9+}} + \mathrm{CO} \rightarrow \mathrm{Fe^{8+}} + \mathrm{CO^{+}}$	n=6	$\lesssim 2.1e0$
	$n{=}7$	2.1e0 - 1.4e3
	n=6	$\gtrsim 1.4e3$
$Fe^{9+}+CO_2 \rightarrow Fe^{8+}+CO_2^{+}$	n=8	\lesssim 9.0e-3
	n=6	9.0e-3-2.3e0
	$n{=}7$	2.3e0 - 1.2e3
	n=6	$\gtrsim 1.2e3$
$Fe^{8+}+H\to Fe^{7+}+H^{+}$	$n{=}7$	$\lesssim 4.5 e2$
	n=6	4.5e2 - 2.1e4
	$n{=}4$	$\gtrsim 2.1e4$
$Fe^{8+} + H_2 \rightarrow Fe^{7+} + H_2^{+}$	n=7	$\lesssim 3.7e0$
	n=6	3.7e0 – 3.6e1

4.4 Summary

Using the MCLZ method, SEC cross sections were calculated and plotted for $Fe^{q+}+X$, where q=8-9, and X=H, H_2 , H_2 , H_2 , H_3 , H_4 , H_4 , H_5 , H_6 , H_4 , H_5 , H_6 , H_7 , H_8 ,

Table 4.8 (cont'd)

System	Channel	eV/u
	n=5 $n=4$	3.6e1–3.1e3 \$3.1e3
$\mathrm{Fe^{8+}\!+\!He}{\rightarrow}\mathrm{Fe^{7+}\!+\!H^{+}}$	n=4 $n=4$ $n=5$	$\lesssim 1.0e2$ 1.0e2-7.4e4
${\rm Fe^{8+}\!+\!H_2O\!\to\!Fe^{7+}\!+\!H_2O^+}$	$n=3 \\ n=6 \\ n=7$	$\gtrsim 7.4e4$ $\lesssim 3.8e-1$ 3.8e-1-1.3e3
	n=6 $n=4$	$1.3e3-2.7e4$ $\gtrsim 2.7e4$

Chapter 5

${ m NE}^{9+}{ m +H}$ using ${ m MOCC}^1$

5.1 Introduction

Single electron capture charge exchange is investigated for the system $Ne^{9+}+H\rightarrow Ne^{8+}+H^+$ using the quantum-mechanical molecular orbital close coupling (MOCC) method as presented in Section 2.2. The MOCC method uses adiabatic potentials and nonadiabatic radial and rotational couplings to calculate cross sections. These potentials and couplings are obtained with the multi-reference single and double-configuration interaction (MRDCI) approach (Buenker and Peyerimhoff 1974, 1975; Buenker 1980, 1982a,b; Buenker and Phillips 1985; Buenker 1986; Krebs and Buenker 1995; Buenker and Krebs 1999). Using the MOCC method, cross sections are calculated at 1, 10, 100, and 1000 eV/u. The results are compared to the multichannel Landau-Zener cross sections of Lyons et al. (2017).

 $^{^{1}\}mathrm{D}$ A Lyons, P C Stancil, H P Liebermann, R J Buenker, 2019. To be submitted to The Astrophysical Journal.

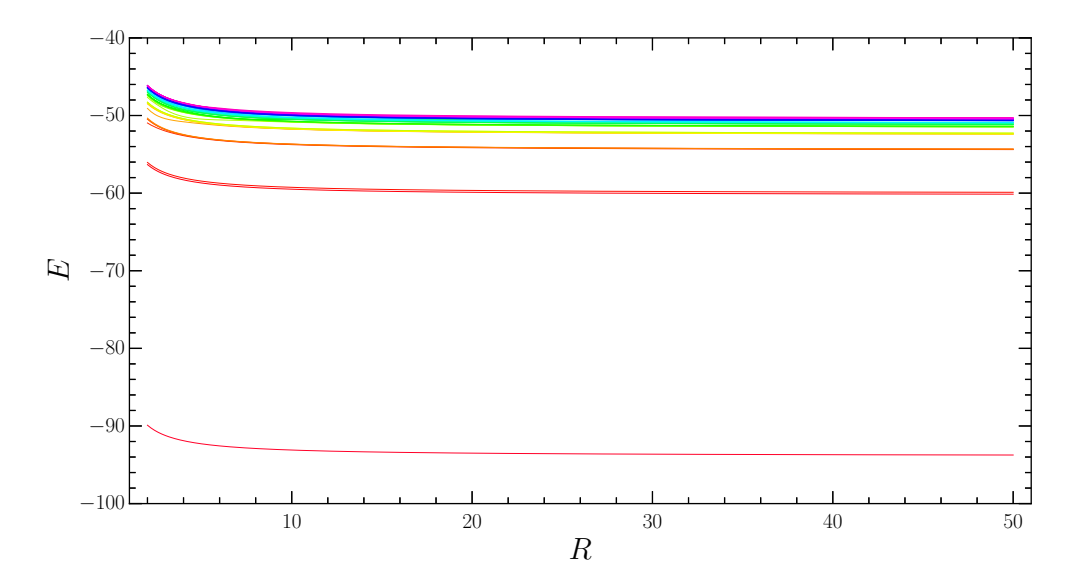


Figure 5.1: Adiabatic potentials singlets.

Figure 5.1 shows singlet potentials obtained with the MRDCI method. These lines correspond to the data in Table 5.1.

Table 5.1. MRDCI Potentials (singlets)

Index	Asymptotic state	Molecular state
1	$Ne^{8+}(1s1s) + H^{+}$	$1~^1\Sigma^+$
2	$Ne^{8+}(1s2s) + H^{+}$	$2~^1\Sigma^+$
3	$Ne^{8+(1s2p)} + H^{+}$	$3~^1\Sigma^+$
4	$Ne^{8+}(1s3s) + H^{+}$	$4~^1\Sigma^+$
5	$Ne^{8+}(1s3d) + H^{+}$	$1~^1\Delta^+$
6	$Ne^{8+}(1s3d) + H^{+}$	$2~^1\Delta^+$
7	$Ne^{8+}(1s3p) + H^{+}$	$5~^1\Sigma^+$
8	$Ne^{8+}(1s4s) + H^{+}$	$3~^1\Delta^+$
9	$Ne^{8+}(1s4d) + H^{+}$	$4~^1\Delta^+$
10	$Ne^{8+}(1s4d) + H^{+}$	$6^{1}\Sigma^{+}$
11	$Ne^{8+}(1s4p) + H^{+}$	$5~^1\Delta^+$
12	$Ne^{8+}(1s4f) + H^{+}$	$6^{1}\Delta^{+}$
13	$Ne^{8+}(1s4f) + H^{+}$	$7~^1\Delta^+$
14	$Ne^{9+}(1s) + H$	$8~^1\Delta^+$
15	$Ne^{8+}(1s5d) + H^{+}$	$9^{1}\Delta^{+}$
16	$Ne^{8+}(1s5p) + H^{+}$	$7^{1}\Sigma^{+}$
17	$Ne^{8+}(1s5s) + H^{+}$	$10^{-1}\Delta^{+}$
18	$Ne^{8+}(1s5f) + H^{+}$	$11~^1\Delta^+$
19	$Ne^{8+}(1s5f) + H^{+}$	$8~^1\Sigma^+$
20	$Ne^{8+}(1s5g) + H^{+}$	$12~^{1}\Delta^{+}$
21	$Ne^{8+}(1s5g) + H^{+}$	$13~^1\Delta^+$
22	$Ne^{8+}(1s5g) + H^{+}$	$14~^1\Delta^+$
23	$Ne^{8+}(1s6p) + H^{+}$	$15^{-1}\Delta^+$
24	$Ne^{8+}(1s5d) + H^{+}$	$16^{1}\Delta^{+}$
25	$Ne^{8+}(1s6d) + H^{+}$	$17~^1\Delta^+$
26	$Ne^{8+}(1s6s) + H^{+}$	$18 ^1\Delta^+$

Table 5.1 (cont'd)

Index	Asymptotic state	Molecular state
27	$Ne^{8+}(1s6f) + H^{+}$	$19^{-1}\Delta^{+}$
28	$Ne^{8+}(1s6f) + H^{+}$	$20^{1}\Delta^{+}$
29	$Ne^{8+}(1s7p) + H^{+}$	$21~^1\Delta^+$
30	$Ne^{8+}(1s6g) + H^{+}$	$22~^1\Delta^+$
31	$Ne^{8+}(1s6g) + H^{+}$	$23~^1\Delta^+$
32	$Ne^{8+}(1s6g) + H^{+}$	$24~^1\Delta^+$
33	$Ne^{8+}(1s7d) + H^{+}$	$25~^1\Delta^+$
34	$Ne^{8+}(1s7d) + H^{+}$	$9^{1}\Sigma^{+}$
35	$Ne^{8+}(1s7s) + H^{+}$	$10^{-1}\Sigma^{+}$
36	$Ne^{8+}(1s7f) + H^{+}$	$26^{-1}\Delta^+$
37	$Ne^{8+}(1s7f) + H^{+}$	$27^{-1}\Delta^+$
38	$Ne^{8+}(1s8s) + H^{+}$	$28~^1\Delta^+$
39	$Ne^{8+}(1s8p) + H^{+}$	$29^{1}\Delta^{+}$
40	$Ne^{8+}(1s8d) + H^{+}$	$30^{1}\Delta^{+}$
41	$Ne^{8+}(1s8d) + H^{+}$	$31~^1\Delta^+$
42	$Ne^{8+}(1s8f) + H^{+}$	$32~^1\Delta^+$
43	$Ne^{8+}(1s8f) + H^{+}$	$11 \ ^1\Sigma^+$
44	$Ne^{8+}(1s7g) + H^{+}$	$33~^1\Delta^+$
45	$Ne^{8+}(1s7g) + H^{+}$	$34~^1\Delta^+$
46	$Ne^{8+}(1s7g) + H^{+}$	$12~^{1}\Sigma^{+}$
47	$Ne^{8+}(1s9d) + H^{+}$	$13~^{1}\Sigma^{+}$
48	$Ne^{8+}(1s9d) + H^{+}$	$14^{-1}\Sigma^{+}$

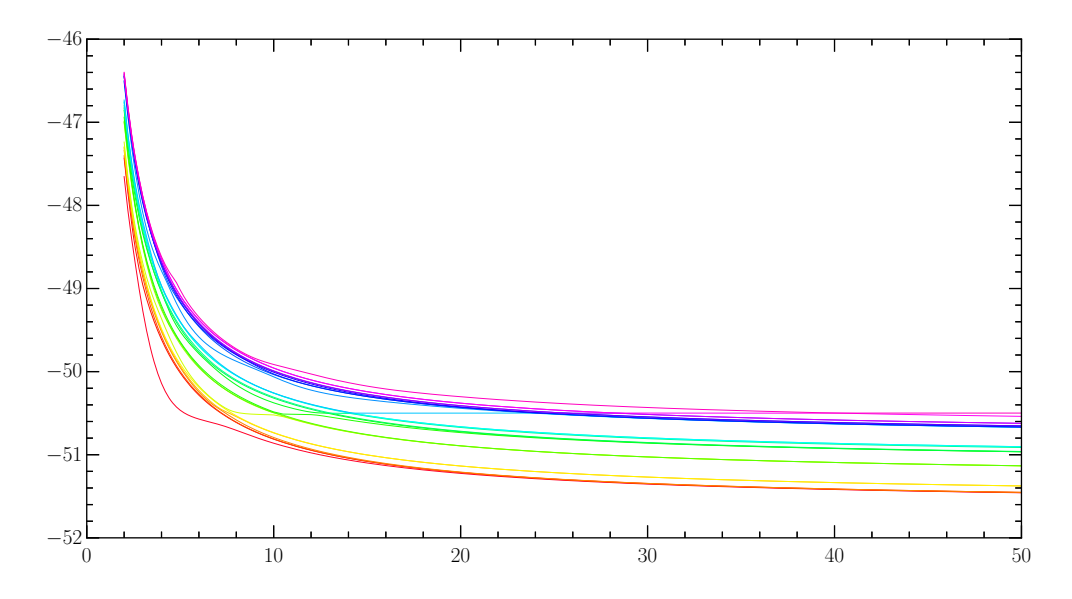


Figure 5.2: Avoided crossings for channels 14-38.

The avoided crosses of channels 14–38 are shown in Figure 5.2. Using the potential and coupling data generated by the MRDCI approach, singlet cross sections are calculated for energies 1, 10, 100, and 1000 eV/u.

5.2 Results

Using the MRDCI potentials and couplings, total and n-resolved cross sections for energies 1, 10, 100, and 1000 eV/u are shown in figure 5.3. Also shown are MCLZ cross sections (Lyons et al. 2017) for comparison.

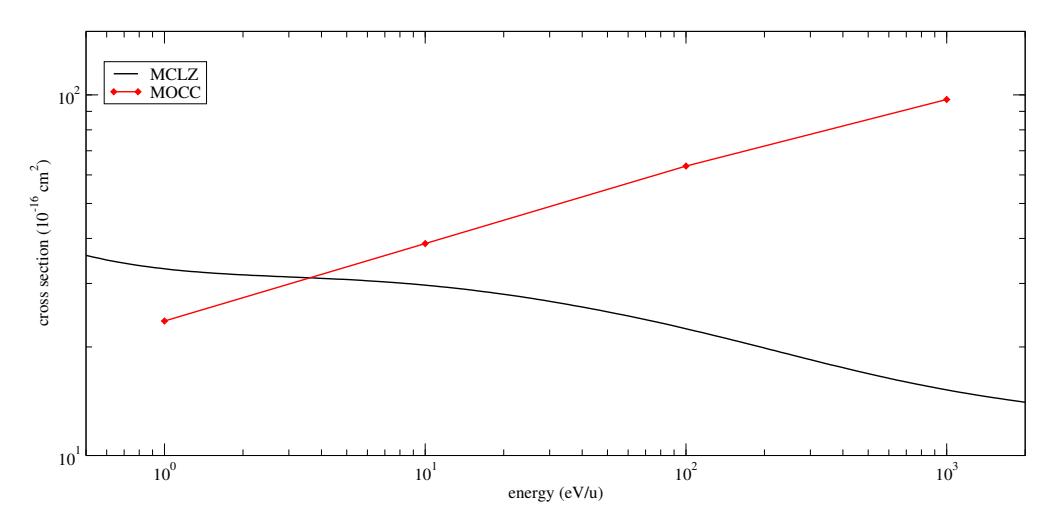


Figure 5.3: $Ne^{9+}+H\to Ne^{8+}+H^+$

MOCC and MCLZ singlet cross sections.

The MOCC total cross sections, for energies of 1 eV/u and 10 eV/u, are reasonably close to those of MCLZ at those energies. However, at 100 eV/u and 1000 eV/u, the MOCC cross sections exceed those of MCLZ by nearly an order of magnitude. The values calculated for the MOCC cross sections are shown in Table 5.2.

5.3 Summary

The MOCC method was used to calculate singlet cross sections for the charge exchange interaction $Ne^{9+}+H\rightarrow Ne^{8+}+H^{+}$. The MOCC total cross section results were fairly close

Table 5.2. MOCC Single Electron Capture Cross Sections

Energy (eV/u)	Cross section (10^{-16}cm^2)
$\begin{array}{c} 1.000\mathrm{e}{+00} \\ 1.000\mathrm{e}{+01} \\ 1.000\mathrm{e}{+02} \\ 1.000\mathrm{e}{+03} \end{array}$	$2.360\mathrm{e}{+01} \ 3.871\mathrm{e}{+01} \ 6.348\mathrm{e}{+01} \ 9.711\mathrm{e}{+01}$

to those of MCLZ (Lyons et al. 2017) at 1–10 eV/u. The total cross sections of the two methods diverged at 100 eV/u. Further data will be calculated with the MOCC method and compared to other available data.

Chapter 6

CONCLUSIONS

6.1 MCLZ: $NE^{(8-10)+}$ AND $MG^{(8-12)+}$

Using the multichannel Landau–Zener method, state-resolved CX cross sections were computed for highly charged Ne and Mg ions colliding with H and He. It was found that the MCLZ method can provide reasonable SEC cross sections for energies below 10 keV/u for the dominant capture channels. Comparison to previous work was primarily limited to Ne¹⁰⁺+H and a handful of results for Ne⁹⁺ and Ne⁸⁺. Some of the other less dominant channels do not agree as closely with other theoretical and experimental data as do the dominant channels, while prior results for the Mg ions considered here are completely lacking.

6.2 MCLZ: $FE^{(8-9)+}$

Cross sections were calculated for ionic systems $Fe^{(8-9)+}$ colliding with neutral atoms and molecules H, H₂, He, H₂O, CO, CO₂, and N₂, for single election capture. Excitation energies were estimated where they were not provided by NIST or other sources. These estimations were based on a version of the quantum defect method. The estimations of excitation energies should be accurate to two significant digits.

The results presented here were supported by CTMC and experimental results (Simcic et al. 2010a,b).

6.3 MOCC: NE⁹⁺+H

The molecular orbital close coupling (MOCC) method was used to calculate singlet cross sections at energies of 1, 10, 100, and 1000 eV/u for the SEC interaction of $Ne^{9+}+H\rightarrow Ne^{8+}+H^+$. MOCC is a computationally intensive procedure which, compared to a method such as MCLZ, produces a much smaller amount of data for the same amount of effort. The MOCC method can yield accurate results, but determining the best metrics to use for a given system might require a significant amount of trial and error.

Appendix A

Stückelberg

The cross sections computed here were generated with the MCLZ package Stückelberg written by the author using the C language and designed to be highly automated, efficient, and modular. It has also been used to generate cross section data for Mullen et al. (2016, 2017) and Cumbee et al. (2014, 2016, 2018). The user is required to only provide asymptotic atomic ion energies to Stückelberg, but a careful application of Wigner-Witmer rules to select final states consistent with allowed transitions is the user's responsibility. The code can be downloaded from https://www.physast.uga.edu/ambds/ along with documentation and a start-up guide.

Within the CXDatabase directory one will find the input files for $St\ddot{u}ckelberg$ and various output files including lists of avoided-crossings as well as n-, $n\ell$ -, and $n\ell S$ -resolved cross sections. For bare ions, $n\ell$ cross sections are given using the low-energy and statistical distribution functions, but other ℓ -distribution functions can be applied by the user to the n-resolved cross section files. Cross sections for additional collision pairs and/or obtained by other theoretical methods are expected to be routinely added. The cross sections will also be available on the UGA Charge Transfer Database (https://www.physast.uga.edu/ugacxdb/).

BIBLIOGRAPHY

- Abramov, V. A., Baryshnikov, F. F., and Lisitsa, V. S. (1978). Charge transfer between hydrogen atoms and the nuclei of multicharged ions with allowance for the degeneracy of the final states. Sov. Phys. JETP, 47:469–477.
- Ali, R., Neill, P. A., Beiersdorfer, P., Harris, C. L., Schultz, D. R., and Stancil, P. C. (2010). Critical test of simulations of charge-exchange-induced x-ray emission in the solar system. ApJ, 716:L95–L98.
- Bendahman, M., Bliman, S., Dousson, S., Hitz, D., Gayet, R., Hanssen, J., Harel, C., and Salin, A. (1985). Electron capture from atomic hydrogen by multiply charged ions in low energy collisions. J. De Physique, 46:561–572.
- Bransden, B. H. and McDowell, R. C. (1992). Charge Exchange and the Theory of Ion-Atom Collisions. Oxford.
- Buenker, R. J. (1980). Proceedings of the Workshop on Quantum Chemistry and Molecular Physics (Wollongong, Australia) ed P G Burton (Wollongong: University of Wollongong Press), page 151.
- Buenker, R. J. (1982a). Current Aspects of Quantum Chemistry, 1981 (Studies in Physical and Theoretical Chemistry vol 21) ed R Carbo (Amsterdam: Elsevier), page 17.
- Buenker, R. J. (1982b). Current Aspects of Quantum Chemistry, 1981 (Studies in Physical and Theoretical Chemistry vol 21) ed R Carbo (Amsterdam: Elsevier), page 81.
- Buenker, R. J. (1986). Int. J. Quantum Chem., 29:435.

- Buenker, R. J. and Krebs, S. (1999). Recent Advances in Multireference Methods (Recent Advances in Computational Chemistry vol 4) ed K Hirao (Singapore: World Scientific), page 1.
- Buenker, R. J. and Peyerimhoff, S. D. (1974). Individualized configuration selection in CI calculations with subsequent energy extrapolation. Theoret. Chim. Acta (Berl.), 35:33–58.
- Buenker, R. J. and Peyerimhoff, S. D. (1975). Energy extrapolation in CI calculations.

 Theoret. Chim. Acta, 39:217–228.
- Buenker, R. J. and Phillips, R. A. (1985). J. Mol. Struc.-Theochem, 123:291.
- Butler, S. E. and Dalgarno, A. (1980). Charge transfer of multiply charged ions with hydrogen and helium: Landau-Zener calculations. ApJ, 241:838–843.
- Child, M. S. (2010). *Molecular Collision Theory*. Dover Publications.
- Connerade, J. P. (1998). *Highly Excited Ions*. Cambridge University Press.
- Cox, D. P. (1998). Modeling the Local Bubble. In Breitschwerdt, D., Freyberg, M. J., and Trümper, J., editors, The Local Bubble and Beyond: Lyman-Spitzer-Colloquium (Lecture Notes in Physics), pages 121–131. Berlin:Springer, 1998 edition.
- Cravens, T. E. (2000). Heliospheric x-ray emission associated with charge transfer of the solar wind with interstellar neutrals. ApJ, 532(2):L153–L156.
- Cravens, T. E., Howell, E., Waite, Jr., J. H., and Gladstone, G. R. (1995). Auroral oxygen precipitation at Jupiter. Journal of Geophysical Research, 100:17153–17162.
- Cumbee, R. S., Henley, D. B., Stancil, P. C., Shelton, R. L., Nolte, J. L., Wu, Y., and Schultz, D. R. (2014). Can charge exchange explain anomalous soft x-ray emission in the Cygnus Loop? ApJ, 787(2):L31.

- Cumbee, R. S., Liu, L., Lyons, D., Schultz, D. R., Stancil, P. C., Wang, J. G., and Ali, R. (2016). Ne X X-ray Emission due to Charge Exchange in M82. Monthly Notices of the Royal Astronomical Society, 458(4):3554–3560.
- Cumbee, R. S., Mullen, P. D., Lyons, D., Shelton, R. L., Fogle, M., Schultz, D. R., and Stancil, P. C. (2018). *Theoretical charge exchange X-ray cross sections. ApJ*, 852(1):7C.
- Errea, L. F., Illescas, C., Méndez, L., Pons, B., Riera, A., and Suárez, J. (2004). Accuracy of the classical trajectory Monte Carlo method for electron capture in Li³⁺ and Ne¹⁰⁺+H(1s) collisions. Phys. Rev. A, 70:052713.
- Fabian, A. C., Sanders, J. S., Williams, R. J. R., Lazarian, A., Ferland, G. J., and Johnstone, R. M. (2011). The energy source of the filaments around the giant galaxy NGC 1275. Monthly Notices of the Royal Astronomical Society, 417:172–177.
- Greenwood, J. B., Williams, I. D., Smith, S. J., and Chutjian, A. (2001). Experimental investigation of the processes determining x-ray emission intensities from charge-exchange collisions. Phys. Rev. A, 63:062707.
- Grozdanov, T. P. (1980). Classical model for electron capture in collisions of highly charged, fully stripped ions with hydrogen atoms. Journal of Physics B: Atomic Molecular Physics, 13:3835–3847.
- Heil, T. G. and Dalgarno, A. (1979). Diabatic molecular states. Journal of Physics B:

 Atomic and Molecular Physics, 12(18):L557–L560.
- Janev, R. K., Belić, D. S., and Bransden, B. H. (1983). Total and partial cross sections for electron capture in collisions of hydrogen atoms with fully stripped ions. Phys. Rev. A, 28:3:1293-1302.

- Johnson, B. R. (1973). The multichannel log-derivative method for scattering calculations.

 Journal of Computational Physics, 13:445–449.
- Katsuda, S., Tsunemi, H., Mori, K., Uchida, H., Kosugi, H., Kimura, M., Nakajima, H., Takakura, S., Petre, R., Hewitt, J. W., and Yamaguchi, H. (2011). Possible chargeexchange x-ray emission in the Cygnus Loop detected with Suzaku. The Astrophysical Journal, 730(1):24.
- Kramida, A., Ralchenko, Y., Reader, J., and NIST ASD Team (2018). NIST Atomic Spectra Database (ver. 5.6.1), [Online]. Available: https://physics.nist.gov/asd [2015, April 16]. National Institute of Standards and Technology, Gaithersburg, MD.
- Krasnopolsky, V. A., Greenwood, J. B., and Stancil, P. C. (2004). X-Ray and extreme ultraviolet emissions from comets. Space Sci. Rev., 113:271–374.
- Krebs, S. and Buenker, R. J. (1995). J. Chem. Phys., 103:5613.
- Landau, L. D. (1932). A theory of energy transfer II. Phys. Zts. Sowjetunion, 2:46.
- Lisse, C. M., Dennerl, K., Englhauser, J., Harden, M., Marshall, F. E., Mumma, M. J., Petre, R., Pye, J. P., Ricketts, M. J., Schmitt, J., Trümper, J., and West, R. G. (1996). Discovery of x-ray and extreme ultraviolet emission from comet C/Hyakutake 1996 B2. Science, 274(5285):205–209.
- Lyons, D., Cumbee, R. S., and Stancil, P. C. (2017). Charge Exchange between Ne and Mg Ions and H and He. ApJS, 232(2):27–43.
- Maynard, G., Janev, R. K., and Katsonis, K. (1992). Electron capture and ionization in collisions of multicharged neon ions with atomic hydrogen. Journal of Physics B: Atomic, Molecular and Optical Physics, 25(2):437–444.

- Meyer, F. W., Howald, A. M., Havener, C. C., and Phaneuf, R. A. (1985). Low-energy total-electron-capture cross sections for fully stripped and H-like projectiles incident on H and H₂. Phys. Rev. A, 32:3310–3318.
- Mullen, P. D., Cumbee, R. S., Lyons, D., Gu, L., Kaastra, J., Shelton, R. L., and Stancil, P. C. (2017). Line ratios for solar wind charge exchange with comets. ApJ, 844(1):7.
- Mullen, P. D., Cumbee, R. S., Lyons, D., and Stancil, P. C. (2016). Charge exchange-induced x-ray emission of Fe xxv and Fe xxvi via a streamlined model. ApJS, 224(2):31.
- Nakamura, H. (2002). Nonadiabatic Transition. World Scientific Publishing Co Pte Ltd.
- Olson, R. E. and Salop, A. (1977). Charge-transfer and impact-ionization cross sections for fully and partially stripped positive ions colliding with atomic hydrogen. Phys. Rev. A, 16:531–541.
- Perez, J. A., Olson, R. E., and Beiersdorfer, P. (2001). Charge transfer and x-ray emission reactions involving highly charged ions and neutral hydrogen. Journal of Physics B: Atomic, Molecular and Optical Physics, 34(15):3063–3072.
- Schultz, D. R. and Kristić, P. S. (1996). Atomic and Plasma-Material Interaction Data for Fusion. Supplement to the Journal Nuclear Fusion, 16:173.
- Schwerdtfeger, P. and Nagle, J. K. (2018). 2018 Table of static dipole polarizabilities of the neutral elements in the periodic table. Molecular Physics, 0(0):1–26.
- Simcic, J., Schultz, D. R., Mawhorter, R. J., Greenwood, J. B., Winstead, C., McKoy, B. V., and Chutjian, S. J. S. A. (2010a). Measurement and Calculation of Absolute Single and Multiple Charge Exchange Cross Sections for Fe^{q+} Ions Impacting H₂O. ApJ, 722:425–439.
- Simcic, J., Schultz, D. R., Mawhorter, R. J., Cadež, I., Greenwood, J. B., Chutjian, A., Smith, S. J., and Lisse, C. M. (2010b). *Measurement of absolute single and multiple*

- charge exchange cross sections for Fe^{q+} ions impacting CO and CO₂. Phys. Rev. A, 81:062715.
- Smith, R. K., Foster, A. R., Edgar, R. J., and Brickhouse, N. S. (2014). Resolving the origin of the diffuse soft x-ray background. ApJ, 787(1):77.
- Stückelberg, E. C. G. (1932). Theory of Inelastic Collisions between Atoms. Helvetica Physica Acta, 5:369–423.
- Taulbjerg, K. (1986). Reaction windows for electron capture by highly charged ions. Journal of Physics B: Atomic and Molecular Physics, 19(10):L367–L372.
- Wigner, E. and Witmer, E. E. (1928). Über die Struktur der zweiatomigen Molekelspektren nach der Quantenmechanik. Zeitschrift fur Physik, 51:859.
- Zener, C. (1932). Non-adiabatic crossing of energy levels. Proceedings of the Royal Society of London. Series A, Containing Papers of a Mathematical and Physical Character, 137:696–702.